



FACHBEREICH C - MATHEMATIK
UND NATURWISSENSCHAFTEN
BERGISCHE UNIVERSITÄT
WUPPERTAL

HADES - an acoustic sensor for neutrino detection in ice

Calibration, characterization and
measurements

Benjamin Semburg

Dissertation

zur Erlangung des Doktorgrades
Fachgruppe Physik
Bergische Universität Wuppertal

Februar 2011

Astroteilchenphysik

HADES - an acoustic sensor
for neutrino detection in ice
Calibration, characterization and measurements

DISSERTATION

zur Erlangung des Doktorgrades
doctor rerum naturalium
(Dr. rer. nat.)



Fachbereich C – Mathematik und Naturwissenschaften

Der Fachgruppe Physik vorgelegt von

Benjamin Semburg

im

Februar 2011

Dedicated to Tom and Julia

It all started with the big BANG!

*Excerpt from the lyrics "History of Everything"
by Barenaked Ladies. Also theme music
from the sitcom "The Big Bang Theory".*

Contents

List of Figures	VII
List of Tables	IX
Nomenclature	XI
1 Introduction	1
2 Neutrinos from Cosmic Rays	5
2.1 Primary cosmic ray spectrum	6
2.2 GZK cutoff	8
2.3 Active Galactic Nuclei (AGN)	10
2.4 Gamma Ray Burst (GRB)	11
2.5 The Waxmann Bahcall-Limit	13
2.6 Z-Bursts	14
3 Neutrino detection mechanisms	15
3.1 Optical detection mechanism	15
3.1.1 IceCube observatory	17
3.2 Acoustical detection mechanism	21
3.3 Radio detection mechanism	24
4 South Pole Acoustic Test Setup	27
4.1 Permanently deployed in-ice hardware	27
4.2 Retrievable transmitter - the pinger	31
4.2.1 First pinger season in 2007/2008	33
4.2.2 Second pinger season in 2008/2009	34
4.2.3 Third pinger season in 2009/2010	35
4.3 Recent SPATS results	36
4.3.1 Sound speed in deep South Pole ice	36
4.3.2 Acoustical attenuation length	37

5	Design of acoustic sensors	41
5.1	SPATS sensors	41
5.2	HADES sensors	43
6	Absolute calibration methods	49
6.1	Comparison method	49
6.2	Reciprocity calibration method	50
6.3	Pre-calibrated hydrophone Sontech SQ03	63
7	Laboratory facilities	67
7.1	Wuppertal Water Tank Test Facility	67
7.2	Aachen Acoustic Laboratory (AAL)	72
8	HADES sensor properties	75
8.1	Directional sensitivity	75
8.1.1	Azimuthal sensitivity of HADES	80
8.1.2	Zenith sensitivity of HADES	82
8.2	Self-noise	89
8.3	Sensitivity change with temperature	93
8.4	Calibration in water	94
8.5	Calibration in ice	98
8.6	In-situ calibration	103
9	South Pole ice properties	119
9.1	South Pole noise	119
9.2	Transient event location reconstruction	126
10	Summary and Outlook	135
	Bibliography	137
	Appendix	i
A	Discrete Fourier transform	i
A.1	Basic equations	i
A.2	Continuous Fourier transform	i
A.3	Discrete Fourier transform	ii
A.4	Power spectral density (PSD)	iii
A.5	Relation between PSD and signal RMS	iv
	Acknowledgment	v

List of Figures

1.1	Messenger particles from extraterrestrial objects and possible detector types	1
2.1	Primary cosmic ray spectrum	6
2.2	Mean time between $\gamma_{\text{CMB}} - p$ interaction	9
2.3	Unified model of active galactic nuclei (AGN)	11
2.4	GRB fireball shock model	12
3.1	Schematic view of the optical detection principle	16
3.2	The IceCube observatory with its sub detectors	18
3.3	Depth dependent effective scattering coefficient and absorption coefficient for different wavelengths	19
3.4	The IceCube array footprint without DeepCore	20
3.5	Schematic drawing of hadronic cascade	22
3.6	Shape of bipolar pulses according to three different thermo acoustic models	22
3.7	The electric field strength caused by a 10 TeV electron versus observation angle	25
4.1	SPATS array layout	29
4.2	SPATS geometry inside the IceCube detector	30
4.3	Fourier spectrum of transmitter pulse	30
4.4	Pinger HVRB pulse in time and frequency domain	33
4.5	Pinger TVR	34
4.6	The pinger equipped with centralizers	35
4.7	Measured sound speed for both pressure waves and shear waves at depth of equipped SPATS stages	37
4.8	Absorption length for different frequencies and temperatures	38
5.1	Inside view of one SPATS sensor housing used at SPATS strings A-C	42

5.2	Inside view of one SPATS sensor housing used at SPATS string D	42
5.3	Schematic drawing with dimensions of the piezo ceramic element used for HADES sensors	43
5.4	Two stage amplifier board for HADES sensors	43
5.5	HADES sensor without PU coating and schematic drawing (bottom view) of a HADES sensor	44
5.6	HADES sensor: piezo ceramic element with two step amplifier.	44
5.7	Deployment of SPATS string D; stage 6 with HADES B	45
5.8	Deployment of SPATS string D; stage 2 with HADES A	45
5.9	Intra-stage event detected with HADES B at a depth of 430 m	46
5.10	Measured peak to peak amplitudes vs. time from intra-stage runs with HADES B	47
6.1	Schematic drawing of the setup for calibration via comparison method	49
6.2	Validation of the electroacoustic reciprocity principle for T_1 . .	51
6.3	Schematic setup for the impedance measurement	57
6.4	Impedance measurement for transducer T_2 at one certain temperature	58
6.5	Schematic setup with coil for contact free transducer driving current measurement	59
6.6	T_1 driving current comparison	60
6.7	Density vs. temperature of H_2O	60
6.8	Transducer T_2	61
6.9	Schematic setup for reciprocity calibration in water	62
6.10	Schematic setup for reciprocity calibration in ice	62
6.11	Sensortech SQ03	63
6.12	Measured sensitivity of SQ03 in 2004	64
6.13	Comparison between the sensitivity measurements from 2004 and 2010	65
6.14	Ratio between the sensitivities from SQ03 calibrations in Rome 2004 and 2010	65
7.1	Wuppertal Water Tank Test Facility	69
7.2	Top view of one sensor mounting with angular scale and HADES sensor mounted between stainless steel ropes	70
7.3	Peak to peak amplitude versus time measured with HADES B (2)	71
7.4	Peak to peak amplitude versus time measured with HADES B (2), prior covered by liquid soap	71

7.5	IceTop tank with the FCU at the front inside the cooling container	73
7.6	Schematic drawing of the IceTop tank	73
7.7	Speed of sound for pressure waves in clear ice produced in AAL	73
8.1	Relative azimuth sensitivity of piezo electric element coated without amplifier (type I)	76
8.2	Relative azimuth sensitivity of piezo electric element coated without amplifier (type II)	77
8.3	Relative azimuth sensitivity of piezo electric element coated without amplifier (type II; split up)	78
8.4	Relative zenith sensitivity of piezo electric element coated without amplifier (type I)	79
8.5	Relative zenith sensitivity of piezo electric element coated without amplifier (type II)	80
8.6	Relative azimuth sensitivity of HADES sensors	81
8.7	Schematic drawing of shadowing effect in zenith angle due to sensor housing	82
8.8	Relative zenith sensitivity of HADES sensors	83
8.9	Normalized zenith sensitivity with polynomial fit	84
8.10	In-situ measurement of relative zenith sensitivity with frozen in transmitters	87
8.11	Transmitter AT5 signal received by HADES A	87
8.12	Transmitter AT5 signal received by HADES B	88
8.13	Transmitter AT5 signal received by CS5(1)	88
8.14	Noise waveform recorded with HADES A (1) at -40°C air temperature in time and frequency domain	90
8.15	Mean RMS versus temperature for several sensors	92
8.16	Calculated pinger signal energy versus air temperature for time and frequency domain	93
8.17	Top view of the calibration setup inside the water tank	94
8.18	Calibration results for HADES B (1) and (2) in water	95
8.19	Schematic drawing of in ice calibration setup with systematic modification of the azimuthal orientation of SQ03	96
8.20	Sensitivity of SQ03 measured via the ice calibration setup in water in comparison with the sensitivity result from Rome 2010	97
8.21	The positioning system; three levels equipped with six sensor / transmitter pairs per level	98
8.22	Schematic drawing of the IceTop tank including the positioning system with the three levels of sensors / transmitters	98
8.23	Artist view of the installed equilateral double triangle	99

8.24	Top view of the IceTop tank with installed HADES calibration setup and Murata sensors	99
8.25	Calibration results at -21.6°C ice temperature and $145\ \mu\text{s}$ signal time window	101
8.26	Averaged sensitivities at different temperatures	101
8.27	Averaged sensitivity for every single calibration measurement result in ice for HADES B (1) and (2)	102
8.28	Location of IceCube holes used for pinger runs after the installation of string D in season 2007/2008 and pinger lowered into an IceCube hole	104
8.29	Pressure sensor data for pinger hole #69	104
8.30	Peak to peak amplitude (signal) vs. time for pinger run in hole #69	106
8.31	Stable pinger waveform in time (left) and frequency (right) domain	107
8.32	All nine sequences, not clock drift corrected, with tripolar pulse fit	108
8.33	Position of each signal maximum per sequence versus sequence number normalized to sequence nine	108
8.34	All nine sequences clock drift corrected	108
8.35	Averaged sequences with tripolar fit	109
8.36	Expected acoustic pinger pulse	109
8.37	Received pinger signal with HADES B and a corresponding noise measurement in comparison with the (scaled) theoretical pinger output	110
8.38	Pinger prepared for pool test	111
8.39	Schematic drawing of pool setup for pinger frequency content measurement	111
8.40	Comparison of theoretical pinger frequency power spectrum with pool measurements done with SQ03	112
8.41	Ratio of the theoretical pinger power spectral density with measurements done with SQ03	113
8.42	Sketch for the visualization of distance d and emergent angle α_2 between pinger and HADES B	114
8.43	Transmission coefficient t versus emergent angle α_2	114
8.44	HADES B in-situ absolute sensitivity estimation	115
8.45	Sketch for the visualization of distance d between pinger and selected SPATS sensors	116
9.1	Distribution of ADC values from one day of noise data	120

9.2	Noise RMS values versus time for HADES A & B (left side) and histogram with Gauss fit.	121
9.3	FFT of RMS noise data versus time recorded with HADES sensors in 2009	124
9.4	Power consumption in time and frequency domain for the ICL and PMDE for 2009	125
9.5	Arbitrarily chosen transient events recorded with HADES A .	127
9.6	Reconstructed transient events from July 1 st to October 22 nd 2008 with $\chi^2 / \text{NDF} < 25$	130
9.7	Reconstructed transient events from July 1 st to October 22 nd 2008 with $\chi^2 / \text{NDF} < 8$	131
9.8	Schematic drawing of Rodriguez well	132
9.9	PSD of triggered event	133

List of Tables

3.1	Parameters for comparison between different media for acoustic neutrino detection	23
6.1	Near and far field requirements with capable reciprocity parameter and pressure field	56
8.1	Combination of HADES sensors and transmitter pairs with visible transmitter signals	85
8.2	Distance matrix for the in ice calibration setup in AAL	100
8.3	Final pinger stop depth for hole #69 calculated via the mean of the depth received via turn counting and pressure sensor data	105
8.4	Averaged sensitivity (5-30 kHz) of selected SPATS sensors based on horizontal pinger measurements in austral summer season 2008/2009	117
8.5	Systematic uncertainties for HADES sensor corresponding to the in-situ calibration with the pinger as calibrated transmitter	118
9.1	Used sensor channels for transient data taking	126

Nomenclature

AAL	Aachen Acoustic Laboratory
ADC	Analog to digital converter
AGN	Active galactic nucleus/nuclei
APB	Acoustic Pinger Box
DAQ	Data acquisition system
DFT	Discrete Fourier Transform
FCU	Freeze Control Unit
Firn	Layer of uncompactified surface snow above the ice in Antarctica
GPS	Global Positioning System
GRB	Gamma ray burst
HADES	Hydrophone for Acoustic Detection at South Pole
HVRB	High voltage read back
Intra-stage run	If a transmitter of a certain stage is fired and the sensor of the same stage received the signal.
IRIG-B	Inter Range Instrumentation Group Timecode; provides 100 pps
PMT	Photomultiplier tube
PPS	Pulse Per Second
PSD	Power spectral density
PU	Polyurethane
P-wave	Longitudinal or pressure wave

XII

Rod well	<u>R</u> odriguez well; Man-made hot water cavern in the ice, used for hole drill
SPATS	South Pole Acoustic Test Setup
S-wave	Transversal or shear wave
TOS	Tower Operations Structure
TVR	Transmit Voltage Response

Chapter 1

Introduction

Multiple types of particles permanently reach our planet and are used for observation and research of objects surrounding us in the universe (see Figure 1.1). The particles interacting with the atmosphere, reaching the Earth's surface (photons only) or traversing it.

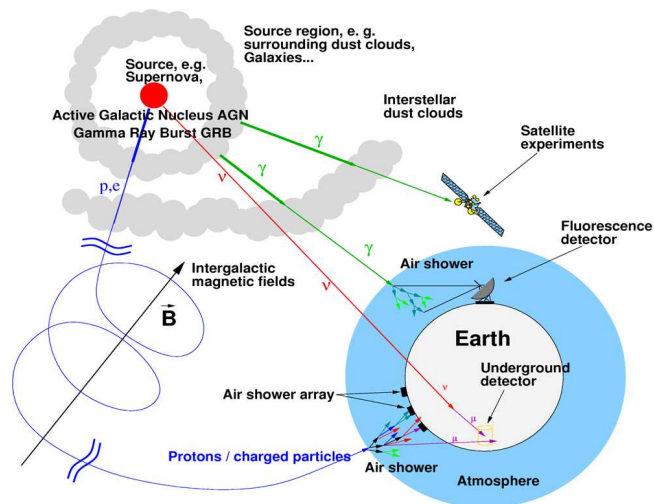


Figure 1.1: Messenger particles from extraterrestrial objects and possible detector types [Wag 04].

Observations of the sky using visible light (photon or γ with a frequency from 800-400 THz) reach back in time to the beginning of mankind. Research started with the naked eye until the present telescopes located in space or at elevated locations on Earth looking light years deep inside the universe. Today, detectors for the whole photon energy spectrum are avail-

able and sky observations starting in the TeV and GeV range down to X-ray and radio light are possible. Photons point straight back to their source, but they cannot pass dust or dense gas clouds, which reduces their observability.

Also taking into account the charged particles reaching the Earth, source information about the corresponding acceleration process can be derived via the energy spectrum of these particles. Only the extreme high energetic particles can communicate far-reaching information about their source location. These particles are rare and require huge detectors to reach a sufficient number of detections within a scientist's life. All other charged particles are deflected by magnetic fields and the information of source direction is lost.

All particles mentioned above are part of the so called *cosmic rays*. Viktor F. Hess discovered 1912 this type of radiation (honored with the Nobel prize in 1936 together with Carl D. Anderson for his discovery of the positron) via balloon flights up to an altitude of 5 km. His discovery was the starting point to develop detectors to analyze cosmic rays after which many new particles have been observed. Today, the particles of cosmic rays reaching the Earth are called *primary cosmic rays*, and all particles produced in an interaction between primary cosmic rays and molecules of the atmosphere or the Earth itself are called *secondary cosmic rays*.

To fulfill the requirement of energy and momentum conservation during the nuclear beta decay

$$n \rightarrow p + e^- + \bar{\nu}_e \quad (1.1)$$

Wolfgang Pauli postulated in 1930 a new elementary particle. Enrico Fermi published in 1934 the theoretical properties and interactions of this particle and named it *Neutrino* ν (for small neutron) [Fer 34].

Clyde L. Cowan and Frederick Reines managed to detect the first Neutrino (electron antineutrino) via inverse beta decay

$$\bar{\nu}_e + p \rightarrow n + e^+ \quad (1.2)$$

with the “Poltergeist” project at the Savannah River nuclear reactor in 1956 [Rei 56]. Reines was rewarded with the Nobel prize together with Martin L. Perl (for the discovery of the tau lepton) in 1995¹.

¹Clyde Cowan died in 1974

In 1962 Jack Steinberger, Melvin Schwartz and Leon M. Lederman discovered the muon neutrino with help of the first neutrino beam produced at an accelerator. They were honored with the Nobel prize in 1988.

The tau neutrino was expected after the discovery of the tau in 1975. The direct observation of the tau neutrino succeeded the DONUT² collaboration in 2000.

Neutrinos are the only messengers penetrating every object between the source and the observer without deflection. But the very small cross section for neutrino interactions puts very high demands on the detectors. As neutrinos only interact weakly, they cannot be accelerated in electromagnetic fields. Therefore, neutrinos with high energies have to be products of decays or interactions of high energy cosmic ray particles which were previously accelerated.

Neutrino astronomy uses the nearly massless, not charged and only weakly interacting neutrino particles to observe the sky in *neutrino light*. This started not a century ago and leads to one of the biggest detectors ever built so far.

Possible extraterrestrial sources for neutrinos will be described in Chapter 2.

A neutrino interaction with a nucleus of a dense medium causes a hadronic shower and in charged current interactions one lepton leaving the interaction point in extension of the neutrino direction. In ice (and water) the shower and the outgoing lepton produce Cherenkov light. In the Antarctic ice sheet at the geographic South Pole optical modules are deployed to detect this light, building the IceCube detector. Beside the location of the shower, the lepton track and therefore the direction of the neutrino can be reconstructed with the arrival time information of the Cherenkov light at multiple optical modules. With the intensity of the Cherenkov light at each optical module the energy can be estimated. In addition to the lepton, the hadronic shower causes a local heating of the surrounding medium which generates a pressure wave (based on work of G. A. Askarian) and radio signals are emitted from electromagnetic cascades caused by hadronic shower. Ice offers the unique possibility to detect a neutrino interaction with three different independent techniques e. g. optical, acoustical and radio, and studies for a possible hybrid detector are under way (details will be presented in Chapter 3).

²Direct Observation of the NU Tau at Fermilab

The optical attenuation length of Cherenkov light emitted by the outgoing lepton in the South Pole ice is in the order of 100 m. This requires a dense spacing between optical modules. In [Pri 06] the attenuation length of acoustic signals in the same media should be a few kilometers. If this were true, with the same number of acoustical modules in comparison with the optical modules, a bigger volume could be equipped which would lead to a higher neutrino detection rate. But in addition to the acoustic attenuation length, which determines the energy threshold, other acoustic ice properties (e. g. the acoustic noise level) need to be studied at first.

To verify the acoustical attenuation length, predicted from theory with a few kilometers length, and to investigate the South Pole ice properties (e. g. sound speed, rate of transient acoustic signals and the acoustical noise level) the South Pole Acoustic Test Setup (SPATS) was developed and installed in the upper part of IceCube holes. The permanently deployed hardware, called *SPATS array*, the retrievable transmitter - *the pinger* - and recent results will be described in Chapter 4.

The SPATS array contains first and second generation SPATS sensors and two HADES (Hydrophone for Acoustic Detection at the South Pole) sensors, developed in this thesis. All three types of acoustic sensors are presented in detail in Chapter 5.

In Chapter 6 the theories concerning absolute calibration of hydrophones will be explained. Laboratory facilities for absolute calibration measurements of HADES sensors in water and ice will be introduced in Chapter 7. An absolutely calibrated hydrophone is essential for an absolute noise measurement.

Properties of the HADES sensor like angular sensitivity, absolute sensitivity and the absolute self-noise, received via laboratory and in-situ measurements will be presented and discussed in Chapter 8.

The absolute South Pole noise level and results of an acoustical transient event location reconstruction will be shown in Chapter 9.

Chapter 2

Neutrinos from Cosmic Rays

Today, the results of experiments exclude the existence of 2 or rather 4 different kinds - named *flavors* - of neutrinos. The three neutrino flavors are: electron neutrino ν_e , muon neutrino ν_μ and tau neutrino ν_τ .

In the *standard model of particle physics* (SM) the neutrinos are uncharged *fermions* (spin 1/2 particles) with membership in the *lepton family*. To each neutrino flavor there is one charged lepton; electron neutrino $\nu_e \leftrightarrow$ electron e^- , muon neutrino $\nu_\mu \leftrightarrow$ muon μ^- and tau neutrino $\nu_\tau \leftrightarrow \tau^-$. Due to the proven existence of antiparticles to the charged leptons e^+ , μ^+ and τ^+ , the corresponding antineutrinos $\bar{\nu}_e$, $\bar{\nu}_\mu$ and $\bar{\nu}_\tau$, are also required. The charge cannot be used to distinguish between neutrino and antineutrino, because they are not charged, and therefore it cannot be excluded that the neutrino is its own antiparticle. If this were the case, it would be called *Majorana particle*.

Until now, only upper limits for the neutrino masses are known [Nak 10]:

$$m_{\nu_e} < 2 \frac{\text{eV}}{c^2} \quad m_{\nu_\mu} < 0.19 \frac{\text{MeV}}{c^2} \quad m_{\nu_\tau} < 18.2 \frac{\text{MeV}}{c^2}$$

Due to the fact that neutrinos only interact weakly, they cannot be accelerated in electromagnetic fields. Therefore, high energetic neutrinos need to be products of decays and/or interactions of previously accelerated high energetic (charged) cosmic ray particles. In this thesis particles with energies above 10^9 eV are *high energy cosmic ray* (HECR) particles and particles exceeding energy of 10^{18} eV are called *ultra high energy cosmic ray* (UHECR) particles. The energy spectrum of these particles will be discussed hereafter.

2.1 Primary cosmic ray spectrum

The energy spectrum was measured by many different experiments and the combination of all results leads to an energy spectrum from 10^9 eV up to more than 10^{20} eV. The spectrum (flux vs. energy) is pictured in Figure 2.1. Below 10^9 eV the cosmic ray particles are deflected by the solar wind and the measured spectrum is no longer identical with the interstellar spectrum. As visible in Figure 2.1, the flux decreases rapidly with increasing energy (photon and neutrino fluxes have not been taken into account). Therefore, the (average) particle composition is dominated by low energy particles. The primary charged particle cosmic ray spectrum consists of protons (87%), α -particles (12%) and electrons (1%).

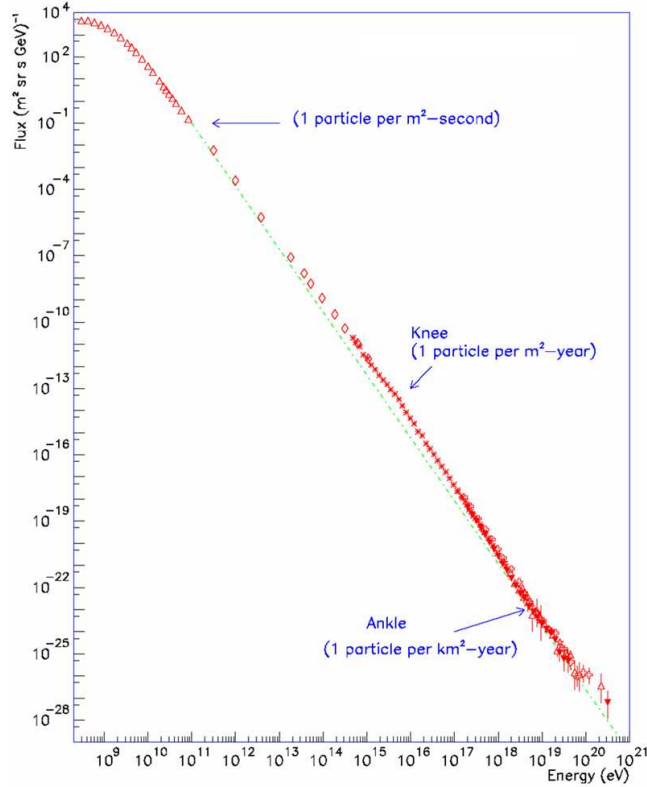


Figure 2.1: Primary cosmic ray spectrum of charged particles [Swo 97].

The differential cosmic ray *flux spectrum* follows a power law

$$\frac{dN}{dE} \sim E^{-\gamma} \quad (2.1)$$

with the *spectral index* γ . As visible in Figure 2.1, the spectrum can be divided into three parts, described via three different spectral indices and related to different sources of cosmic ray particles. Following the human leg the transition points from one spectral index to another are called *knee* and *ankle*.

From $5 \cdot 10^9$ eV to the region around the knee at $4 \cdot 10^{15}$ eV the spectral index is equal $\gamma = 2.7$. With the assumption that galactic sources are not able to accelerate particles to higher energies than located at the knee and that the magnetic fields of our galaxy cannot bind particles with higher energies the change in the spectral index to $\gamma \approx 3$ until the ankle region (at roughly $6 \cdot 10^{18}$ eV) can be explained. Around this energy the spectral index is falling again and two possible explanations for this will be discussed:

- The ankle could be interpreted as a source change; from galactic sources to extragalactic. This is assumed with a change in the composition of the cosmic ray particles; from heavier to lighter particles. The light extragalactic protons overtake the heavy galactic part.
- In [Ber 06] the dip is produced by pair production on the cosmic microwave background photons ($p + \gamma \rightarrow p + e^+ + e^-$) and is located in energy interval $1 \cdot 10^{18}$ eV to $4 \cdot 10^{19}$ eV. This is assumed to be at energies slightly lower than the GZK threshold (see Section 2.2) and causes the desired reduction of the spectral index. A strong indication for the GZK interaction was published by the *HiRes*- [Abb 08] and the *Pierre Auger Collaboration* [Abr 08]. They observed a steepening of the spectra above $4 \cdot 10^{19}$ eV

As mentioned above, high energetic neutrinos need to be products of decays and/or interactions of previously accelerated high energetic (charged) cosmic ray particles. Two possible acceleration models are the *first and second order Fermi acceleration*¹, found by Enrico Fermi [Fer 49]:

- the scattering of particles on randomly moving magnetic clouds is called *second order Fermi acceleration* and
- the scattering on (aligned) shock fronts moving at relativistic speed through the interstellar medium is known as *first order Fermi acceleration*.

¹ *Order* is related to the energy increase proportional to $\beta = v/c$, therefore first order Fermi acceleration is more efficient (because $\beta < 1$)

A possible shock front source could be a *super nova*. Calculations in [Gai 90] show that the maximum particle energy reached by Fermi acceleration in this shock front never exceeds a few 100 TeV. Other acceleration sources could be *active galactic nuclei* (AGN) or *gamma ray burst* (GRB)

In the following part a selection of possible production mechanisms for neutrinos will be presented.

2.2 GZK cutoff

The steepening of the charged cosmic ray spectrum at highest energies, found by the Pierre Auger Collaboration [Abr 08], is a big hint towards the existence of the so called *GZK cutoff*. Kenneth Greisen, Georgiy Zatsepin and Vadim Kuzmin developed in 1965 the theoretical prediction that the cosmic ray flux dies out in the energy range from 10^{19} eV to 10^{20} eV due to the interaction of ultra high energetic protons with photons of the *cosmic microwave background* (CMB). The highest energetic cosmic ray protons can produce the Δ^+ resonance with a CMB photon and the Δ^+ resonance decays as follows:

$$p + \gamma_{\text{CMB}} \rightarrow \Delta^+(1232) \rightarrow \pi^+ + n \quad (2.2)$$

$$p + \gamma_{\text{CMB}} \rightarrow \Delta^+(1232) \rightarrow \pi^0 + p$$

The produced pions decay in muon and neutrino or photon

$$\pi^0 \rightarrow \gamma + \gamma \quad (2.3)$$

$$\pi^+ \rightarrow \mu^+ + \nu_\mu$$

which decay in electrons and neutrinos

$$\mu^+ \rightarrow e^+ + \nu_e + \bar{\nu}_\mu. \quad (2.4)$$

Until now the CMB radiation was measured very precisely by the *Far In-fraRed Absolute Spectrometer* (FIRAS) located on the COBE satellite (*COs-mic Background Explorer*). With this data the absolute photon density \bar{n}_γ can be calculated to [Ben 03]:

$$\bar{n}_\gamma = 410 \text{ cm}^{-3} \quad (2.5)$$

With a proton cross section of $\sigma_p \approx 200 \mu\text{b}^2$ (increases to a maximum of about $400 \mu\text{b}$ [Gre 66]) the mean free path can be calculated via:

$$\lambda = \frac{1}{\sigma_p \bar{n}_\gamma} \approx 1.2 \cdot 10^{25} \text{ cm} \quad (2.6)$$

Within the meantime between $\gamma_{CMB} - p$ reaction, displayed in Figure 2.2, and an initial proton energy loss between 13% to 22% [Gre 66] it is obvious that the high energetic proton particle horizon is limited.

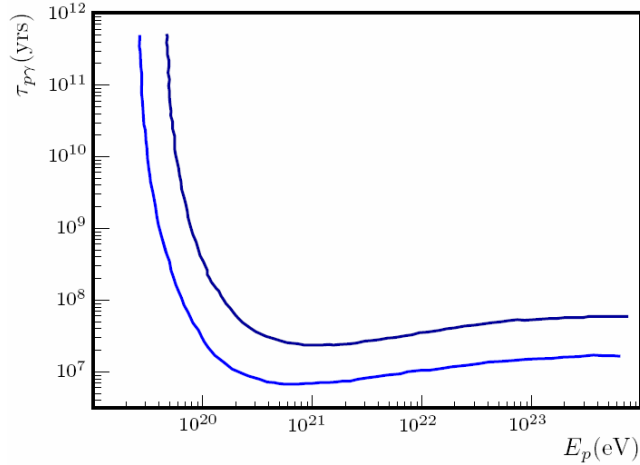


Figure 2.2: Mean time between $\gamma_{CMB} - p$ interaction. 10^7 yrs correspond to about 3 Mpc. Upper blue line: $T_{CMB} = 2$ K; lower light blue line: $T_{CMB} = 3$ K [Zat 66]

The reachable travel distance of protons (*GZK sphere for protons*) depends on the initial energy and the required remaining proton energy fraction.

On the other hand, if the GZK cutoff exists, the proton/photon interaction and the decays of sub-particles (as described above) should produce detectable neutrinos, called *cosmogenic neutrinos*, at highest energies. Calculations and the expected neutrino flux due to the GZK cutoff can be found in [Eng 01].

²¹ 1 b = 1 barn = 10^{-24} cm^2

2.3 Active Galactic Nuclei (AGN)

Based on the current knowledge it is assumed that inside the center of most galaxies a *super massive black hole*, with a mass of 10^6 to 10^{10} times the mass of our sun, is located. Each *active nucleus* owns an accretion disc and collects the surrounded matter. If radio emission of an AGN can be detected or not, they are classified in *radio loud* or *radio quiet* AGN, respectively.

in comparison with radio quiet AGN, which shows only a very weak or no jet, radio loud AGN produces a highly relativistic jet (of particles), emitted from the center, to compensate the angular momentum due to the accretion process. These jet particles are bound to the jet region by magnetic fields (with a few Gauss strength) caused by the plasma in the jet. The dimension of the jet region can cover the size of our Milky Way and beyond. These described jets are believed to produce cosmic rays of highest energies via first order Fermi acceleration, shock fronts moving through the jet.

The viewing angle on the accretion disc (perpendicular or parallel to the disc and in between) defines many different types of AGN; see Figure 2.3. The AGN type called *blazars* are radio loud AGN and the jets are pointing in the direction of the observer. As mentioned above these jets are believed to be the source of highest energy cosmic ray and a blazar emits these particles directly to the Earth (to the observer). A correlation between the positions of AGN and the source direction of cosmic rays was found by the Pierre Auger Observatory [Abr 07].

Two models of AGN are currently under discussion:

- The *pure leptonic model* describes the acceleration of electrons only. Therefore all AGN obeying this model would be visible in the γ -light but would not emit high energetic neutrinos.
- The *mixed leptonic/hadronic model* quotes, beside the acceleration of electrons, the acceleration of hadrons (mainly protons). The accelerated protons could interact with photons in the neighborhood of the jet and therefore the region around the AGN could be a source for high energetic neutrinos.

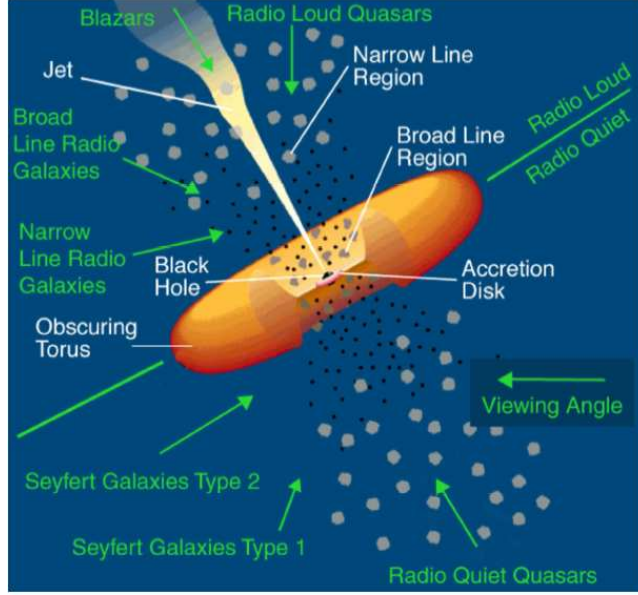


Figure 2.3: Unified model of active galactic nuclei (AGN) [Aug 10].

2.4 Gamma Ray Burst (GRB)

Today, it is assumed that the sources of Gamma Ray Bursts (GRBs) are cosmic objects which collapse. Possible candidates are: massive stars with high rotation frequency [Woo 93] [McF 99], millisecond proto-magnetars [Tho 04] or mergers of neutron star binaries or mergers of black hole - neutron star systems [Jan 99]. GRBs have high redshifts, they are isotropically distributed over the sky and it is assumed that these are the objects with the highest luminosity in our universe. These GRBs emit total energies in the γ -ray spectrum of about 10^{44} J ($= 10^{62}$ eV) and this happened in a very short time scale starting with seconds and could reach minutes. Within this time and the known propagation speed the radius of a sphere, which covers the bursts, can be calculated to be $10^2 - 10^3$ km, only.

In [Pir 99] a *fireball model* is described (using the dimension calculated above) which emits e^+e^- -pairs caused by the high γ -ray density in the bursts via pair production:

$$\gamma + \gamma \longrightarrow e^+ + e^- + \gamma \quad (2.7)$$

Furthermore the emission of a thermal photon spectrum from the fireball is predicted. In this model the photons are trapped inside the fireball and

their radiation energy will be converted into the kinetic energy of the baryons.

To explain the measured non-thermal photon spectra (see [Cav 81]) the *fireball shock model* described in [Ree 92] and [Més 93] will be introduced. In this model the fireball moves through the interstellar medium and the emitted shock waves, which are deflected on randomly distributed magnetic clouds, travel back through the ball. As described above the particle acceleration using shock fronts is known under first order Fermi acceleration and should be able to produce energies of up to 10^{20} eV. It is assumed that the produced high energetic electrons can produce synchrotron radiation in the γ -ray band via interactions with the surrounded magnetic fields. A visualization of the fireball shock model with the collapsed object and jets reacting with the interstellar medium is shown in Figure 2.4.

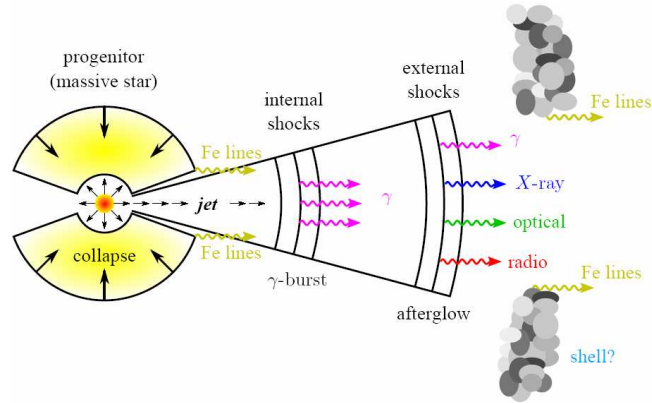
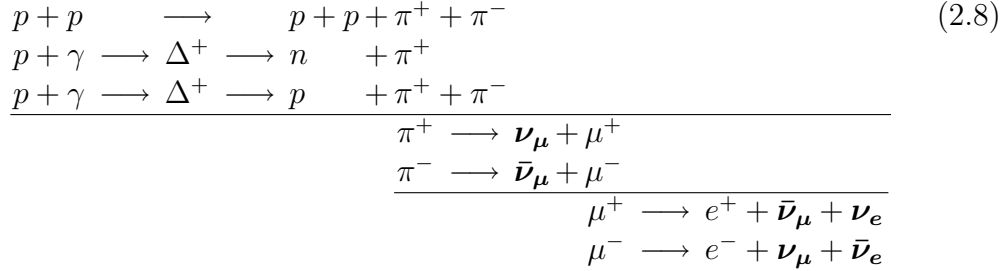


Figure 2.4: GRB fireball shock model. The γ -ray emission happens via synchrotron radiation on shocks, which are mediated by magnetic fields [Més 01].

2.5 The Waxmann Bahcall-Limit

Eli Waxmann and John Bahcall published in 1999 a calculated upper limit for *diffuse neutrino flux* [Wax 99]. This limit was validated in 2001 [Bah 01]. In this limit neutrino production via proton - proton and proton - photon interactions are assumed:



Interactions e.g. with neutrons as primary particles yielding to non-neutrino particles during decay are not displayed. As visible from above, the ratio of produced neutrino flavors are $\nu_e : \nu_\mu : \nu_\tau = 1 : 2 : 0$. in comparison with Equation 2.2 in Section 2.2 (GZK cutoff) these photons are part of the source itself and no relict photons.

It is assumed that the sources are expanded at least in the order of the mean free path of protons and participate in the reactions described above. This source property is known as *optical thin for protons*. If these protons are accelerated by Fermi acceleration and contribute to the high energetic cosmic ray spectrum, a spectral index of $\gamma=2$, which is the lower limit of the spectral index, is postulated.

With the energy production rate $\dot{\epsilon} \approx 5 \cdot 10^{44}$ erg Mpc⁻³ yr⁻¹ in the energy range from 10¹⁹ eV to 10²¹ eV, it is possible to calculate an overall limit of

$$E_\nu^2 \Phi_\nu < 2 \cdot 10^{-8} \frac{\text{GeV}}{\text{cm}^2 \text{ s sr}} \tag{2.9}$$

for the sum over these sources.

2.6 Z-Bursts

Another production process for neutrinos is the decay of a Z -boson developed via the following reaction [Wei 82]:

$$\bar{\nu} + \nu \longrightarrow Z \tag{2.10}$$

The primary neutrino is a relict particle of the hot big bang model with the current density of $n_\nu = 336 \text{ cm}^{-3}$ (summed over all flavors) [Zub 04]. This cosmic neutrino background should react with ultra high energetic antineutrinos from current sources and produce a Z -boson. This decays into hadronic jets, within a probability of 69.9%, which produce Z -bosons on their own until the energy decreases to the Z mass of 91 GeV. Based on this assumption an excess slightly below the Z mass in the cosmic ray neutrino spectrum is expected.

Chapter 3

Neutrino detection mechanisms

3.1 Optical detection mechanism

The optical neutrino detection mechanism is based on an indirect detection. Optical detectors do not measure the neutrino, but the secondary particles caused by a neutrino interaction with matter (symbolized via N for nucleus in the following). The neutrino can participate in a *neutral current* (NC) interaction

$$\nu_l + N \rightarrow \nu_l + X \quad (3.1)$$

or in a *charged current* (CC) interaction

$$\nu_l + N \rightarrow l + X \quad (3.2)$$

with the incoming neutrino flavor ν_l (ν_e , ν_μ or ν_τ), the hadronic cascade X and the corresponding outgoing lepton l (e , μ , τ). This outgoing lepton and the cascade particles traverse the reaction matter with a speed v which is higher than the speed of light c_{medium} inside this medium:

$$v > c_{\text{medium}} = \frac{c_{\text{vacuum}}}{n(\omega)} \quad (3.3)$$

where $n(\omega)$ is the frequency-dependent *refraction index*.

The particles of the hadronic cascade and the outgoing lepton polarize the atoms of the medium which emit light (electromagnetic waves) during relaxation. This light is known as *Cherenkov light* or *Cherenkov radiation*. If v exceeds the speed of light in the medium as described, the emitted electromagnetic waves from every point on the particle trajectory can interfere

constructively on a cone around the trajectory. The light emission angle - the Cherenkov angle θ_C - can be calculated with $\beta = v/c$ via:

$$\cos(\theta_C) = \frac{1}{\beta n(\omega)} \quad (3.4)$$

Optical neutrino telescopes use photomultiplier tubes (PMTs) for Cherenkov light detection and the detection principle is shown in Figure 3.1. For example, a muon energy of $E_\mu \approx 162 \text{ MeV}$ ¹ is needed to produce Cherenkov light in South Pole ice.

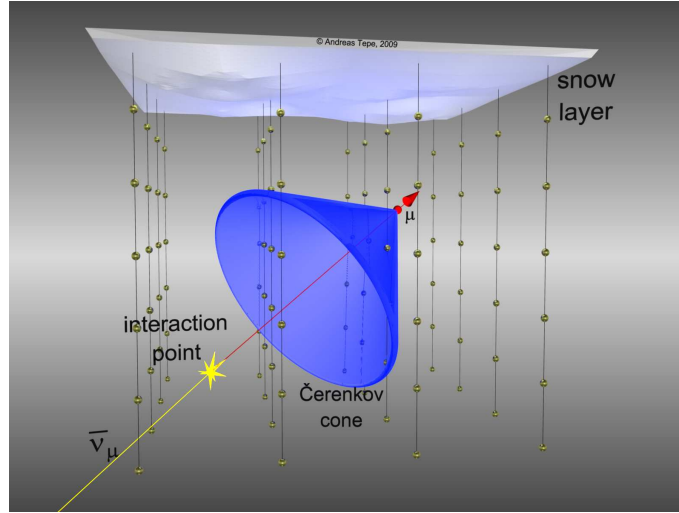


Figure 3.1: Schematic view of the optical detection principle [Tep 09].

Within optical neutrino detectors the three neutrino flavors differ from their interaction signature, which will be described briefly below:

The electron, caused by a CC electron neutrino interaction, will emit *bremstrahlung*. If the emitted bremsstrahlung photons exceed the energy of two times the electron mass ($m_e = 511 \text{ keV}$) $e^+ - e^-$ -pair production is possible. The produced positrons and electrons can produce bremsstrahlung on their own. This *electromagnetic cascade* dies out at the *critical energy* E_c valid for liquids and solids (with the atomic number Z) [Nak 10]:

$${}^1 E_\mu = \frac{m_{\mu 0}}{\sqrt{1-\beta^2}} = \frac{105.7 \text{ MeV}}{\sqrt{1-0.76^2}}$$

$$E_c = \frac{610 \text{ MeV}}{Z + 1.24} \quad (3.5)$$

Below E_c ionization dominates in comparison with bremsstrahlung. Electron neutrino causes a hadronic cascade with a length of < 10 m. Regarding to IceCube detector (see Section 3.1.1), this size is smaller than the minimal optical module spacing, and therefore this cascade causes a point like light signature.

The muon, caused by a CC muon neutrino interaction, has a lifetime of $\tau_\mu = 2.197 \mu s$. With this lifetime and an energy of $E_\mu \approx 1 \text{ TeV}$ the muon travels roughly 2.5 km (through the detector) until it decays. Using the emitted Cherenkov light and measuring the arriving time of photons with PMTs in the detector, the time and the position of the light emission and therefore the emission point of the neutrino in the sky can be calculated. The angular deviation δ_μ of the secondary muon from the primary muon neutrino path is [Lea 00]:

$$\delta_\mu \approx 0.7^\circ \left(\frac{1 \text{ TeV}}{E_{\nu_\mu}} \right)^{0.7} \quad (3.6)$$

The tau, produced in a CC tau neutrino interaction, causes a *double bang event*. At the interaction point the primary hadronic cascade produces light (bang one). The outgoing tau loses energy via Cherenkov light. For example, a tau particle with an energy of $E_\tau \approx 4 \text{ PeV}$ travels 200 m until it decays in an additional cascade (bang two).

The optical Cherenkov light detector *IceCube observatory* will be introduced below.

3.1.1 IceCube observatory

The idea of an optical neutrino detector was driven by the goal of detecting astrophysical neutrino point sources, which are believed to be correlated with cosmic ray production sites. Due to the extremely small neutrino interaction cross section and the expected low fluxes from astrophysical neutrino sources, a large (volume) detector is required. The history of IceCube started with *AMANDA* (Antarctic Myon And Neutrino Detector Array), the predecessor and prototype for IceCube, but it is no longer operating. IceCube is able to detect neutrinos from 100 GeV to more than 10^9 GeV and all components will be described below briefly.

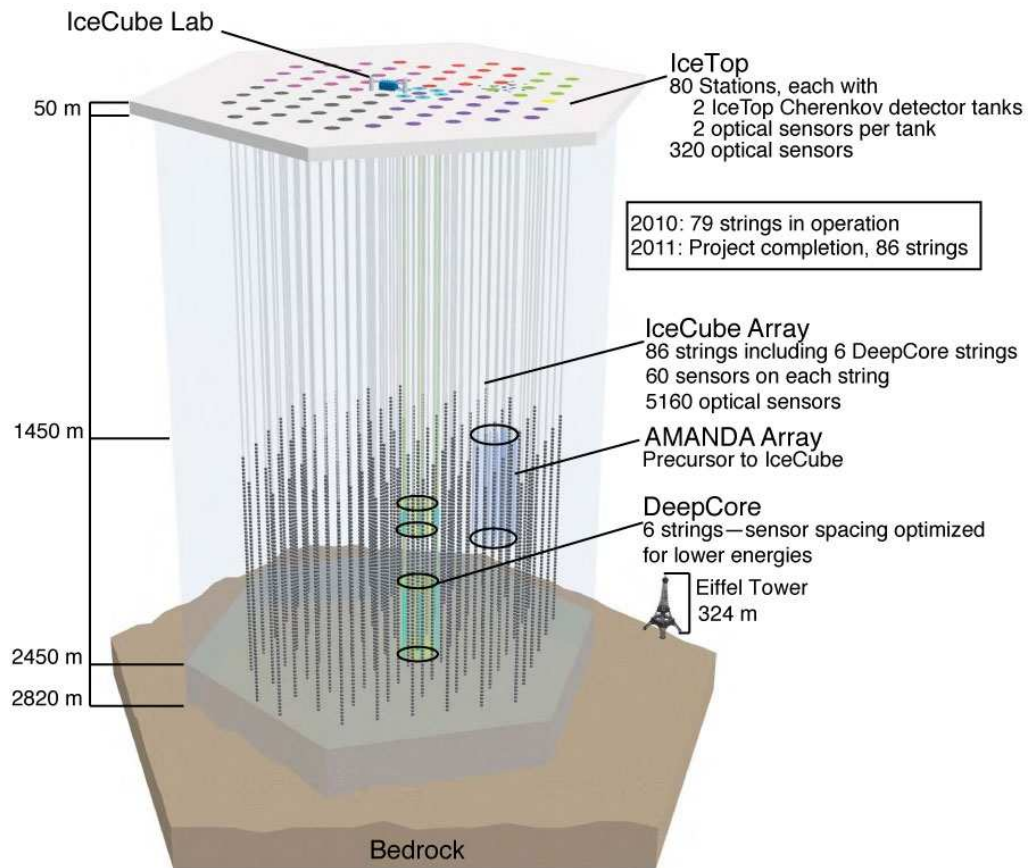


Figure 3.2: The IceCube observatory with its sub detectors.

When completed in austral summer season 2010/2011, the in-ice components of IceCube - the *IceCube Array* - will consist of 86 strings, including 6 strings forming *DeepCore*. In total 5160 so called *Digital Optical Modules* (DOMs) are installed on these vertical strings (installed via hot water drill) at a depth of between 1450 m and 2450 m in the South Pole ice sheet. At one string 60 DOMs are located (a 10 inch Hamamatsu *photomultiplier tube* (PMT) [Abb10+] together with electronics in a glass pressure sphere building one DOM). The electronics to digitize, time stamp and transmit signals to the central data acquisition system [Abb 09] is located in the IceCube laboratory on the snow surface.

The vertical spacing of the DOMs located at the 80 standard strings (or non *DeepCore* strings) is 17 m. Horizontally the strings are 125 m apart and spread out in a triangular grid over an area of 1 km² (see Figure 3.4). The entire instrumented volume will cover 1 km³.

The 60 DOMs per *DeepCore* string are high quantum efficiency DOMs and installed below 1750 m in the deep, exceptionally clear ice. Taking into account the dust layer at a depth of around 2000 m an ice region with a thickness of about 100 m is not instrumented (see Figure 3.3). With a closer spacing in horizontal (75 m) and vertical direction in comparison with the standard IceCube strings these strings are located inside the center of IceCube. Using the outer strings as a veto against atmospheric muons the sensitivity of the IceCube detector for lower energies (< 100 GeV) can be enhanced [Wie 09].

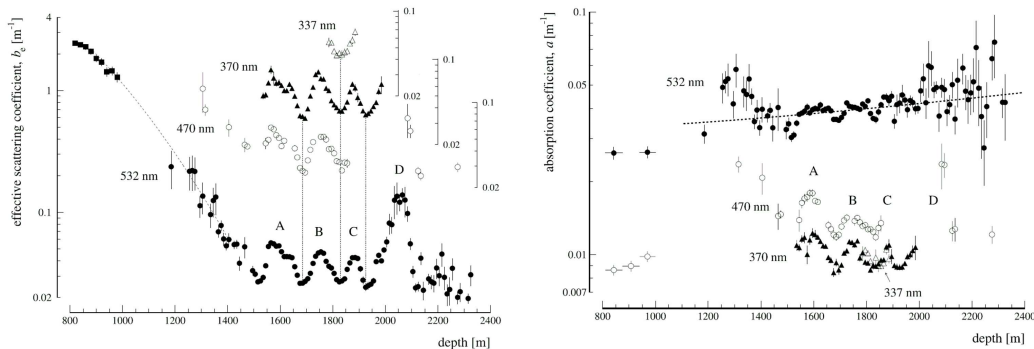


Figure 3.3: Depth dependent effective scattering coefficient and absorption coefficient for different wavelengths measured with light sources in South Pole ice. The four bumps correspond to dust layers of different ages: 38,000 yr (A), 46,500 yr (B), 53,500 yr (C) and 65,000 yr (D) [Ack 06].

Inside the snow surface, close to the holes of each 80 standard strings, there are two *IceTop tanks* called *stations* building the *IceTop air shower detector*. The 160 clear-ice tanks are equipped with two DOMs (low-gain and high-gain). The air showers are detected via a high energetic muon or electron passing through a tank causing Cherenkov light. Beside the possibility of running IceTop as a stand alone air shower detector, it allows a calibration of the in-ice components using atmospheric muons and acts as a veto detector for atmospheric muons [Sta 09] For recent results see [Feu 10] and [Kis 10].

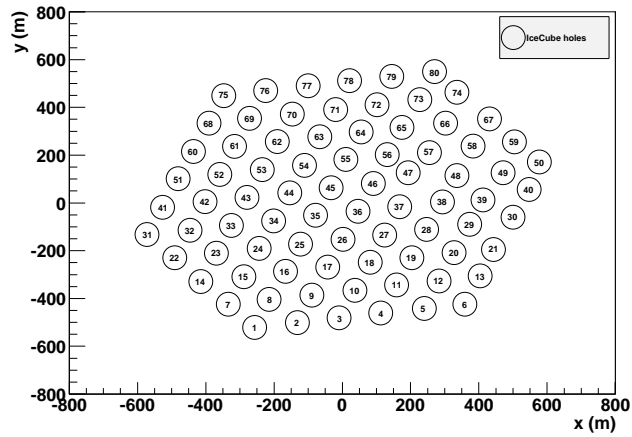


Figure 3.4: The IceCube array footprint without DeepCore.

As a possible extension of the optical neutrino detection mechanism towards a hybrid detector the acoustical and radio detection technique will be introduced in the following two sections.

3.2 Acoustical detection mechanism

This section describes the acoustic signal production and detection due to a particle interaction with matter.

A theoretical work - the *thermo acoustic model* - about the production of an acoustic signal in water (or fluid media) caused by energy deposition due to particle interaction was published in 1979 by G. A. Askarian et al. [Ask 79]. This was verified experimentally by L. Sulak and J. Learned using proton beams [Sul 79].

A local heating of temperature ΔT caused by the deposition of energy E in volume V is determined by

$$\Delta T = \frac{E}{\rho C_p V} \quad (3.7)$$

with the heat capacitance C_p at constant pressure and the density ρ of the medium. The expansion of the volume due to the temperature increase can be calculated with:

$$\Delta V = \alpha V \Delta T = \frac{\alpha}{\rho C_p} E \quad (3.8)$$

Now, using the definition of thermal expansion coefficient $\alpha = 1/V(\partial V/\partial T)$ and the energy density $\epsilon = E/V$ Equation 3.8 becomes:

$$\frac{\Delta V}{V} = \frac{\alpha}{\rho C_p} \epsilon \quad (3.9)$$

With Equation 3.9 as forcing term the inhomogeneous wave equation describes the evolution in time t and space \vec{r} of the pressure density $p(\vec{r}, t)$ when the energy density $\epsilon(\vec{r}, t)$ is deposited in the medium:

$$\nabla^2 p(\vec{r}, t) - \frac{1}{v_l^2} \frac{\partial^2 p(\vec{r}, t)}{\partial t^2} = -\frac{\alpha}{\rho C_p} \frac{\partial^2 \epsilon(\vec{r}, t)}{\partial t^2} \quad (3.10)$$

v_l represents the longitudinal speed of sound.

Using the Kirchoff integral to solve the equation one gets the pressure at a certain time and place:

$$p(\vec{r}, t) = \frac{\alpha}{4\pi\rho C_p} \int \frac{d^3 r'}{|\vec{r} - \vec{r}'|} \frac{\partial^2}{\partial t^2} \epsilon \left(\vec{r}', t - \frac{|\vec{r} - \vec{r}'|}{v_l} \right) \quad (3.11)$$

In a very simplified model, it is assumed that the energy of a neutrino induced particle cascade is released instantaneously² within a cylindrical volume of length L and diameter d (see Figure 3.5). With these assumptions and $L \ll R \ll L^2\pi/2d$, where R is the distance perpendicular to the cascade, the pressure will decrease proportional to \sqrt{R} [Ask 79]:

$$p(R) \propto f_{peak}^2 \frac{\alpha}{\rho C_p} \frac{E}{\sqrt{R}} \quad (3.12)$$

$f_{peak} = v_l/2d$ is the main component of the spectral content of the signal.

A hadronic cascade caused by a UHE neutrino interaction ($E_\nu > 1$ PeV) covers a cylindrical volume of $L = 5 - 10$ m and a diameter d of a few cm. Therefore, the maximum frequency content is $f_{peak} \approx 20$ kHz.

As mentioned above the expected pressure pulse (in time domain), at a fixed location, shows a bipolar shape. In Figure 3.6 pressure amplitudes as function of time at a position corresponding to the maximum of the shower and perpendicular to shower axis for three different energy distribution models is shown [Ded 97].

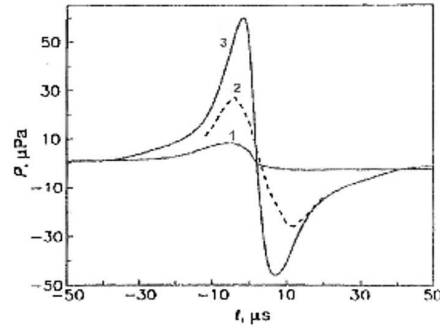
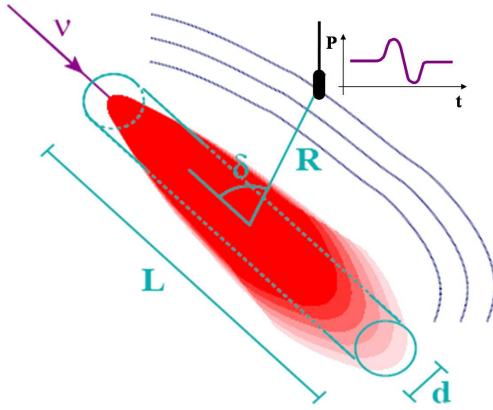


Figure 3.5: Schematic drawing of hadronic cascade with pressure wave and bipolar signal [Bös 03].

Figure 3.6: Shape of bipolar pulses according to three different thermo acoustic models; (1) Learned, (2) Askarian and (3) Dedenko [Ded 97].

²Time scale for energy deposition is much shorter than for heat dissipation in the medium.

To investigate the difference in acoustic signal strength for different interaction media, the *Grüneisen parameter* γ_G , which is proportional to

$$\gamma_G = \langle v_l \rangle^2 \frac{\alpha}{C_p} \quad (3.13)$$

can be used. For a certain medium this parameter expresses the efficiency of the conversation between heat and elastic energy. The *Grüneisen parameter* allows for a comparison of media with different physical properties, e. g. sea water, salt and ice. Table 3.1 shows that an acoustic signal produced by a certain energy deposition in ice is 7.3 times higher than the signal produced by the same energy in sea water.

		Sea water	Salt	Ice
Temperature	T in °C	15	30	-51
Density	ρ in $\frac{\text{g}}{\text{cm}^3}$	1	2.16	0.92
Speed of sound (longitudinal)	v_l in $\frac{\text{m}}{\text{s}}$	1530	4560	3920
Thermal expansion coefficient	α in $\frac{10^{-5}}{\text{K}}$	25.5	11.6	12.5
Heat capacitance	C_p in $\frac{\text{J}}{\text{kg}\cdot\text{K}}$	3900	839	1720
Peak frequency	f_{peak} in kHz	7.7	42	20
Grüneisen parameter	γ_G	0.153	2.87	1.12

Table 3.1: Parameters for comparison between different media for acoustic neutrino detection [Pri 06]

For the detection of acoustic signals *piezo electric elements* (also piezo or piezo elements) are used. These are ceramic or crystal (e. g. lead zirconate titanate, PZT) based devices in various shapes and sizes which own linear electromechanical interaction between the mechanical and the electrical state. If an external mechanical force is applied (e. g. acoustic pressure wave) a resulting measurable internal electrical charge (voltage) is generated. This is a reversible process and known as the *piezoelectric effect*. Using the *inverse piezoelectric effect* (applying an electrical field causes the internal generation of a mechanical force) to build acoustic transmitters.

In several detectors and test beds (see below) the piezo electric elements used as receivers or transmitters are e. g. coated and amplifiers for a suitable signal strength are used.

Beside the South Pole Acoustic Test Setup deployed in ice (described in Chapter 4 the following projects are in-water acoustic experiments (in alphabetical order):

- **ACORNE** This is the *Acoustic COsmic Ray Neutrino Experiment* consisting of eight hydrophones and representing the military array near the Scottish coast. It has been in operation since December 2005 [Bev 08].
- **AMADEUS** The (*Antares Modules for Acoustic DEtection Under the Sea*) test system (see [Agu 10] for details) is integrated into the optical neutrino telescope ANTARES [Agu 06], consisting of 36 hydrophones and is located in the Mediterranean Sea near Marseilles.
- **O ν DE** The four broadband hydrophones of the *Ocean Noise Detection Experiment* are included into the NEMO project and were in operation from 2005 to 2006 [Ric 08].
- **SAUND** The *Study of Acoustic Ultra-high energy Neutrino Detection* is currently present in phase two and consists of a 49 hydrophones military array near Bahamas [Kur 08]. Into the first phase SAUND consisted of seven hydrophones and was in operation from 2004 to 2005.

3.3 Radio detection mechanism

The radio detection principle is based on theoretical work by Askarian [Ask 62] which predicts that the number of electrons would be superior to the number of positrons by about 20% within a cascade. Reasons for that are the positron annihilation and the electron Compton scattering by photons. The asymmetry in charge causes an unbalanced electrical field.

A typical frequency for radio emission is 1 GHz. The index of refraction for ice at this frequency is $n \approx 1.78$ and therefore the radio Cherenkov emission angle is $\Theta_C = 56^\circ$ [Sta 91].

The real maximum frequency is defined via the lateral distribution of the shower and the width of the peak is inversely proportional to the longitudinal depth of the shower; if the longitudinal shower length and therefore the maximum energy increases then the peak width decreases (see Figure 3.7).

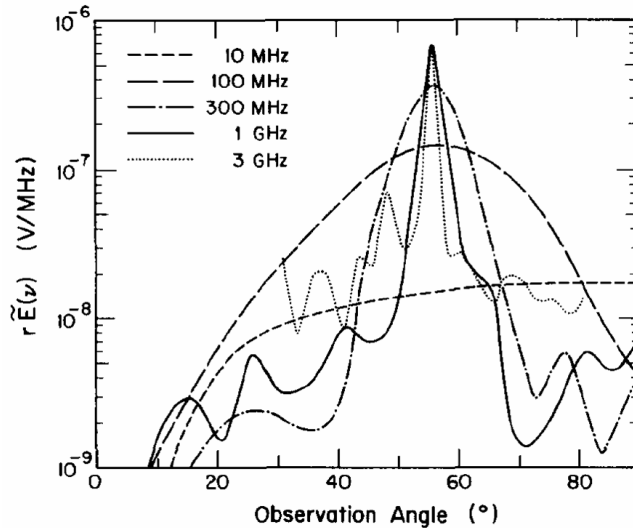


Figure 3.7: The electric field strength caused by a 10 TeV electron versus observation angle (polar angle of the radiation with respect to the longitudinal shower axis) [Sta 91].

To receive this type of pulses, radio antennas are used. With the *Radio Ice Cherenkov Experiment* (RICE) cylindrical dipole antennas (oriented vertically) were installed inside the bore holes, used for the deployment of the AMANDA detector, to investigate the environmental conditions. RICE consists of 18 radio antennas which are distributed over a $200 \cdot 200 \cdot 200 \text{ m}^3$ cube at a depth of between 100 m and 300 m in the snow (see [All 97] for details). An overview of current in-ice radio detectors and planned in-ice and on-ice detectors can be found in [Auf 10].

Chapter 4

South Pole Acoustic Test Setup

On the way to a big acoustical neutrino detector or hybrid neutrino detector the acoustical ice properties e. g. the sound speed, acoustical attenuation length and absolute noise level are essential. To answer these questions the South Pole Acoustic Test Setup (SPATS), presented in Section 4.1, was permanently installed inside IceCube holes at the geographic South Pole.

A retrievable transmitter - the pinger -, to multiply the transmitter and sensor combinations for attenuation length analysis was developed and used in three consecutive deployment seasons. Details will be discussed in Section 4.2.

This chapter ends with the presentation of recent SPATS results regarding the speed of sound (Section 4.3.1) and the acoustical attenuation length (Section 4.3.2).

4.1 Permanently deployed in-ice hardware

In the austral summer season 2006/2007 three strings (A-C) of the South Pole Acoustic Test Setup (SPATS) were installed after the IceCube strings in the upper part of IceCube holes down to 400 m depth. Each of these SPATS strings consist of seven *acoustic stages* located at a depths of 80 m, 100 m, 140 m, 190 m, 250 m, 320 m, and 400 m and each stage contains one transmitter and one sensor housing.

On Christmas Eve 2007 (season 2007/2008) a fourth SPATS string (D) with advanced SPATS sensors and two HADES sensors (developed in this thesis) was deployed. in comparison with the first three strings, string D con-

sists also of seven acoustic stages, but the spacing is different. These stages are located at depths of 140 m, 190 m, 250 m, 320 m, 400 m, 430 m and 500 m.

Each acoustic string is connected to an *Acoustic Junction Box* (AJB) at the surface. This is an aluminum box buried under roughly 2 m of snow. Each AJB contains a PC, called *string PC*, and the electronic components necessary to digitize all signals. All four AJBs are connected to another PC, called *master PC*, located in the IceCube laboratory. There, the data is stored until it is transferred to a data storage in the northern hemisphere by satellite or transferred onto a tape at the South Pole. Technical details about the SPATS array can be found in [Abd ip].

An artist view of the SPATS array layout is pictured in Figure 4.1 and the (horizontal) locations within the IceCube detector is shown within the IceCube footprint in Figure 4.2.

The different types of sensors, first and second generation of SPATS sensors and the HADES sensors, will be described in detail in Chapter 5.

We refer to each sensor channel by the string identifier letter (A, B C, or D), a capital S for sensor, the number of the stage (1-7, counting from top to bottom) and the number of the channel (0-2). For example, AS6(0) indicates channel 0 of the sensor module number 6 of string A. The spacing of all four strings from 140 m to 400 m is equal, but the shallower two stages of strings A-C are installed deeper on string D down to 500 m. Using the notation described above, the number of a stage located at string D is not present at the same depth as the acoustic stage of the same number of string A, B or C!

The transmitters, deployed with SPATS, will be briefly introduced now. The steel pressure vessel of each transmitter contains a high-voltage pulse generator board and a temperature or pressure sensor. A ring shaped piezo ceramic element, cast in epoxy for electrical insulation, is located approximately 13 cm below the steel housing and emits a broadband pulse, driven by the pulse generator board. The amplitude of the transmitted acoustic pulse can be modified by adjusting the steering voltage and the trigger pulse length. We refer to a certain transmitter via the string identifier letter, a capital T for transmitter and the number of the stage (only one transmitter per stage). Therefore BT2 represents the transmitter on string B at level 2 (100 m deep).

For example, a transmitter pulse in frequency domain, emitted by transmitter BT4 and received by DS6(2) (HADES B) is shown in Figure 4.3.

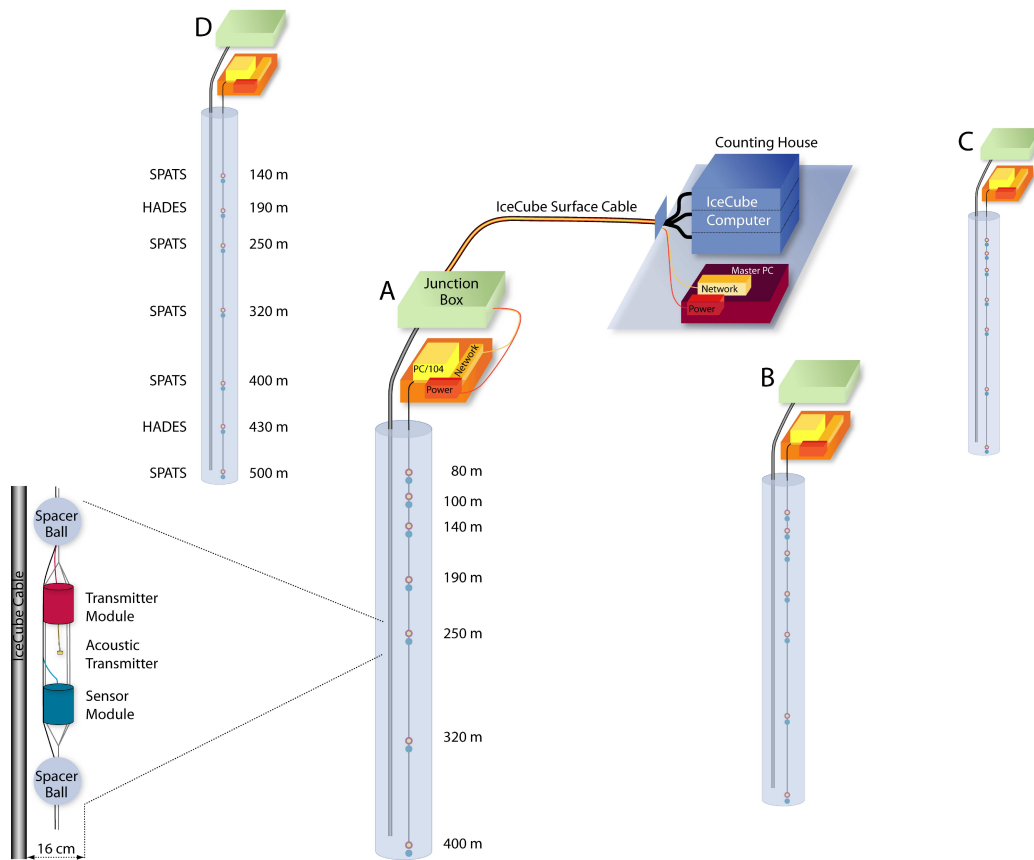


Figure 4.1: SPATS array layout.

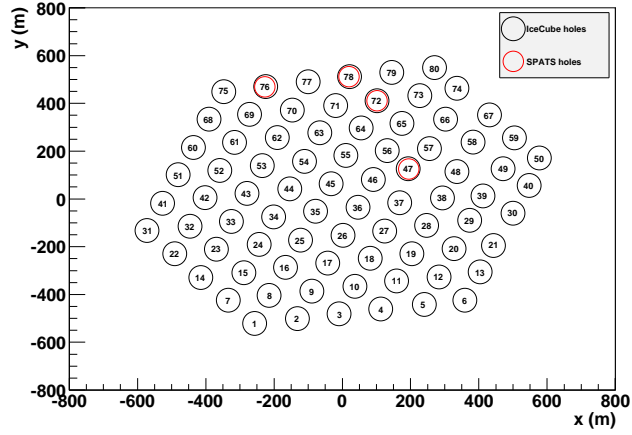


Figure 4.2: SPATS geometry inside the IceCube detector (without the location of holes used for DeepCore strings). IceCube holes with deployed SPATS strings are marked with red open circles. SPATS strings A, B, C and D are deployed in IceCube holes # 78, # 72, # 47 and # 76 respectively.

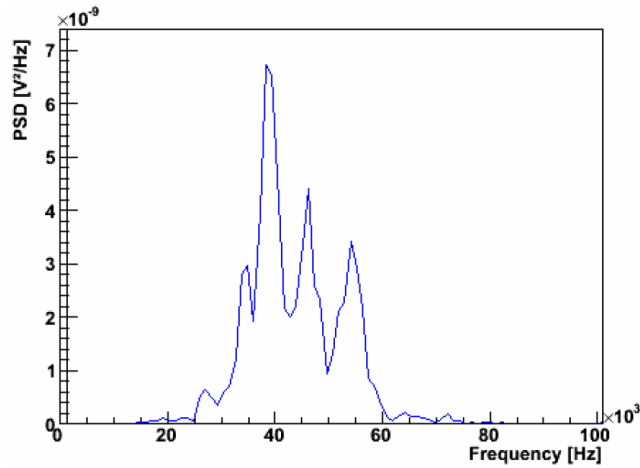


Figure 4.3: Fourier spectrum of transmitter pulse emitted by transmitter T4 at string B (depth 190 m) and received by HADES B at string D (depth 430 m).

4.2 Retrievable transmitter - the pinger

The SPATS array was installed to measure (among other things mentioned earlier) the acoustical attenuation length in South Pole ice. Therefore, sensors and transmitters were permanently deployed which offered several distances for an attenuation measurement between multiple sensor and transmitter combinations. This type of measurement is based on the assumption that the sensor/transmitter combinations behave similar (e. g. in sensitivity/transmittivity) to each other. It is known that each sensor module can rotate during the deployment and freeze-in inside the hole and even the exact horizontal position in the hole is unknown after the deployment. In addition to that the sensor sensitivity and transmitter transmittivity depend on both the azimuthal and the zenith angle with the consequence that an attenuation length analysis with reasonable uncertainties based only on simple sensor/transmitter combinations is not possible.

To reduce the uncertainties due to different transmitters a single powerful retrievable transmitter for use in water filled IceCube holes prior to IceCube string deployment was developed. This retrievable transmitter is called *the pinger* and the detailed development and testing steps can be found in [Tos 10]. The pinger consists of three components: the Acoustic Pinger Box (APB), the high voltage pulser and the transmitting piezo element. All components will be explained in detail in the following and the complete pinger setup is shown in Figure 8.38.

The *Acoustic Pinger Box* (APB) weights of about 10 kg and contains a 24 V sealed lead acid rechargeable battery pack specified to work at low temperatures down to -65°C to drive the *high voltage pulser board* (see Figure 8.38). It is possible to connect a GPS receiver to the APB and the GPS clock is used to generate a Pulse Per Second (PPS) trigger pulse.

The high voltage pulser board is based on a modified transmitter board and is located in a steel housing (diameter: 10 cm; height: 15 cm). This board generates the high voltage pulse which excites the piezo element of the pinger ball. The board hardware was modified during the different deployment seasons and details can be found in the corresponding sections (see below).

As a transmitting element the ITC-1001¹ was chosen. It consists of two hemispheres in high precision Channelite-5400 lead zirconate titanate ceramic which form the transmitter ball and emits a spherical beam [ITC 10]. The specified maximum working depth is 1250 m.

For data taking at the South Pole the transmitting piezo together with the high voltage pulser were connected to the APB via a ≈ 2700 m long four wire cable spooled on the so called *Robertson winch*. The voltage pulser and the transmitter (connected via 2 m cable) were lowered in the hole and the APB provided the power and the trigger signal from the top of the hole. The pinger ball (in operation) was stopped for a certain time at depth equipped with acoustic sensors. When analyzing received pinger pulses with SPATS sensors, called *pinger data*, one needs to keep the following things in mind:

- The position of the sensors inside the frozen IceCube hole is not well determined. All SPATS strings are equipped with spacer balls with a diameter of 16 cm but the hole diameter is ≈ 70 cm. In addition the position of the IceCube cable is unknown, too. This could shadow the sensor in the case of a specific location of the pinger.
- After the deployment of the SPATS strings and the IceCube strings the water refreezes. This so called *hole ice* is not as crystal clear as the *bulk ice*. This “bad quality” ice could lead to an inhomogeneous absorption or scattering near the sensors and / or to transmission inhomogeneities for the pinger signal.
- The recorded pinger waveforms contain a signal and a noise contribution and to receive the real signal the noise must be correctly subtracted.
- Each string PC uses a single clock to drive its analog to digital converters (ADCs), which are used to sample and record the sensor waveforms. The sample time (number of samples actually processed) deviates from the true time (number of samples that should have been processed according to the absolute amount of time that has passed) by an amount that increases over time, or in a simplified way: the actual sampling frequency differs from the nominal sampling frequency. This is called *clock drift* and the deviation is typically of the order of a few parts per million. The clocks drift at a rate of 10 parts per million (positive or negative). These clock drifts need to be corrected when waveforms or waveform fragments are averaged.

¹International Transducer Corporation; <http://www.itc-transducers.com/>

- The dynamic range of the sensors is limited and therefore the sending amplitude of the pinger has to be chosen in a way that the sensors do not saturate at the nearest distance and detect a reliable signal at the furthest distance.

Up to now the pinger has been used in three consecutive seasons and was deployed for the first in time in season 2007/2008. For this thesis, only the first two pinger seasons are of interest and they will be discussed in more detail in comparison with the third season in the following Sections.

4.2.1 First pinger season in 2007/2008

Before deployment at South Pole, the real electric pulse produced by the high voltage pulser board exciting the load on the transmitter was measured in laboratory [Tos 10]. This is called the *high voltage read back* (HVRB) signal as shown in Figure 4.4. Due to the short driving pulse the emitted signal by the pinger ball is broadband with a predominance in the 10-30 kHz range as specified by the Transmit Voltage Response (TVR) provided by the company. The TVR in time and frequency domain is pictured in Figure 4.5.

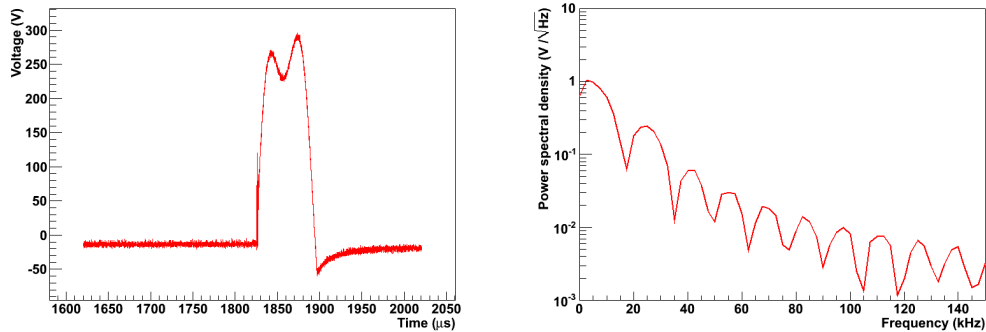


Figure 4.4: Pinger HVRB pulse in time and frequency domain (Voltage values are scaled by factor 500) [Tos 10] [Kar pr].

In this pinger season all three channels in the same SPATS sensor or one of the HADES sensors were taking data one at a time for 9 seconds. The pinger was pulsed at 1 Hz repetition rate (triggered by the PPS of the GPS clock), so 9 pulses were recorded in each waveform. The data taking script looped over the channels and sensors on one selected string, and it took a time of about 4 minutes to record 3×7 channels on each string. Therefore a

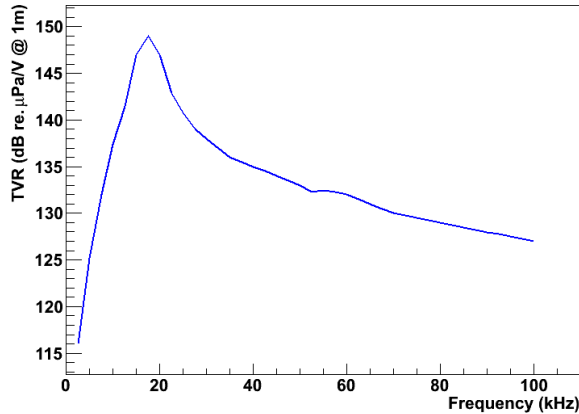


Figure 4.5: Pingr TVR [Kar pr].

stopping time of 4-5 minutes at each selected depth was established to get at least one waveform recorded for each channel during the stop of the pingr at each level. The data taking between different strings was started manually and was completely asynchronous.

The pingr data collected during this season were found to be affected by many unforeseen effects (see [Tos 10] for details) in such a way that the recorded waveforms were so unstable in amplitude that they could not be used for attenuation length measurement. This first year pingr data was suitable for a depth depended sound speed analysis (see Section 4.3.1).

4.2.2 Second pingr season in 2008/2009

Starting with this season, the pingr ball position inside the water filled hole was stabilized around the center of the hole with metal springs, called *centralizers*. The updated pingr is shown in Figure 4.6.

In comparison with the first pingr season the pingr pulse repetition rate was changed from 1 Hz to 10 Hz and 8 Hz and the recorded time window has been increased. The pingr was deployed in IceCube holes #19, #28, #37 and #5.

For attenuation length analysis one sensor channel at a time was used when the pingr is located at the same sensor depth in different vertical distances (different holes) with none or a very small azimuthal angle variation.

With these requirements the influences of the sensor to sensor variation and the azimuthal and zenith sensitivity variation of each sensor are minimized and the acoustical attenuation length could be derived. See Section 4.3.2 for details.

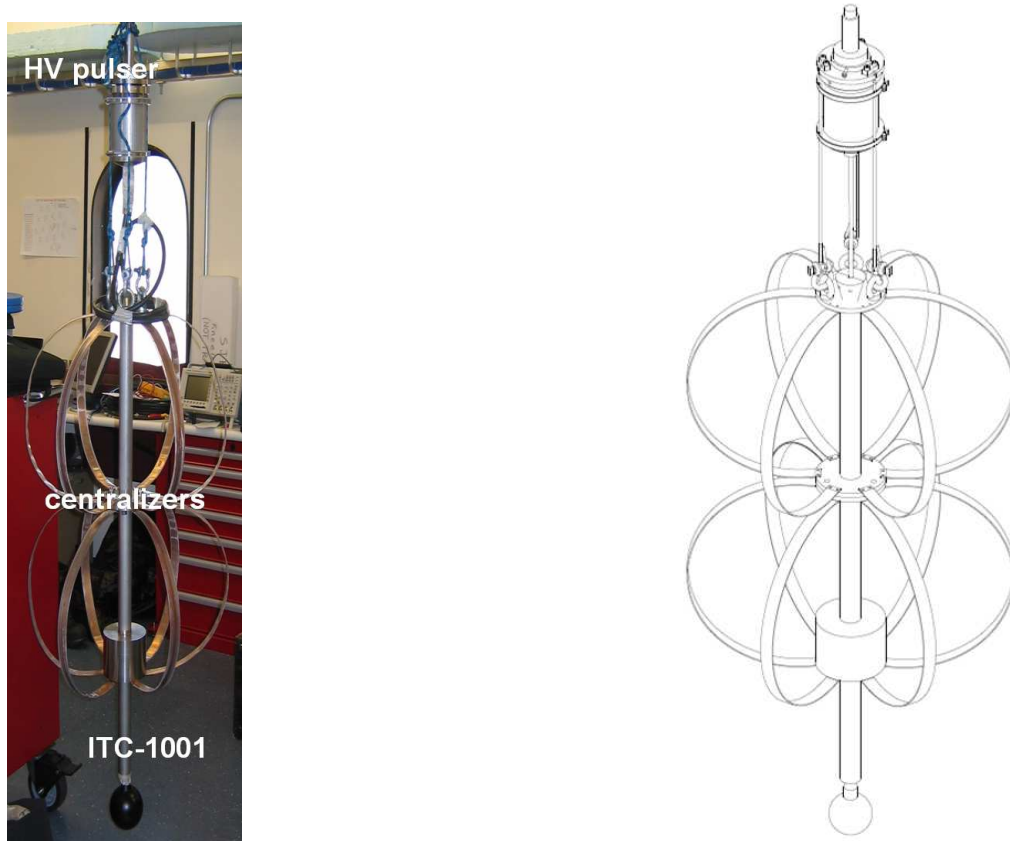


Figure 4.6: The pinger equipped with centralizers (picture and drawing adapted from [Tos pr] and [Hel pr] respectively).

4.2.3 Third pinger season in 2009/2010

In this season the pinger (with centralizers) was used in *burst mode*. Therefore a new voltage board was developed and several sine wave cycles at three different frequencies for a frequency depended attenuation length analysis were sent. The analysis is still ongoing and results will be published in [AbdPhD].

4.3 Recent SPATS results

4.3.1 Sound speed in deep South Pole ice

Several SPATS sensors of string B and D were used to measure the sound speed via the exact signal emission and receiving time and the known distance between transmitter and sensors. As sound source the described pinger was used in season 2007/2008. The pinger was lowered in to string B and D nearby water filled holes (nominal horizontal distance: 125 m).

In addition to the expected pressure waves (P-waves) shear waves (S-waves) were clearly detected and the sound speed for pressure and shear waves were measured. In the water filled holes shear waves cannot propagate but they were possibly produced by mode conversion at the water / ice interface at the hole wall. If the incident angle were normal, the shear wave would be suppressed, but when the pinger was not in the center of the hole the incident angle was oblique and shear wave production was favored.

For sound speed analysis one needs to take into account that the first 200 m (or 250 m) of the total ice sheet at the South Pole consist of uncompactified surface snow - *the firn* - and this layer provides different acoustical properties in comparison with the rest (fully compactified region - *the bulk ice*).

Figure 4.7 shows the result of the sound speed analysis for pressure and shear waves. For comparison a previous measurement without uncertainty estimation made at seismic frequencies is shown. Details of the analysis can be found in [Abb 10].

A linear fit was applied to the data in the fully compactified region from a depth of 250 to 500 m and results for pressure wave (P-wave) and shear wave (S-wave) are:

$$v_P(375 \text{ m}) = (3878 \pm 12) \text{ m/s} \quad (4.1)$$

$$v_S(375 \text{ m}) = (1975.8 \pm 8.0) \text{ m/s} \quad (4.2)$$

All in all the speed of both pressure and shear waves as a function of depth between 80 and 500 m in South Pole ice have been measured within a precision better than 1 %. In addition to that, between 200 m and 500 m, the

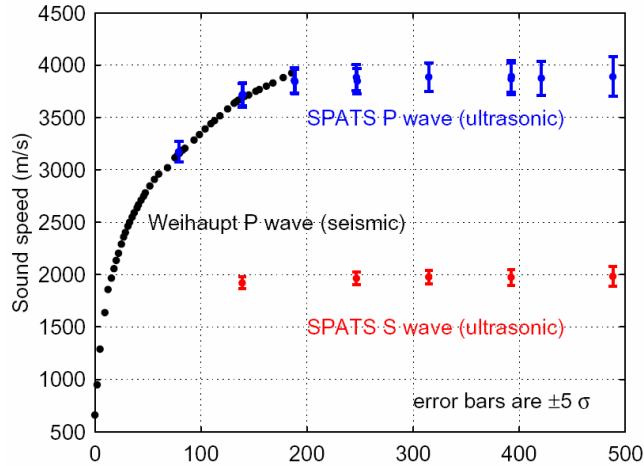


Figure 4.7: Measured sound speed for both pressure waves (P-waves; blue) and shear waves (S-waves; red) at depth of equipped SPATS stages. A previous measurement (black) without uncertainty estimation is shown for comparison [Abb 10].

measured profile is consistent with zero variation of the sound speed with depth.

4.3.2 Acoustical attenuation length

The attenuation of acoustical waves in the South Pole ice is an important quantity and determines the density of acoustic sensors that must be deployed. The number of sensors is mainly responsible for the cost for an acoustic detector with reasonable detection efficiency for neutrino interactions. The acoustic signal, propagating through the ice, is attenuated via a combination of two effects: scattering and absorption [Pri 06].

The acoustic signal is *scattered*, when the pressure wave is deviated (with or without energy loss) from its straight trajectory due to an inhomogeneous medium. In ice the scattering objects are bubbles and ice crystals.

Down to a depth of 1400 m it is assumed that bubbles act as independent scattering centers because their mean distance is larger than their linear dimensions. Below that depth the influence of bubbles on acoustic waves is negligible, because due to the pressure most of the bubbles have been converted to clathrate crystals.

In contrast to that, the crystal grain size increases with depth due to increasing pressure. Measurements, using drilling cores from Greenland and

Antarctica, show that the mean diameter is less than 0.2 cm down to 600 m which increases to a value of 0.4 cm at a depth of 1500 m. Within the frequency range for acoustic detection the wavelength is a few tens of centimeters and therefore much larger than the measured grain size.

Calculations in [Pri 06] using Rayleigh scattering show that the scattering coefficient is proportional to the frequency to the 4th:

$$\alpha_{\text{scat}} \propto f^4 \quad (4.3)$$

When the acoustic wave penetrates the ice multiple interactions with the ice lattice and the grain cause *absorption*. Today, it is assumed that the main contribution to absorption comes from changes in the orientation of the dipole moment of water molecules and to movements of protons from one bond site to another. The *relaxation time* τ_m quantized the internal friction induced by these processes. Up to the frequency f_s the absorption coefficient is proportional to f and above it is independent from frequency:

$$\alpha_{\text{abs}} \propto f \quad \text{for} \quad f < f_s = 1/2\pi\tau_m \quad (4.4)$$

The absorption coefficient was calculated frequency dependent at different temperatures via measurements of the relaxation process by Kuroiwa in 1964 and these results agree with measurements by Bentley and Kohnen (Antarctica in 1976, near Byrd station, -28°) and Brockamp and Kohnen (Greenland in 1965, -22°), see Figure 4.8.

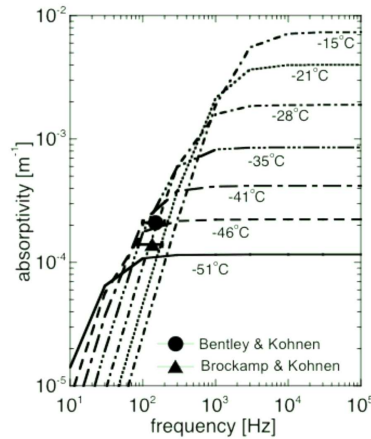


Figure 4.8: Absorption length for different frequencies and temperatures; calculated by Kuroiwa and measured by Bentley and Kohnen and Brockamp und Kohnen [Pri 06].

To investigate the dominant contribution (scattering or absorption) to the attenuation coefficient, the attenuation length needs to be measured in a frequency dependent way to answer the question it is proportional to f to the 4th or linear.

The acoustic sensors of the SPATS array are based on piezo-ceramics and they are excited by the emitted pressure wave. The received signal amplitude A is proportional to the acoustic pressure and for a point source with a spherical $1/\text{distance}(d)$ emission, A scales due to geometry and attenuation to:

$$A = A_0 \frac{d_0}{d} e^{-\alpha d} = A_0 \frac{d_0}{d} e^{-\frac{d}{\lambda}} \quad (4.5)$$

A_0 is characteristic constant which includes the sound emitted at the source and the sensitivity of the receiver, d is the distance to the source, α is the acoustic attenuation coefficient and the attenuation length λ is its inverse. The acoustical attenuation length has been measured via three different approaches described below:

- **Pinger data (season 2008/2009)**

The pinger was used in several water filled IceCube holes and multiple pulses were recorded by selected SPATS sensors.

- **Inter-string data**

The permanent deployed transmitters of the SPATS array sent multiple pulses received by the SPATS sensors.

- **Transient data**

Sound produced in re-freezing IceCube holes was received by the sensors of the SPATS array.

Comparing all three approaches the attenuation analysis using pinger data in time domain was used to derive the final attenuation length:

$$\lambda = 312_{-47}^{+68} \text{ m} \quad (4.6)$$

The results of all analyses agree with an attenuation length of about 300 m within a 20% uncertainty and up to 30 kHz no strong frequency dependence has been found. In addition to that the attenuation length was studied down to a depth of 500 m and there is no indication of a possible depth dependence. Detailed information about each analysis can be found in [Abb 1+].

Chapter 5

Design of acoustic sensors

Sensors for acoustic neutrino detection purpose in South Pole ice should meet the following requirements:

- Quick, simple and reproducible sensor production process with a moderate cost per sensor
- Power consumption of each operating sensor as low as possible
- Signal to noise ratio as good as possible
(high sensitivity with low self-noise)
- Best reachable angular coverage
- Ability to handle the environmental conditions like (water / ice) pressure (100 bar) and low temperatures (-50°C)
- Robust sensor construction to handle the rough deployment process

The first and second generation SPATS sensors are described below followed by the development of the HADES sensor.

5.1 SPATS sensors

All SPATS sensors consist of a steel pressure housing with an inner diameter of 10 cm. Every steel housing contains three piezo ceramic elements (120° apart from each other) with three stage amplifiers (amplification factor: 10^4) and a voltage converter board. Each of the piezo ceramic element represents one *channel* and each channel per sensor can be read out independently; one channel is connected to one ADC and three ADCs are located in each AJB.

The voltage converter board is driven by +24 V and it distributes +10 V to each amplifier board.

Inside the SPATS sensors, deployed with string A-C, three preload screws, connected to a bolt in the middle of the housings, press the ceramic elements through the amplifier boards against the inner wall to ensure good contact with the steel housings and avoid deformation of the modules (see Fig. 5.1). This type of SPATS sensor modules are known as *first generation SPATS sensor*.

Due to the fact that the preload screws and the bolt introduce a mechanical coupling between the three different channels a metal ring is used in the *second generation SPATS sensors*. An inside view of the second generation SPATS sensor housing, used with string D, is shown in Figure 5.2. More details can be found in [Abd ip]



Figure 5.1: Inside view of one first generation SPATS sensor housing (without voltage converter board) used at SPATS strings A-C [Bös 06].

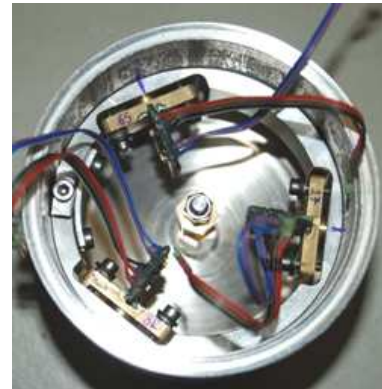


Figure 5.2: Inside view of one second generation SPATS sensor housing (without voltage converter board) used at SPATS string D [Abd ip].

5.2 HADES sensors

HADES - Hydrophone for Acoustic Neutrino Detection at South Pole, was developed as an alternative broadband acoustical sensor with different dynamic range, different sensitivity and different self-noise in comparison with the two types of SPATS sensors.

The HADES sensor consists of a piezo electric element (ring shaped piezo element¹ radial polarized with ID: 20 mm, OD: 24 mm and L: 15 mm; see Figure 5.3) that is connected to an amplifier board (type: Ti TL072) with two step amplification (amplification factor: 6400). The amplifier sends a differential signal via connector (MCIL8M²). In Figure 5.3 the used piezo ceramic element with dimensions is pictured and Figure 5.4 shows the amplifier board. The piezo ceramic element with the installed amplifier is presented on the left side in Figure 5.5.

The HADES sensor is connected to the SPATS array via modified SPATS sensor housings. This sensor housing contains only a voltage converter board (but no piezo ceramic elements), the same type is used within the SPATS sensors, and an connector (MCBH8F²) at the bottom of the sensor housing.

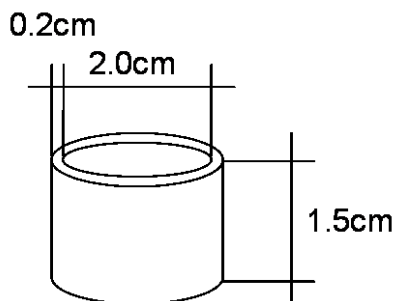


Figure 5.3: Schematic drawing with dimensions of the piezo ceramic element used for HADES sensors.

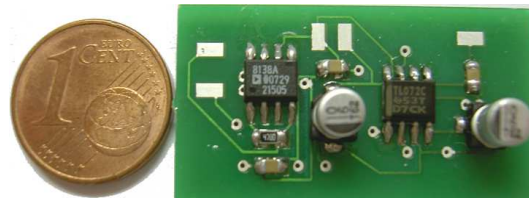


Figure 5.4: Two stage amplifier board; type: Ti TL072, for HADES sensors.

In [Sem 07] several resins have been investigated as potential coating for the piezo electric element and the amplifier board. The resin serves as protec-

¹<http://www.ferroperm-piezo.com>

²<http://subconn.com>



Figure 5.5: HADES sensor without PU coating (left side) and schematic drawing of a HADES sensor (bottom view). The piezo electric element (gray ring) with the amplifier board (green) are surrounded by hard PU coating (right side).

tion against water / ice, needs to be appropriate for the given environmental conditions and was chosen under the aspect of the best reachable *acoustic impedance matching* between ice and the resin. Within this impedance matching the signal reflections at the ice / resin interface can be minimized. Polyurethane³ (PU) resin (see Figure 5.6) yields the best results and this is used as coating for the present HADES sensors.

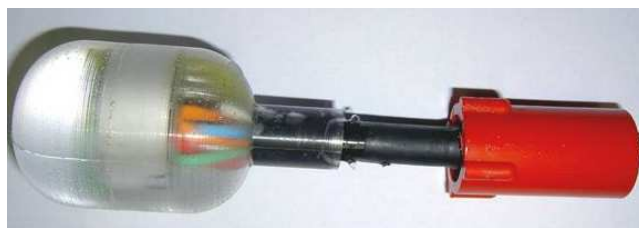


Figure 5.6: HADES sensor: piezo ceramic element with two step amplifier in transparent hard PU resin (left) and the 8 pin connector (right) [Sem 08].

³Resin (Biothan 1770s) and catalyst (Biodur 330) from <http://www.modulor.de/shop>

The two deployed HADES A & B sensors contain in comparison with the SPATS sensors only one channel per sensor. For simplification they are identified via HADES A (at a depth of 140 m) and HADES B (at a depth of 430 m) or in official SPATS notation DS2(2) and DS6(2) respectively. HADES A contains a PZT piezo ceramic element of type Pz-27 ($d_{33} = 425$ pC/N) and HADES B contains a PZT piezo ceramic element of Pz-26 ($d_{33} = 290$ pC/N). Deployment pictures of stage 6 and 2 (containing HADES sensors) are shown in Figure 5.7 and 5.8.



Figure 5.7: Deployment of SPATS string D; stage 6 with HADES B; DS6(2) [Tos pr].

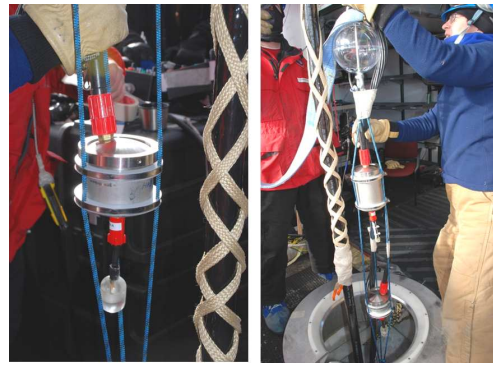


Figure 5.8: Deployment of SPATS string D; stage 2 with HADES A; DS2(2) [Tos pr].

To match the time schedule until deployment of string D only the production of HADES A and B and no characterization or calibration were possible. Therefore two sensors of each type (HADES A (1,2) and HADES B (1,2)) were constructed in the same way as the deployed sensors and were used for characterization and calibration in this thesis. At each laboratory measurement the HADES sensor is directly connected to the voltage converter board and no modified SPATS sensor housing is used. The board is driven via rechargeable batteries to provide voltage with the same quality to the HADES sensor. The differential signal output is converted to a single ended signal via a differential receiver board and can be read out with an oscilloscope or a DAQ.

Commissioning

As described above, every acoustic stage contains a transmitter and a sensor (See Figure 4.1 or 5.7 and 5.8). If a transmitter of a certain stage is fired and the sensor of the same stage receives the signal, then it is called an *intra-stage run*. Intra-stage runs were taken with string D, starting 24 h after deployment. Figure 5.9 shows an intra-stage event of HADES B. The (acoustic) pre-pulse, caused by the charging process when the transmitter electronics generate the pulse and the received acoustic pulse caused by the transmitter itself, is clearly visible.

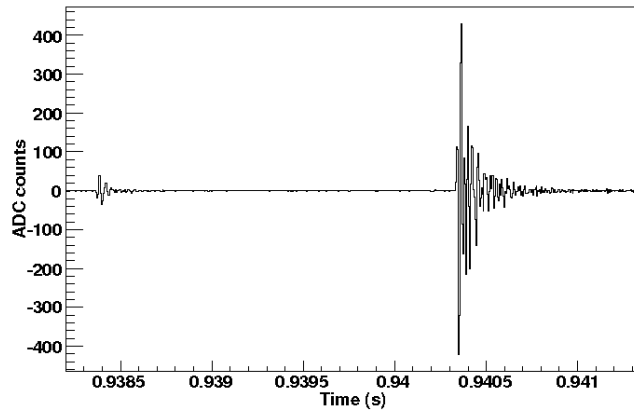


Figure 5.9: Intra-stage event detected with HADES B at a depth of 430 m . The first small pulse represents the pre-pulse, caused by the charging process when the transmitter electronics generate the pulse followed by the received acoustic pulse [Sem 08].

Figure 5.10 shows the measured maximum voltage (peak to peak) of each intra-stage run versus time for HADES B during freeze-in of the string inside the hole. Possible reasons for the increase in received signal strength could include:

- Increase in sensitivity due to temperature decrease since the piezo element is more sensitive at low temperatures (due to decreasing self-noise).
- Better acoustic coupling between sensor and ice or/and transmitter and ice.
- Geometry changes of the hole during freezing.

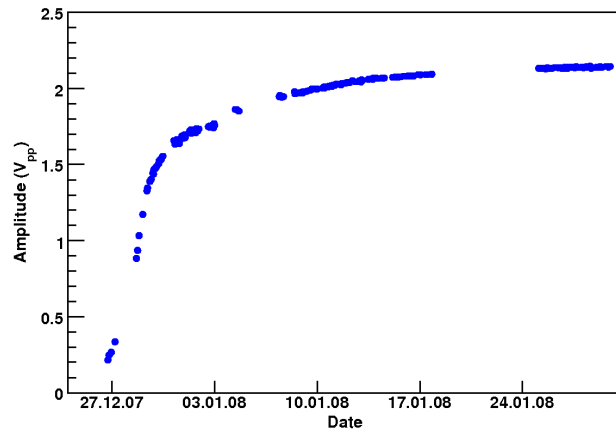


Figure 5.10: Measured peak to peak amplitudes vs. time from intra-stage runs with HADES B [Sem 08].

The amplitude increase by a factor of ≈ 10 is the first in-situ measurement with HADES at this depth, pressure and temperature showing the freezing process.

Chapter 6

Absolute calibration methods

6.1 Comparison method

For a calibration of a hydrophone H via the comparison method an acoustic transmitter T and a calibrated hydrophone, in this thesis Sontortech SQ03 with the sensitivity $S_{\text{SQ03}}(\omega)$ (see below for details), are required. H and SQ03 are located in the same horizontal distance r to the transmitter T (see Figure 6.1). A short pulse (which has a broadband frequency spectrum) is emitted by the transmitter T and recorded with H and SQ03 which provide $U_{\text{H}}(\omega)$ and $U_{\text{SQ03}}(\omega)$, respectively. The sensitivity M_{H} of hydrophone H can be calculated via:

$$M_{\text{H}} = S_{\text{SQ03}}(\omega) \cdot \frac{U_{\text{H}}(\omega)}{U_{\text{SQ03}}(\omega)} \quad (6.1)$$

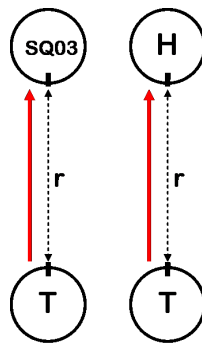


Figure 6.1: Schematic drawing of the setup for calibration via comparison method; Transmitter T, calibrated hydrophone SQ03 and the hydrophone H which one wants to calibrate.

To minimize the effect of azimuthal emission uncertainties from transmitter T, the measurement should be divided into two steps, as shown in Figure 6.1. Send a pulse from T to SQ03 located at distance r and exchange SQ03 with H and repeat the measurement. This guarantees two measurements of the sound field at the same location emitted by transmitter T. As additional uncertainty contributions the SQ03 sensitivity uncertainty (in azimuth) and the accuracy in placing the receivers at distance r to the transmitter need to be taken into account. With the described technique a calibration of hydrophone H under a certain angle can be received. For an average sensitivity this measurement could be repeated with different azimuth (and/or zenith) angle setting(s) of hydrophone H.

The comparison method is a quick and convenient (only few measurements are needed) method for acoustic sensor calibration in water. This technique cannot be used in ice, because no (pre-)calibrated hydrophone for ice is/was available. For an in ice calibration the reciprocity method needs to be applied. Therefore several measurements (more in comparison with the comparison method) are needed.

6.2 Reciprocity calibration method

In contrast to the comparison method described above no calibrated hydrophone is needed for this method. Beside the hydrophone H for calibration one transmitter and one transducer (can act as receiver and transmitter) need to be installed in distance a to the hydrophone (see Figure 6.9). In this thesis both devices (beside H) are transducers distinguished via T_1 and T_2 . Advantages of this will be described below.

This method is based on the equality of electrical power to mechanical power ($U \cdot I = \vec{F} \cdot \vec{v}$) known as the *electroacoustic reciprocity principle*

$$\frac{|E|}{|F|} = \frac{|v|}{|I|} \quad (6.2)$$

with $|E|$ = absolute magnitude of electric voltage, $|I|$ = absolute magnitude of electric current, $|v|$ = magnitude of velocity on diaphragm and $|F|$ = magnitude of force on diaphragm [Uri 83]. In this thesis the general Equation 6.2 needs to be met by the used piezo electric elements (see Section 3.2) to allow the application of the reciprocity method (the mentioned diaphragm represents the surface of the piezo electric element).

The validity of the electroacoustic reciprocity principle for the used transducers have been measured angular dependent in water. Therefore, the energy E_i in the frequency range from 10-50 kHz versus azimuth and zenith angle has been measured when the transducer of interest acts once as transmitter and once as receiver. For example Figure 6.2 shows the deviation of the mean energy (\bar{E}) in percentage calculated via $(\bar{E} - E_i) \cdot 100/\bar{E}$ versus azimuth angle (at a fixed zenith angle). It is clearly visible that the electroacoustic reciprocity principle is fulfilled. This is also true for other measurements at different angle settings which have been done with T_1 and T_2 .

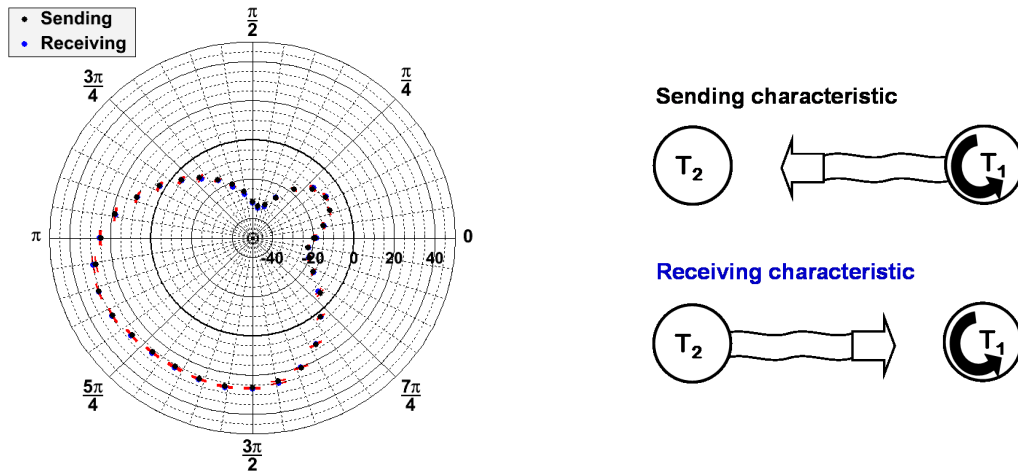


Figure 6.2: Validation of the electroacoustic reciprocity principle. The deviation of the mean energy in percentage ($(\bar{E} - E_i) \cdot 100/\bar{E}$) in the frequency range from 10-50 kHz on the radial axis versus azimuth angle (at fixed zenith angle) when T_1 acts as transmitter and receiver.

Now, the sensitivity M_H of hydrophone H using the reciprocity method will be derived:

The sensitivity M of a hydrophone is defined via the voltage U measured when an acoustic pressure p is applied:

$$M = \frac{U}{p} \quad (6.3)$$

The ratio of the acoustic pressure p_0 , measured at distance r_0 , and the transducer driving current I describes the sending capability S of the transducer:

$$S = \frac{p_0}{I} \quad (6.4)$$

The reciprocity parameter J_x is defined via:

$$J_x = M/S \quad (6.5)$$

S and J_x depend on the wave propagation conditions in the experimental setup. The wave propagation conditions are determined from the length L of the transducer, the distance r between transducer and receiver and the desired frequency range f or rather λ . A relatively long transducer close to the receiver ($r \leq L^2/\lambda$) would require the cylindrical reciprocity parameter J_c whereas a short transducer in a large distance would require the spherical reciprocity parameter J_s . A flat faced piston like transducer with area A calibrated at distances $r \leq A/\lambda$ would require the plane wave parameter. All three reciprocity parameters will be discussed in detail after the derivation of the general sensitivity formula using J_x .

The measurements, needed for the sensitivity calculation, can be divided into two steps. In the first step, T_1 is driven with a current I_{T_1} , and the received voltages U_1 and U_2 are measured in H and T_2 , respectively. In the second step, T_2 is driven with the current I_{T_2} , and the voltage U'_1 is measured in H. This configuration is known as *type T₂ setup* (see Figure 6.9, right side) and more details about different setup configurations will be given below.

Assuming that T_1 emits a sound wave with azimuthal symmetry, both T_2 and H should receive the same pressure amplitude $p_{T_2} = p_H$ in step one. Equation 6.3 leads to:

$$\frac{M_H}{U_1} = \frac{M_{T_2}}{U_2} \quad (6.6)$$

Since the distances between T_1 to H and T_2 to H are equal, the ratio of U_1 and U'_1 only depends on the sending capabilities and the driving voltage I_x of T_1 and T_2 :

$$\frac{S_{T_1} I_{T_1}}{U_1} = \frac{S_{T_2} I_{T_2}}{U'_1} \quad (6.7)$$

Now, using Equation 6.3 to define the sensitivity M_H of hydrophone H:

$$M_H = \frac{U_1}{p_1(a)} \quad (6.8)$$

As shown below, only measurements using far field conditions (spherical wave expansion) are used in this thesis and therefore the pressure $p_1(a)$ can be calculated combining Equation 6.4 and the far field $p(r)$ from Table 6.1:

$$S_{T_1} = \frac{p_1(a)}{I_{T_1}} \frac{a}{r_0} \quad (6.9)$$

Multiplying Equation 6.8 and 6.9 yields:

$$M_H S_{T_1} = \frac{U_1}{I_{T_1}} \frac{a}{r_0} \quad (6.10)$$

Using Equation 6.6 and 6.7 to calculate $M_H S_{T_1}$ we get:

$$M_H S_{T_1} = \frac{U_1^2}{U_1' U_2} \frac{I_{T_2}}{I_{T_1}} M_{T_2} S_{T_2} \quad (6.11)$$

Combining Equation 6.10 with 6.11 yields:

$$M_{T_2} S_{T_2} = \frac{U_1' U_2}{U_1 I_{T_2}} \frac{a}{r_0} \quad (6.12)$$

Now, we use Equation 6.12 and apply the reciprocity condition (presented in Equation 6.5) for T_2 ¹:

$$M_{T_2} = \sqrt{J_x \frac{U_1' U_2}{U_1 I_{T_2}} \frac{a}{r_0}} \quad (6.13)$$

Using Equation 6.6 together with Equation 6.13 we obtain the desired M_H :

$$M_H = \sqrt{J_x \frac{U_1 U_1'}{U_2 I_{T_2}} \frac{a}{r_0}} \quad (6.14)$$

To derive the different reciprocity parameters shown below, J_x is defined as $J_x = M/S$ (see Equation 6.5) with $M = E/P_i$, where P_i represents the incident sound field and $S = P_r/I$, where P_r represents the generated sound field at distance r , is needed. The incident sound field P_i is defined via $P_i = F/A$, where F represents the force on the diaphragm area A [Uri 83].

¹Starting with simplified Equation 6.12:

$$MS = X \rightarrow M = \frac{X}{S} \rightarrow M^2 = \frac{M}{S} X \xrightarrow{\text{Eq. 6.5}} M = \sqrt{JX}$$

Plane wave reciprocity parameter J_p

When a transducer produces plane waves, the produced pressure P_r at distance r with fluid density ρ , speed of sound c , and diaphragm velocity v can be calculated via [Sim 49]:

$$P_r = \rho cv \quad (6.15)$$

When the transducer is acting as receiver of a plane pressure wave of pressure P_i , the force F on the area A is represented via:

$$F = 2AP_i \quad (6.16)$$

Inserting both equations in the electroacoustic reciprocity principle (see Equation 6.2) this yields:

$$\frac{E}{2AP_i} = \frac{P_r}{\rho c I} \quad (6.17)$$

Applying now the definition of the reciprocity parameter (see Equation 6.5) one gets the *plane wave reciprocity parameter* [Sim 49]:

$$J_p = \frac{M}{S} = \frac{E/P_i}{P_r/I} = \frac{2A}{\rho c} = \frac{2}{\rho c} (\lambda r)^0 A \quad (6.18)$$

Cylindrical wave reciprocity parameter J_c

When the transducer is a pulsating cylinder, with radius a , generating cylindrical waves, the pressure at distance r is [Mor 84]:

$$P_r = \pi \rho a v \sqrt{\frac{cf}{r}} \quad (6.19)$$

where f is frequency.

The surface area A of a cylindrical transducer with length L is:

$$A = 2\pi a L \quad (6.20)$$

Now, the force caused by the incident sound field can be calculated:

$$F = 2\pi a L P_i \quad (6.21)$$

Using the electroacoustic reciprocity principle (see Equation 6.2) with F and P_r of Equation 6.19 one gets:

$$\frac{E}{F} = \frac{E}{2\pi a L P_i} = \frac{v P_r}{I P_r} = \frac{P_r}{I} \sqrt{\frac{r}{cf}} \frac{1}{\pi \rho a} \quad (6.22)$$

This leads to the *cylindrical wave reciprocity parameter* [Bob 61]:

$$J_c = \frac{M}{S} = \frac{E/P_i}{P_r/I} = \frac{EI}{P_i P_r} = \frac{2L}{\rho c} \sqrt{\frac{cr}{f}} = \frac{2}{\rho c} (\lambda r)^{1/2} L \quad (6.23)$$

Spherical wave reciprocity parameter J_s

When the transducer is a pulsating sphere the pressure at a large distance r is [Mor 84]:

$$P_r = \frac{f\rho}{2r} Q = \frac{f\rho}{2r} Av \quad (6.24)$$

where the volume velocity Q is the product of the area A and the surface velocity v .

With v expressed with the equation above and the force F , calculated via the product of the pressure incident sound field P_i and the surface A , inserted into the electroacoustic reciprocity principle, this yields:

$$\frac{E}{P_i A} = \frac{P_r}{I} \frac{2r}{\rho f A} \quad (6.25)$$

Now, using again the definition of the reciprocity parameter (see Equation 6.5) one gets the *spherical wave reciprocity parameter* [Uri 83]:

$$J_s = \frac{M}{S} = \frac{E/P_i}{P_r/I} = \frac{2r}{\rho f} = \frac{2}{\rho c} (\lambda r) \quad (6.26)$$

Table 6.1 shows the near and far field conditions with the capable reciprocity parameter and pressure field. The variables λ , f , ρ and $c_s(T)$ represent the wavelength, the frequency, the density of the medium and the speed of sound in the medium, respectively.

In this work the calibration media are water and ice within a temperature range from $+20^\circ\text{C}$ to -25°C . A rough speed of sound estimate for water and ice to verify the near or far field condition is $c_s(T > 0) = 1500 \frac{\text{m}}{\text{s}}$ and $c_s(T < 0) = 3840 \frac{\text{m}}{\text{s}}$, respectively. The length of used transducers are 2 cm (see Figure 6.8) and the frequency range of interest is located between 0 - 100 kHz. The distance between transducer and receiver for calibration measurement is 0.6 m. With all these boundary conditions the far field relation is always fulfilled and therefore the reciprocity parameter for spherical waves J_s and the appropriate $p(r)$ have to be used in further calculations (see Table 6.1).

near field	far field
$a \leq \frac{L^2}{\lambda} = \frac{L^2 f}{c_s(T)}$	$a \geq \frac{L^2}{\lambda} = \frac{L^2 f}{c_s(T)}$
$J_c = \frac{2}{\rho c_s} \sqrt{\lambda r_0} L = \frac{2L}{\rho} \sqrt{\frac{r_0}{c_s f}}$	$J_s = \frac{2}{\rho c_s} \lambda r_0 = \frac{2r_0}{\rho f}$
$p(a) = p_0 \sqrt{\frac{r_0}{a}}$	$p(r) = p_0 \frac{r_0}{a}$

Table 6.1: Near and far field requirements with capable reciprocity parameter and pressure field [Kuc 03] [Uri 83].

Applying the reciprocity parameter for spherical waves J_s to Equation 6.14 the absolute sensitivity M_H of H can be calculated with:

$$M_H = \sqrt{\frac{2a U_1 U_1'}{\rho f U_2 I_{T_2}}} \quad (6.27)$$

The final formula for sensitivity calculation contains the driving current I_x of the transducer used in the second step of the calibration measurement procedure and the density of the calibration medium. Both parameters will be discussed in more detail in the next three subsections.

Determination of I_x via impedance measurement

Since the piezo element is a dielectric with two electrodes it acts mainly as a capacitor with capacitance C_x . This means that below the first resonance the impedance Z_x ² of the piezo element can be expressed by $Z_x \propto \frac{1}{f}$ with the frequency f . Therefore, the complex impedance of the piezo element can be calculated via:

$$Z_x = \frac{U_x}{I_x} = \frac{1}{i\omega C_x} = \frac{1}{i2\pi f C_x} \quad (6.28)$$

Thus the driving current I_x in Equation 6.27 is given by:

$$I_x = |I_x| = \omega C_x U_x = 2\pi f C_x U_x \quad (6.29)$$

By measuring the frequency dependent impedance Z_x (below the first resonance) of the piezo element it is possible to extract within Equation 6.28 the needed C_x for Equation 6.29. To determine Z_x a serial connection of the piezo element and a known capacitor with capacitance C_C close to the

²The index x represents in this thesis the two transducers T_1 and T_2

capacitance of the piezo element is needed [Ant 06]. A schematic drawing of the circuit is shown in Figure 6.3.

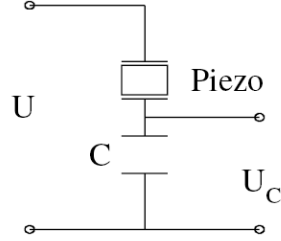


Figure 6.3: Schematic setup for the impedance measurement [Ant 06].

Starting with Ohm's law

$$U = IZ \quad (6.30)$$

using the fact that the total impedance Z in a serial connection is defined via $Z = Z_x + Z_C$ and all currents are equal ($I = I_x = I_C$) we get:

$$U = I_C(Z_x + Z_C) = I_C Z_x + I_C Z_C = I_C Z_x + U_C \quad (6.31)$$

Together with Equation 6.28 adapted for I_C this yields:

$$U = i\omega C_C U_C Z_x + U_C \quad (6.32)$$

Now, the desired Z_x can be calculated:

$$Z_x = \frac{U - U_C}{i\omega C_C U_C} = \frac{U - U_C}{i2\pi f C_C U_C} \quad (6.33)$$

At the beginning of calibration measurements in water (in Wuppertal) a sine wave voltage pulse U at discrete frequencies was used to measure Z_x . Later in the AAL in ice discrete sine waves and a narrow Gaussian shaped voltage pulse is applied to the circuit (thus containing a broad frequency spectrum) and for all input voltages the voltage over the capacitor U_C is analyzed in the frequency domain. In comparison with the mono frequent sine waves the measurements with the Gaussian shaped pulse leads to the complete frequency behavior of the impedance in one measurement and is therefore less time consuming.

The reference capacitor used in Wuppertal has a capacitance of $C_{\text{Wuppertal}} = 470 \text{ pF}$ ($\pm 10\%$)³ and the AAL capacitor has $C_{\text{AAL}} = 2.31 \text{ nF}$ ($\pm 5\%$). An uncertainty of 0.1% concerning the input voltage is assumed.

One example measurement of $|Z_{T_2}|$ versus frequency f at a certain temperature using discrete sine waves and one Gaussian shaped pulse is shown in Figure 6.4 left and right, respectively. Up to the first resonance frequency ($>100 \text{ kHz}$) the expected capacitor like $\frac{1}{f}$ dependence is visible. In frequency range of interest up to 100 kHz the constant slope can be fitted (red line) and as shown in Equation 6.28 the slope of the graph is equal $\frac{1}{2\pi C_x}$. Both measurements agree as expected within their uncertainties.

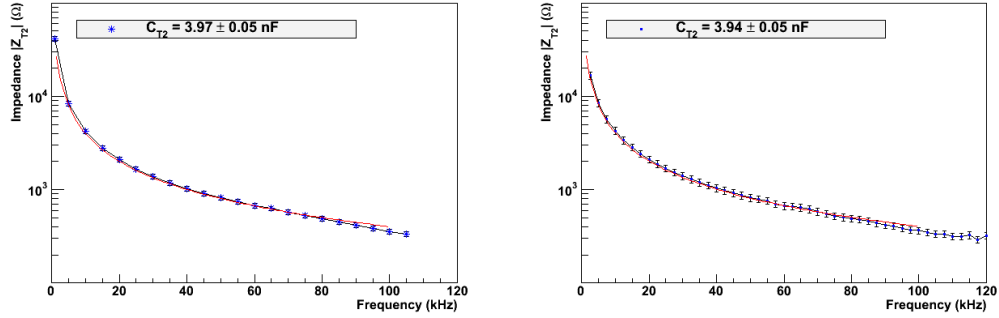


Figure 6.4: Impedance measurement for transducer T_2 at one certain temperature to calculate the piezo element capacitance C_{T_2} via the fitted slope (red). Left side plot corresponds to input voltages of discrete sine waves and right side plot to one narrow Gaussian shaped pulse.

The capacitance of both transducers need to be measured before each calibration measurement. With Equation 6.29 the absolute sensitivity given in Equation 6.27 becomes:

$$M_H = \sqrt{\frac{a}{\rho f^2} \frac{U_1 U'_1}{\pi U_2 U_{T_2} C_{T_2}}} \quad (6.34)$$

³<http://de.farnell.com/murata/debb33f471kc3b/kondensator-470pf-3000v/dp/9527176> (May 3rd, 2010)

Determination of I_x via measurements with coil

Another possibility for determination of I_x , adapted from [Buo pr], will be described now.

With this contact free measurement the transducer driving current can be measured during the calibration measurements with a coil. A schematic setup is shown on the left of Figure 6.5. In comparison with the determination of I_x only one measurement, the frequency dependent resistance of the coil, needs to be done. The result for the coil, used in this thesis, is pictured on the right side of Figure 6.5. With the frequency dependent resistance, the voltage $U(\omega)$ measured at the coil can be converted into the needed current.

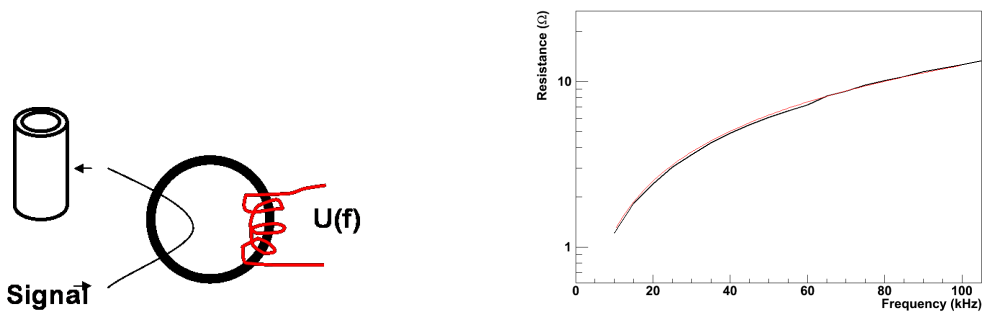


Figure 6.5: Schematic setup with coil for contact free transducer driving current measurement on the left and frequency dependent resistance on the right (data in black with fit in red).

For example, the driving current from T_1 received via impedance measurement (see Equation 6.29) and via coil measurement is shown in Figure 6.6. The result received via coil measurement shows an equal or lower driving current in comparison with the current received via impedance measurement.

Consequently, when using the coil, the lower current would lead to a slightly higher sensitivity, because the driving current is located in the denominator of the sensitivity equation (see Equation 6.27).

The answer to the question as to which technique for driving current measurements should be preferred when doing reciprocity calibration will be given in Section 8.4.

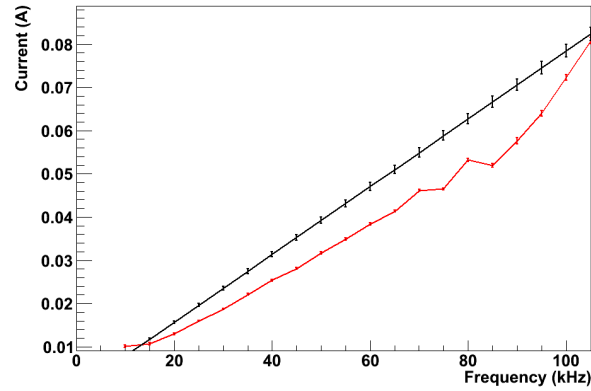


Figure 6.6: T_1 driving current comparison; black curve received via impedance measurement and red via coil measurement.

Density vs. temperature of H_2O

The density of the medium ρ used in Equation 6.27 and 6.34 corresponds in this thesis to the density of water and ice. Especially the density of ice is rarely represented in literature and the used density of H_2O is shown in Figure 6.7. The data points are colored in blue and the required intermediate values for sensitivity calculations are received via spline fit (red).

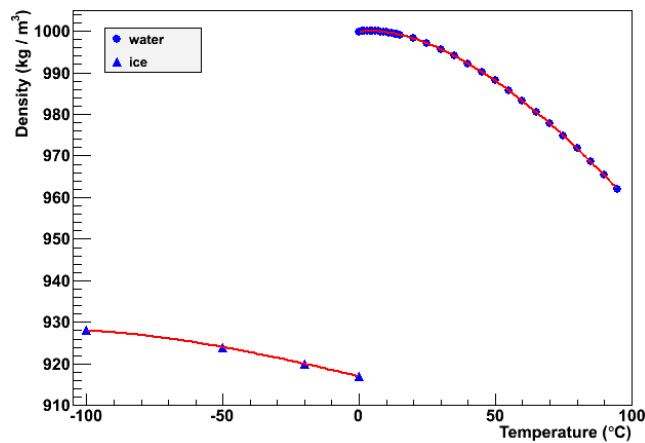


Figure 6.7: Density vs. temperature of H_2O ; data points are colored in blue with spline fit in red [Raz 77] [VDI 06].

Reciprocity calibration setup

The used transducers T_1 and T_2 consist of the same piezo element type and they are coated with hard polyurethane for water and ice protection. Transducer T_2 can be seen in Figure 6.8.

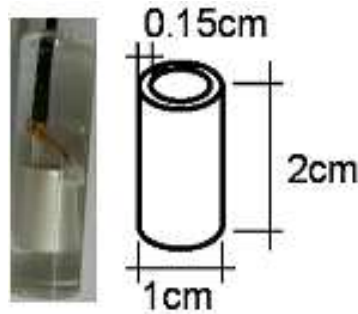


Figure 6.8: Transducer T_2 coated with polyurethane on the left and a schematic drawing of the used piezo element on the right side.

As mentioned above, the two devices T_1 and T_2 used in this thesis are both transducers instead of one transducer and one transmitter which would be sufficient to apply the described reciprocity method. The fact that both are transducers offers the possibility to start the two step calibration measurement with T_1 or T_2 and one should obtain the same sensitivity result of H at the end. To distinguish between the two possibilities each configuration type is named after the transducer used in the second step. In the formalism above transducer T_2 is used in the second step and therefore this configuration is called *type T_2* configuration. Both configurations are visualized in Figure 6.9 and 6.10

As mentioned for the comparison method in water it is essential to exchange the receivers to prevent the influence of azimuthal uncertainties. This adapted to the reciprocity method in water leads to the setup shown in Figure 6.9. Using the reciprocity method in ice, it is not possible to exchange the transducers and the hydrophone quickly, therefore the devices need to be mounted in an equilateral triangle and the azimuthal sending/receiving variations need to be taken into account.

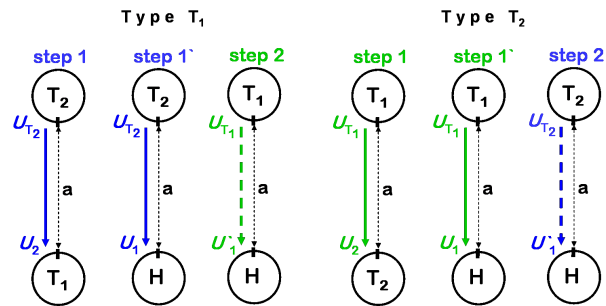


Figure 6.9: Schematic setup for reciprocity calibration in water (top view).

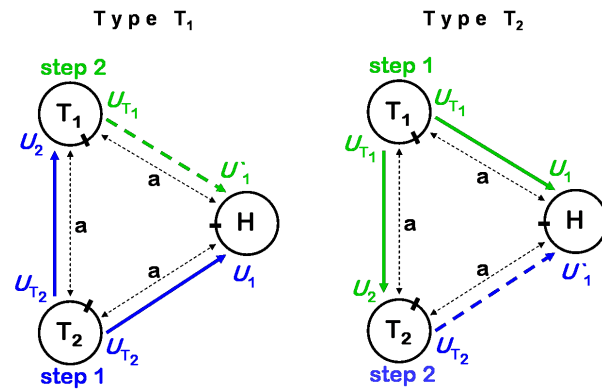


Figure 6.10: Schematic setup for reciprocity calibration in ice (top view).

6.3 Pre-calibrated hydrophone Sontortech SQ03

A calibrated hydrophone, used in this thesis to check the quality of the calibration setup and to estimate the uncertainties in the reciprocity calibration method, is *Sontortech SQ03*⁴ (see Figure 6.11). This hydrophone was bought in fall 2003 by DESY Zeuthen and the calibration data provided by the company states a frequency independent sensitivity of -163.3 ± 1.0 dB re $1 \text{ V} / \mu\text{Pa}$ [Fis 06]. The hydrophone has a preamplifier with a gain of 40 dB (amplification factor: 100) in amplitude.



Figure 6.11: Absolutely calibrated hydrophone Sontortech SQ03. The acoustic sensitive area is the black part on the right side.

The SQ03 has been calibrated frequency dependent in Rome by the Istituto di Acustica e Sensoristica “Orso Mario Corbin” in summer 2004. The laboratory is accredited by SIT as Calibration Centre for hydrophones in compliance with the International Standard ISO/IEC 17025:2005. The calibration was done in water at three different azimuth angles using the comparison method. Due to the method a systematic uncertainty of ± 1 dB has to be taken into account. The result is shown in Figure 6.12. All three azimuth angle measurements agree within the systematic uncertainty.

To use the SQ03 as trustable absolute calibrated reference device to cross check the setup in Wuppertal in 2010 a re-calibration of the SQ03 was needed to exclude changes in sensitivity with time or damages of the SQ03. Again the institution in Rome was used for the re-calibration measurements, but this time the reciprocity method was chosen. All settings used for the calibration will be described below and they base on [Buo pr].

Two passive transducers *ITC 1032* and *TC 4033* were used and in order to avoid the influences of azimuthal variations always the same azimuthal angle of each sensor was used for every measurement. Two sensors were used at a time facing each other at the previously chosen angle.

⁴<http://www.sontortech.ca>

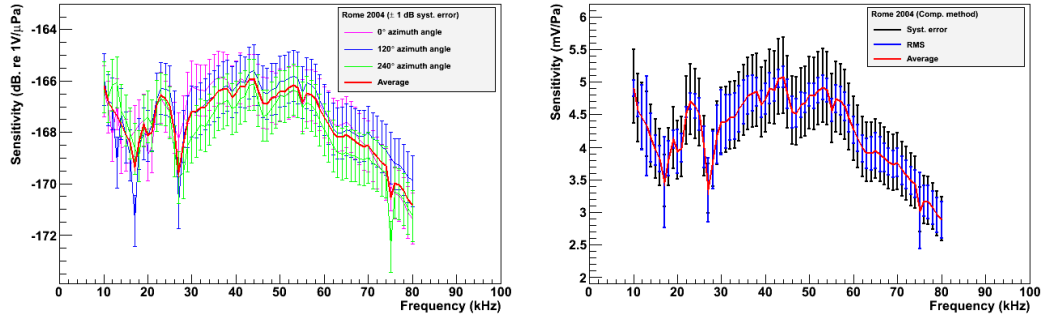


Figure 6.12: Measured sensitivity of SQ03 in 2004 for three different azimuth angles with ± 1 dB systematical uncertainty and the sensitivity average (red) is shown on the left side. On the right side the average sensitivity (red) with systematical (black) and statistical (blue) uncertainty in a linear scale is pictured.

The nominal distance between the sensors was 1 m and the dimensions of the water cuboid were 4 m x 6 m x 5.5 m (length x width x depth). The transmitted signals were sine wave bursts at the desired frequencies. The length of the burst was adjusted in a way that the receiving of the primary signal was finished before the reflections arrived at the receiver. The current needed for the sensitivity calculation was measured contact free during the calibration measurement with the help of a coil. If one of the passive transducer acts as receiver, it was connected to an amplifier and the gain factor for each frequency was adjusted before the calibration measurement to fit in the ADC range properly. The received signal was averaged and band pass filtered to exclude frequencies far outside the range of interest. For the final sensitivity calculation a time window containing stable sine wave cycles (excluding the beginning and the end of the received signal) was used.

The sensitivity of SQ03 received via the reciprocity method for one certain azimuth angle is shown in comparison with the previous calibration result from 2004 received via the comparison method, see Figure 6.13. For the reciprocity method a systematic uncertainty from ± 0.6 dB has to be taken into account. From 15 - 80 kHz both sensitivities agree within their error bars. This is visible when calculating the ratio between sensitivities from SQ03 calibrations in Rome 2004 and 2010, shown in Figure 6.14. A fitted constant line leads to $c = 1.0$ ($\chi^2/\text{NDF} = 0.66$) and shows the expected agreement.

The SQ03 sensitivity has not changed within the last years and it can be used as a trustable calibrated hydrophone for cross checks within the water setups for sensor calibration in this thesis.

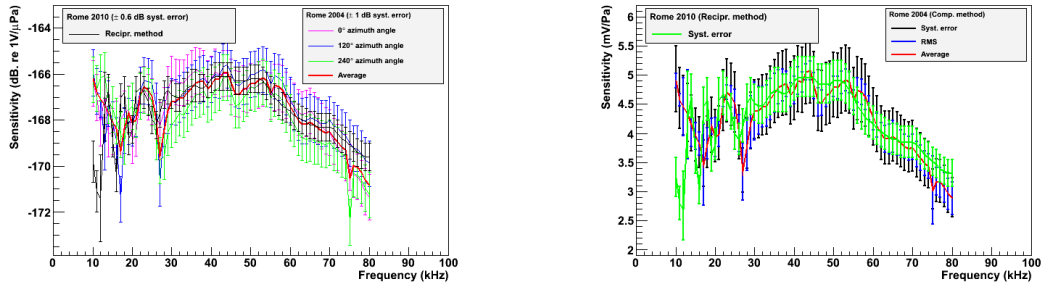


Figure 6.13: Comparison between the sensitivity measurements from 2004 received via the comparison method and the sensitivity measurement from 2010 received via the reciprocity method. Above 15 kHz both sensitivity curves agree within their error bars.

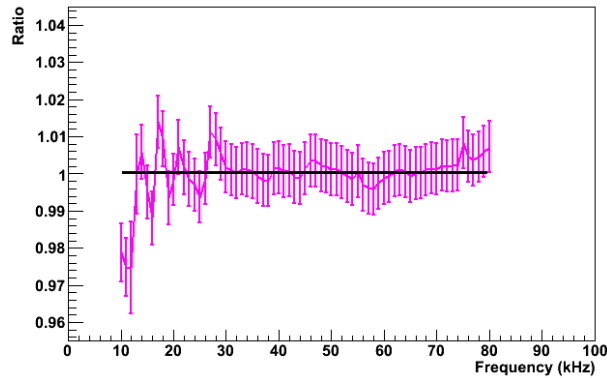


Figure 6.14: Ratio between the sensitivities from SQ03 calibrations in Rome 2004 and 2010. A fitted constant line with $c = 1.0$ ($\chi^2/\text{NDF} = 0.66$) shows the expected agreement between the two calibration measurements.

Chapter 7

Laboratory facilities

The unique possibility to deploy two additional types of sensors (advanced SPATS sensors and alternative HADES sensors) with string D required for the HADES sensors a quick production and testing to meet the time schedule until deployment in the South Pole ice. Two HADES sensors of each type (HADES A (1,2) and HADES B (1,2), see Section 5.2) were produced in addition to the two for deployment to study their properties and to estimate the uncertainties; e. g. sensor to sensor sensitivity variation and angular sensitivity dependence.

To study the HADES sensors a water tank in Wuppertal, called *Wuppertal Water Tank Test Facility* (WWTF), was used. In contrast to ice, here one is able to rotate, change or move the sensors quickly. For ice calibration measurements the Aachen Acoustic Laboratory (AAL) provided clear ice. Both laboratory facilities will be described hereafter .

7.1 Wuppertal Water Tank Test Facility

For all acoustical laboratory measurements it is important to distinguish between the primary signal and reflections. This can be guaranteed via a large (water) volume.

The water tank consists of five concrete rings¹ with an inner diameter of 2.5 m. Four shaft rings with an inner height of 0.5 m and a weight of 1180 kg each are stacked on a bottom ring with an inner height of 0.35 m and a weight of 2150 kg. This yields a total inner height of 2.35 m and an effective

¹<http://www.mall.info/>

water volume of $\approx 10 \text{ m}^3$. The tank is laid-out with PVC foil² (thickness: 0.8 mm) in form of an open cylinder (bottom part was welded to the foil by the company). To protect the foil against the roughness of the concrete, fleece (density: 300 g/m^2) is used to get a plane inner surface of the tank.

A walkable wooden platform with guard rail and a 1 m^2 opening for device installation is located at the top. To provide always the same water quality algicide is used and a pump in combination with a sand filter (ISKK 3005/4W³) cleans the water for 3 h per day. The water quality is tested regularly for its by pH-value. A picture of the water tank with platform, installation opening and pump with sand filter (blue) is shown in Figure 7.1.

To install sensors inside the tank at a desired position for angular sensitivity measurements or calibration measurements for example one mounting per sensor, consisting of three stainless steel ropes (diameter 1 mm) merging at a weight, is used. With the help of the weight the sensor is fixed between the ropes. The other end of the ropes is connected to a turnable aluminum disc at the top (see Figure 7.2 on the left) and the sensor follows the rotational direction when turning the aluminum disc.

For data taking a LabView based NI-Data Acquisition (DAQ) (NI USB-6251 BNC⁴) has been used; 8 differential BNC analog inputs (16-bit), 1.25 MS/s single-channel (1 MS/s aggregate). The DAQ is connected to a PC via USB connection.

When installing acoustic sensors in water a certain amount of time is necessary until the measurement can start. The sensor needs to be in thermal equilibrium with the surrounding medium, and in water one needs to wait until all (micro) air bubbles, accumulated at the sensor surface directly after installation, have vanished. Air bubbles can decrease the received signal strength by more than a factor of two [Gra pr]. This effect has been measured using transducer T_2 installed in the water tank a long time before the installation of HADES B (2) to ensure that T_2 was in thermal equilibrium and no more bubbles were present at the resin surface of T_2 . Directly after the installation of HADES B (2) in a horizontal distance of 60 cm to T_2 one single 20 kHz sine wave cycle was sent every three minutes, and the received reflection free maximum peak to peak amplitude versus time was recorded.

²<http://www.folienvertrieb-drewke.de>

³<http://www.poolpowershop.de/Anleitungen/minisandfilteranlage.pdf>

⁴<http://sine.ni.com/nips/cds/view/p/lang/en/nid/203865>



Figure 7.1: Wuppertal Water Tank Test Facility with walkable platform, installation opening and pump with sand filter (blue).

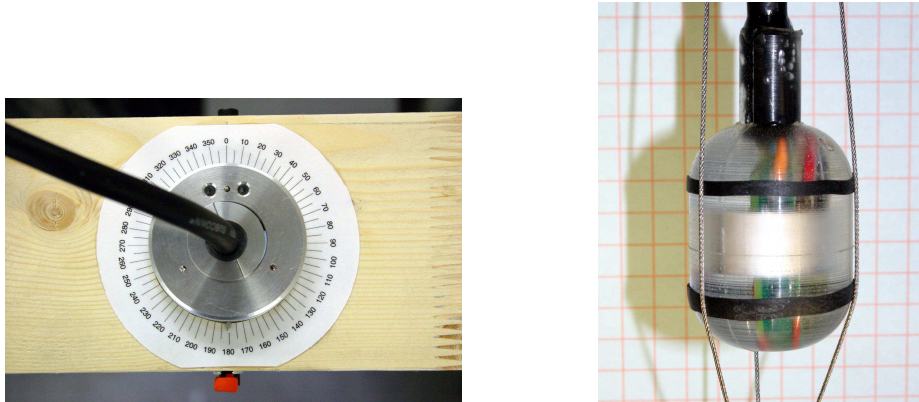


Figure 7.2: Top view of one sensor mounting with angular scale (left side) and HADES sensor with rubber rings (black) mounted between three stainless steel ropes (right side) [Har pr].

In Figure 7.3 the result is shown and an increase in maximum peak to peak amplitude with time is clearly visible. To force the air bubbles to disappear, the sensor surface can be covered with liquid soap (which destroys the surface tension of the water) directly prior to installation in the water [Buo pr]. The measurement described above was repeated, but the surface of sensor HADES B (2) was covered in advance with liquid soap. The result is shown in Figure 7.4.

On the left side of Figure 7.3 and 7.4 24 h of data taking are shown, and in comparison with the measurement without liquid soap a much faster peak to peak amplitude increase is visible. The slight difference in final maximum peak to peak amplitude between the two measurements was caused by an accidental misplacement during the second measurement.

For quantification of this effect an exponential function fit $f(x) = a \cdot [1 - \exp(-c \cdot x)] + b$ is applied to the first six hours of each dataset to receive the time constant c . A time constant $c = 0.81 \pm 0.03$ 1/h, related to the measurement without the use of soap (Figure 7.3; right side), in comparison with the time constant $c_{\text{soap}} = 2.49 \pm 0.41$ 1/h, received via the sensor covered with soap (Figure 7.4; right side), underline nicely the quick reduction of air bubbles on the sensor surface with the help of liquid soap.

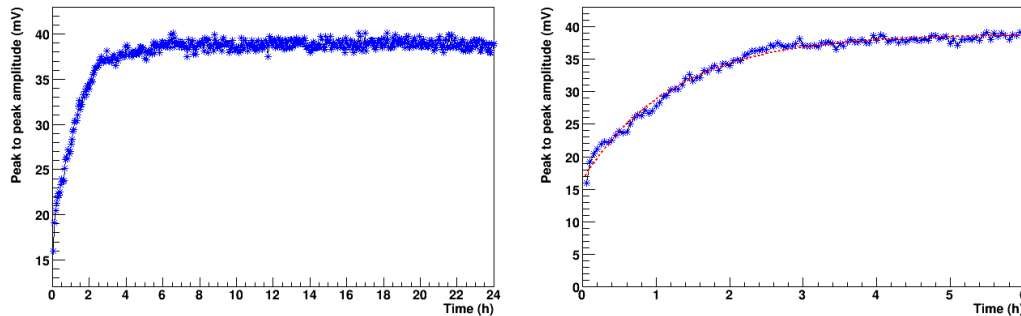


Figure 7.3: Measurement with HADES B (2) (received peak to peak amplitude versus time) started directly after installation inside the water tank. Increase in amplitude due to (micro) air bubbles accumulated at the sensor surface directly after installation which vanish over time. All data is shown on the left side, and a zoom into the first 6 h with fitted exponential function (red dashed line) is pictured at the right side.

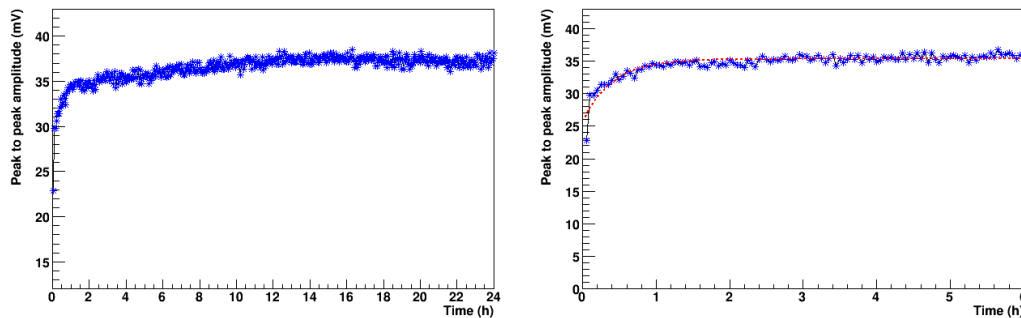


Figure 7.4: Measurement with HADES B (2) (received peak to peak amplitude versus time) started directly after installation inside the water tank, but the surface of HADES B (2) was covered with liquid soap prior to lowering it into the water. Increase in amplitude is much faster in comparison with the setup without liquid soap (see Figure 7.3). All data is shown on the left side, and a zoom into the first 6 h with fitted exponential function (red dashed line) is pictured on the right side.

7.2 Aachen Acoustic Laboratory (AAL)

The main part of AAL is an IceTop tank [Kis 10] located in a cooling container.

The cooling container,⁵ (usually used for food) with the inner dimensions of 545 cm × 226 cm × 211 cm (length × width × height) provides low air temperatures down to -25°C. The desired temperature is adjustable within 0.1°C. A cable feedthrough for power and data taking is installed in the upper part of one side wall of the container.

The IceTop tank is a leftover of the IceTop air shower experiment. It has a diameter of 1.85 m and a height of 1 m. Together with a thermal isolation coating at the side, the so called *Freeze Control Unit* (FCU) allows for the production of clear ice within a top down freezing process. The schematic view of the IceTop tank to present the dimensions is shown in Figure 7.6. The tank located inside the cooling container is presented in Figure 7.5. A membrane as part of the FCU helps to degas the water and prevent the formation of bubbles on the growing surface and the sensors. The water is circulated along a membrane which is permeable to air (nitrogen / oxygen) molecules (not to water molecules) and one side of the membrane is slightly evacuated. The overpressure induced by the expansion in the phase transition from water to ice can be regulated by an overflow output at the bottom. Starting with 0°C water inside the IceTop tank the freezing process with a crystal clear block of ice at the end takes about 60 days. More details about the FCU and the freezing process can be found in [Vog 07].

For calibration measurement it is essential to distinguish between the primary signal and the reflections or at least the moment when the first reflection disturbs the fading out of the primary signal in the piezo pulse. Therefore, the speed of sound inside the media needs to be known. For in ice calibration in AAL the speed of sound of this special type of clear ice has been measured in [Vog 07] (see Figure 7.7). A parametrization of the measurement result was received via a line fit. The speed of sound (in m/sec) for longitudinal (pressure) waves in this clear ice is:

$$v_{\text{ice}}(T) = -2.812 (\pm 0.012) \frac{\text{m}}{\text{s}} \cdot \frac{T}{\text{°C}} + 3837.9 (\pm 5.3) \frac{\text{m}}{\text{s}} \quad (7.1)$$

⁵<http://rainbow-containers.de>



Figure 7.5: IceTop tank with the FCU at the front and with the white thermal isolation coating inside the cooling container [Vog 07].

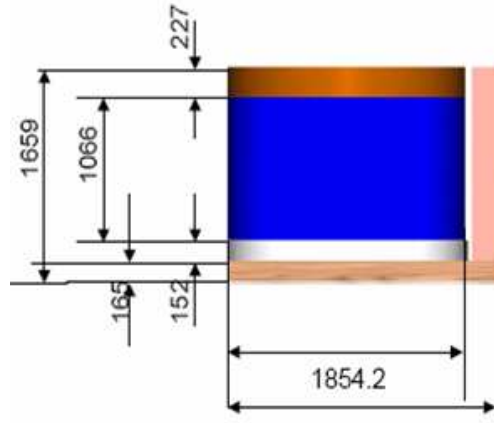


Figure 7.6: Schematic drawing of the IceTop tank (side view). The FCU is located on the right and all values are in mm [Lai pr].

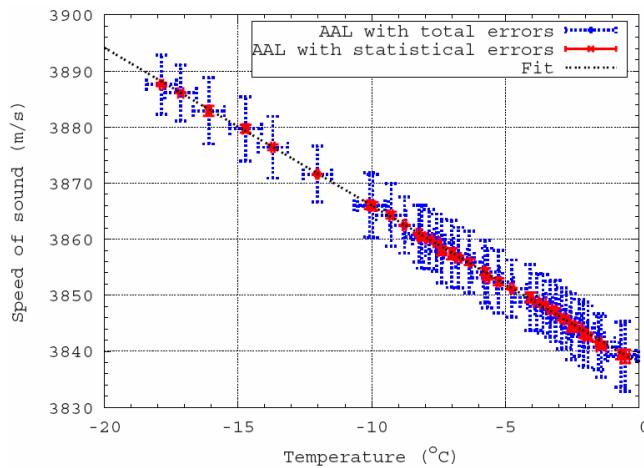


Figure 7.7: Speed of sound for pressure waves in clear ice produced in AAL. The line fit (dotted black line) to the values is done using statistical errors (red) only [Vog 08].

Chapter 8

HADES sensor properties

This Chapter contains directional and sensitivity measurement results and leads to the understanding of HADES sensor properties.

At first the directional sensitivity of the sensor will be studied in detail followed by the determination of the sensor self-noise and the investigation of a possible sensitivity change with temperature. At the end the calibration results for water and ice will be discussed.

8.1 Directional sensitivity

The measurements have been done in the water tank in Wuppertal. A transmitter and sensor (with a distance of 0.6 m from each other) and only the primary signal without the influence of reflections is used for the analysis. Therefore the devices are located inside the water tank in a way that the distances to the bottom, inner walls and water surface are maximized. A narrow signal pulse (broad frequency spectrum) is emitted by the transmitter and 30 single pulses per angle setting (10° step size) are recorded. The 30 pulses are averaged in time domain and the Fourier transform of every single pulse was calculated for the determination of the averaged spectrum in frequency domain. With the average in time domain the peak to peak value and with the average in frequency domain $\bar{\mathcal{F}}(f)$ the energy value in frequency range from 10-50 kHz for every angle setting x ($E_x = \int_{10\text{ kHz}}^{50\text{ kHz}} |\bar{\mathcal{F}}(f)|^2 df$) are used for further analysis. The mean over all angles for the peak to peak values \bar{V}_{pp} and the mean energy value \bar{E} is calculated. The relative deviation of each particular mean ($\frac{E_x - \bar{E}}{\bar{E}}, \frac{V_x - \bar{V}}{\bar{V}}$) versus angle is discussed below.

To explore the influence of the “egg shaped” resin coating, piezo electric elements without the amplifier are coated in different orientations and their angular sensitivity was measured.

Starting with the normal arrangement of piezo electric element and coating as used for the HADES sensors (but without amplifier) the azimuth measurement (see Figure 8.1) yields a more less uniform azimuthal sensitivity as expected. As visible in Figure 8.1 the sensitivity around zero is increased and around π decreased. This deviation of the mean could be related to the non-centered piezo ceramic element inside the resin coating but more studies have been done with the next measurement.

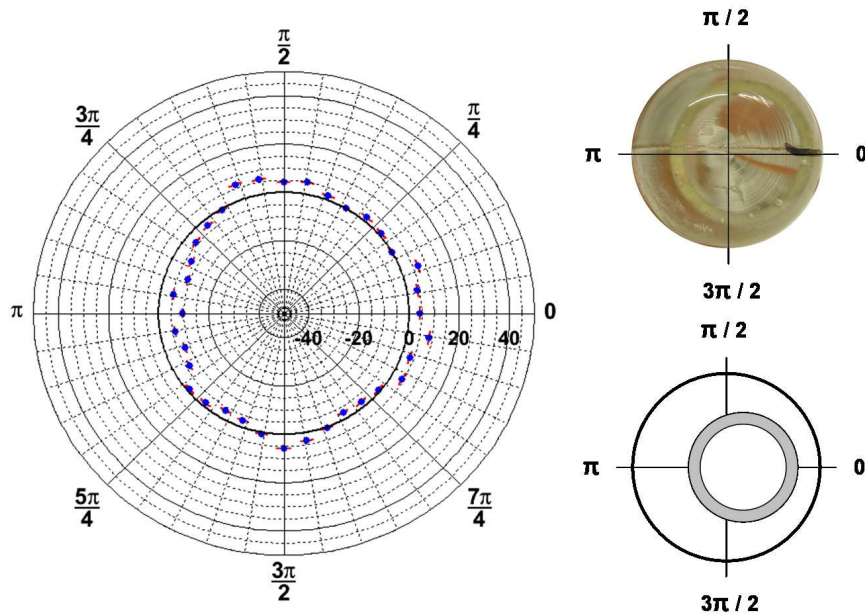


Figure 8.1: Relative azimuth sensitivity of piezo electric element coated without amplifier (type I). Deviation of the energy mean (10-50 kHz) in % versus azimuth angle is shown on the left side. In the right upper corner a bottom view of the device is pictured to indicate that the piezo electric element is not centered and in order to clarify this a schematic drawing of this is shown in the bottom right.

In Figure 8.2 the relative azimuth sensitivity of the piezo electric element has been measured with another orientation of the resin in comparison with Figure 8.1. In Figure 8.2 the shape of the surrounded resin can be identified and it is visible that the thickness of the resin coating could be responsible for a decreased sensitivity.

The peak to peak amplitude values versus angle have been normalized to the global maximum of this measurement. Due to the shape and the orientation of the piezo element a 0° to 180° symmetry is expected and therefore two curves from 0° to 180° are visible in the right upper corner (of Figure 8.2). As visible the piezo electric element is not perfectly aligned (no 0° to 180° symmetry) and the maximum sensitivity is not present at $\pi/2$ and $3\pi/2$ on the left side of Figure 8.2.

In Figure 8.3 the presented sensitivity deviations in the 10-50 kHz band are split up and a clear frequency dependent angular sensitivity is visible.

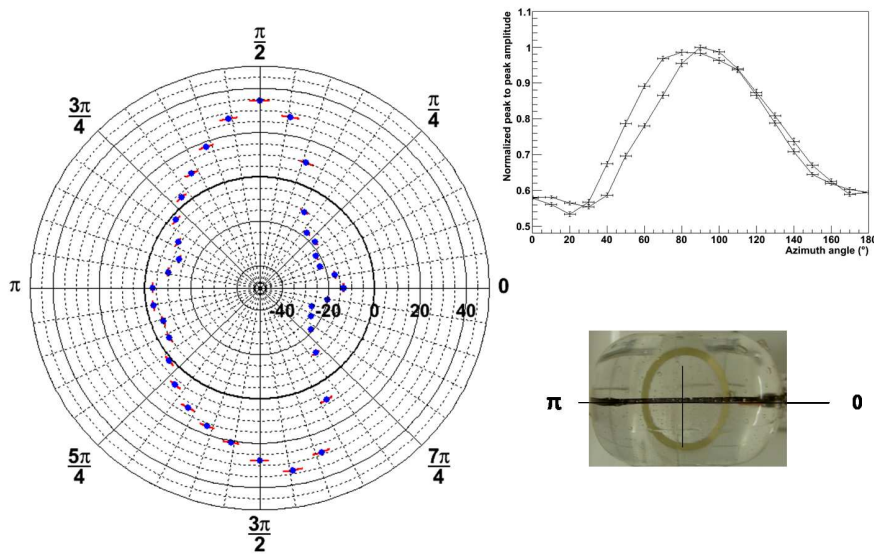


Figure 8.2: Relative azimuth sensitivity of piezo electric element coated without amplifier (type II). Deviation of the energy mean (10-50 kHz) in % versus azimuth angle is shown on the left side. The normalized peak to peak amplitude versus angle in the right upper part indicates that the piezo electric element is not perfectly aligned (no 0° to 180° symmetry). The position of the device during measurement is shown at the bottom right.

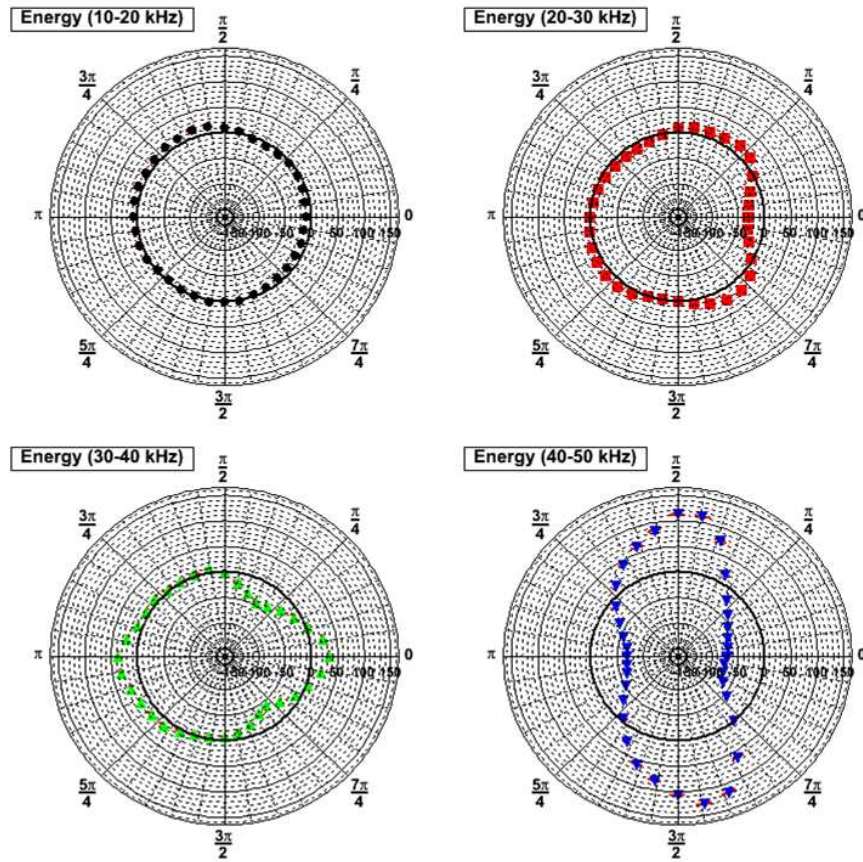


Figure 8.3: Relative azimuth sensitivity of piezo electric element coated without amplifier (type II). Deviation of the the energy mean in % versus azimuth angle for different frequency bands.

The relative zenith sensitivity (type I) of the piezo electric element is shown in Figure 8.4. At $\pi/2$ and $3\pi/2$ the signal is received via the outer walls of the ring shaped piezo element, and therefore the maximum sensitivity is expected. The maximum is slightly shifted, because the piezo ceramic element is not perfectly aligned, shown with the normalized peak to peak amplitude versus angle in the upper right corner of Figure 8.4. Surprising is the fact that a certain sensitivity is present at 0 and π , though the signal is received via the open side of the ring shaped piezo.

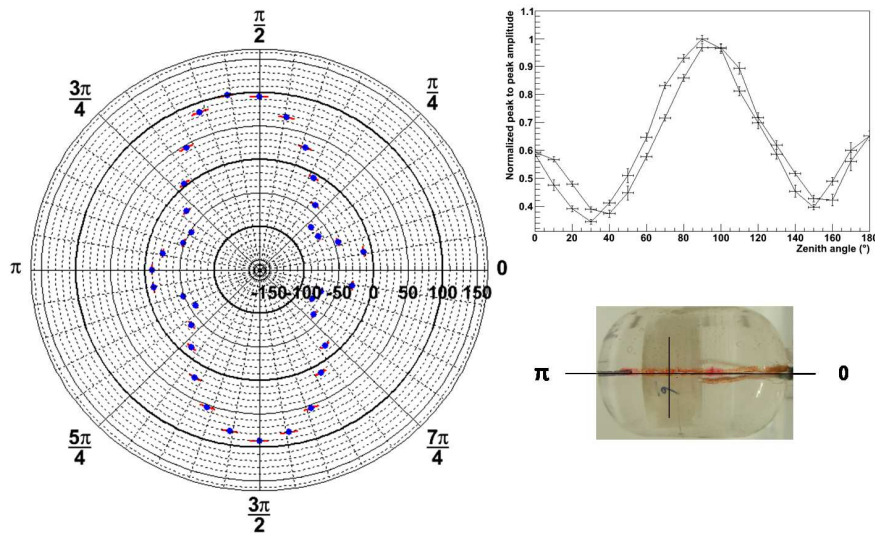


Figure 8.4: Relative zenith sensitivity of piezo electric element coated without amplifier (type I). Deviation of the energy mean (10- 50 kHz) in % versus zenith angle is shown on the left side. The normalized peak to peak amplitude versus angle in the right upper part indicates that the piezo electric element is not perfectly aligned. The position of the device during measurement is shown at the bottom right.

The last possible configuration is shown in Figure 8.5. The piezo ceramic element is positioned vertically and surrounded by more or less the same amount of resin in the transmitter/sensor plane. It is nicely visible that the maximum sensitivity is present when receiving with the walls of the ring shaped piezo ceramic element ($\pi/2$ and $3\pi/2$), the minimum sensitivities are given at the edges of the piezo and a medium sensitivity occurs at the open sides of the ring.

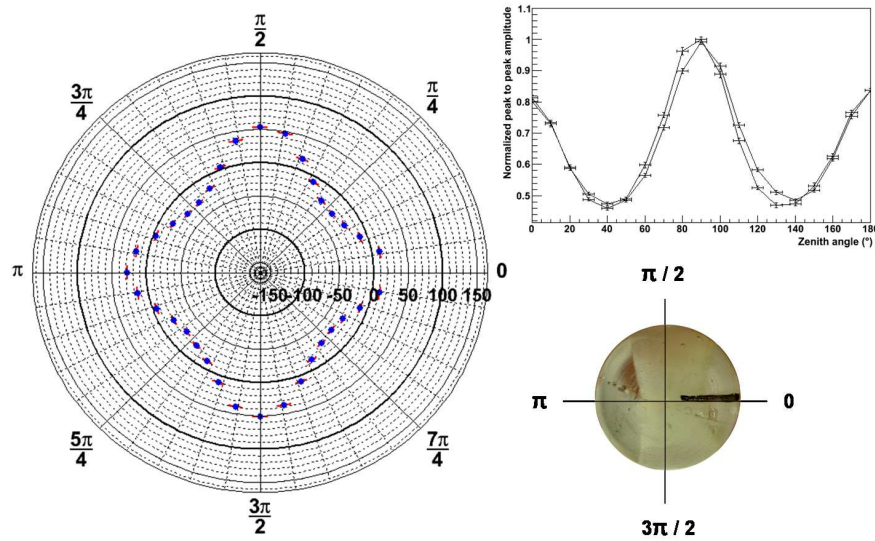


Figure 8.5: Relative zenith sensitivity of piezo electric element coated without amplifier (type II). Deviation of the energy mean (10- 50 kHz) in % versus zenith angle is shown on the left side. The normalized peak to peak amplitude versus angle in the right upper part indicates that the piezo electric element is well aligned. The position of the device during measurement is shown at the bottom right (bottom view).

8.1.1 Azimuthal sensitivity of HADES

The azimuth sensitivity variation for all four HADES sensors is shown in Figure 8.6. In comparison with the result in Figure 8.1, where a sensor without the amplifier board was used, a higher deviation of the mean of up to 40 % is visible. Possible reasons could be inner reflections and diffraction due to the amplifier board. In addition, the amplifier board is soldered with one side to the inner wall of the piezo electric element, which could cause damping of the piezo vibrations around this area. As visible in Figure 8.6 the relative sensitivity deviations could be related to the position of the piezo electric element within the resin coating as dominant effect.

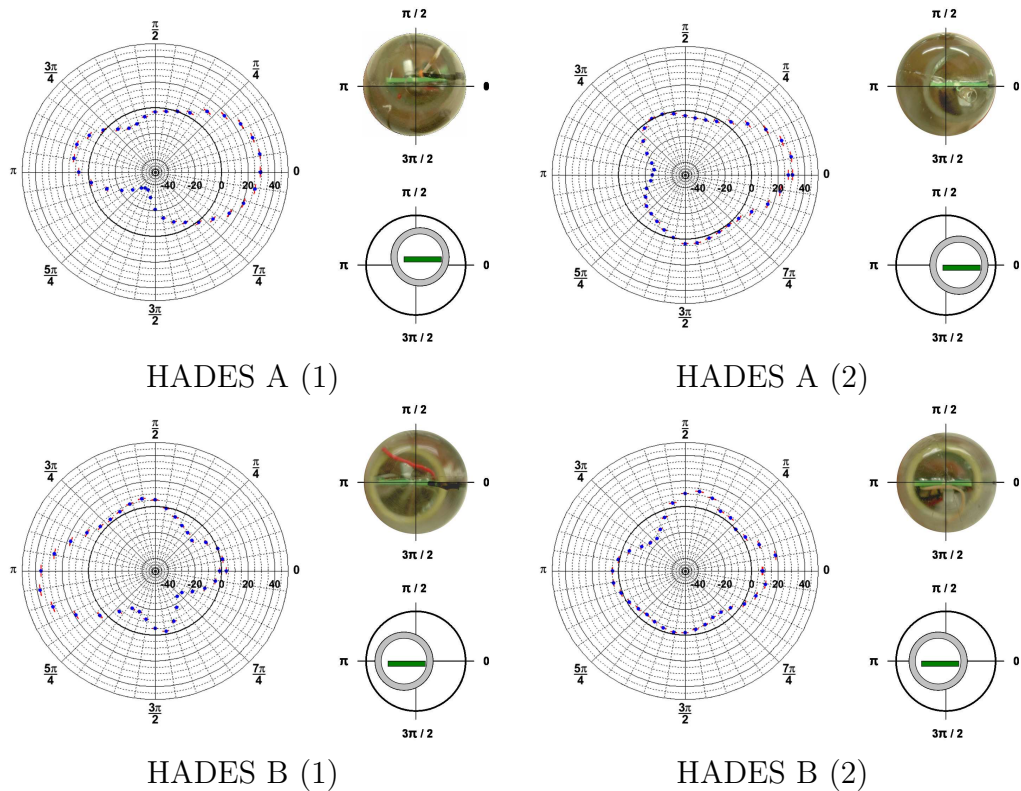


Figure 8.6: Relative azimuth sensitivity of HADES sensors. Deviation of the energy mean (10-50 kHz) in % versus azimuth angle is shown on the left side of each panel. In the right upper corner a bottom view of the sensor is pictured to indicate that the piezo electric element is not centered and to clarify this a schematic drawing of this is shown at the bottom right. The positive/negative deviation of the mean can be related to the shift of the piezo ceramic element inside the resin coating.

8.1.2 Zenith sensitivity of HADES

For the zenith sensitivity measurements in the water tank an azimuth angle setting for each sensor was chosen in a way that the same thickness of resin was present in the horizontal sensor/transmitter plain. This yields the same maximum sensitivity (same deviation of the mean in %) at $\pi/2$ and $3\pi/2$ if the piezo element was not tilted (see Figure 8.8).

The power/readout cable is present around 0° zenith angle and causes shadowing effects. As shown in Figure 5.7 and 5.8 the deployed HADES sensor is connected to a (modified) SPATS sensor housing which dominates the shadowing effects in this zenith angle region. An estimation of the shadowed zenith angle region is shown in Figure 8.7, and for all zenith angle sensitivity measurements the zenith angle region around $\pm 30^\circ$ is excluded.

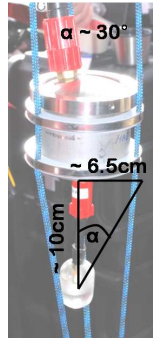


Figure 8.7: Schematic drawing of shadowing effect in zenith angle due to sensor housing.

The zenith sensitivity results for the four HADES sensors are visible in Figure 8.8, and they show a deviation of the mean of up to 100%. A comparison with Figure 8.4 (zenith sensitivity measurements without amplifier) shows a similar shape and also an variation of up to 100% due to the shape of the surrounding resin but inner reflections and diffraction due to the amplifier board cannot be excluded. As described above the azimuth angle during these measurements was chosen in such a way that the same thickness of resin was present in the horizontal sensor/transmitter plain, and the orientation of the amplifier board towards the transmitter was not taken into account.

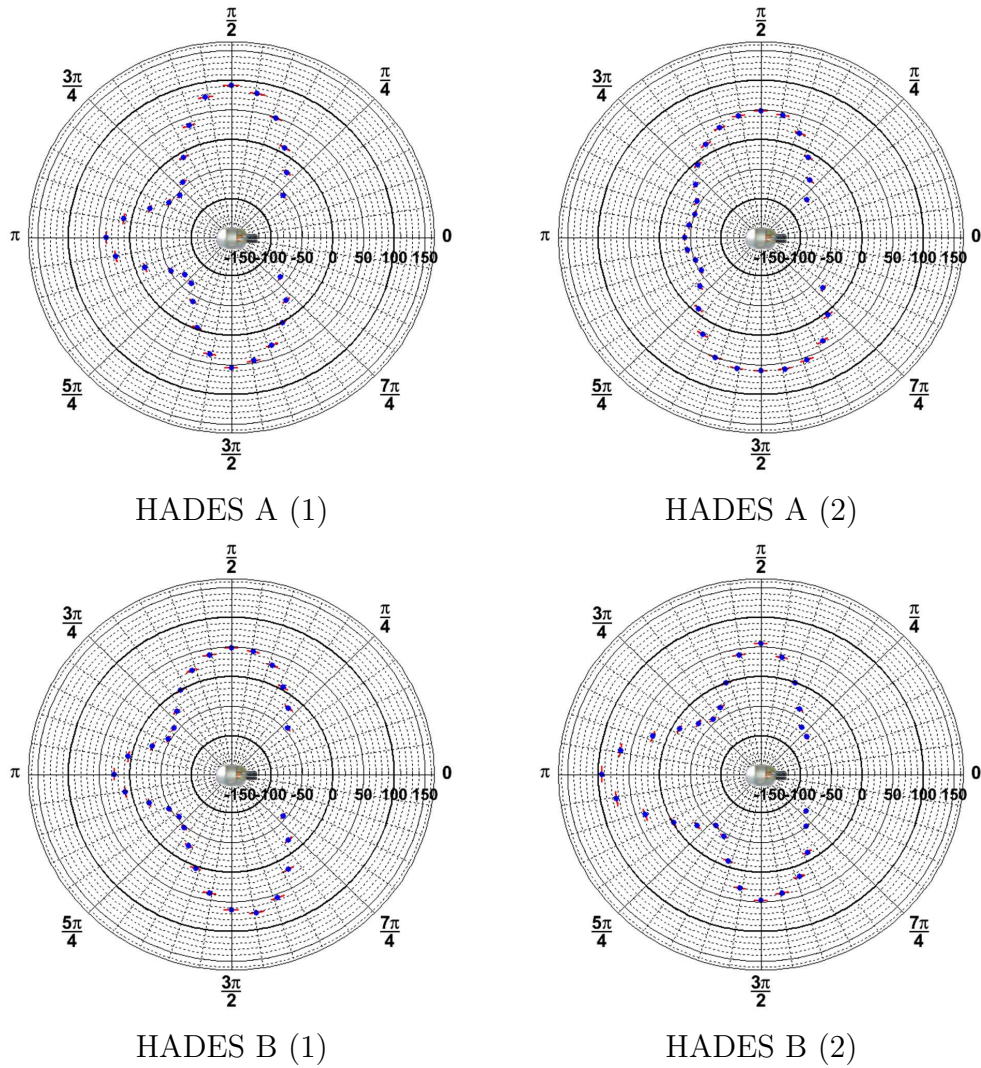


Figure 8.8: Relative zenith sensitivity of HADES sensors. Deviation of the energy mean (10-50 kHz) in % versus zenith angle. The readout cable is located on the right hand side (0°)

Confirmation of zenith sensitivity with transmitter data

The relative zenith sensitivity of HADES measured in laboratory will be parameterized at first for a comparison with measured transmitter data at South Pole.

The peak to peak amplitude versus zenith angle per sensor measured in laboratory is normalized and assumed to be symmetrical from 0° - 180° and 180° - 360° . Therefore two curves per sensor are shown in Figure 8.9 (colored markers) from 0° - 180° . The shown data points only include the RMS uncertainty from the averaging and no systematical uncertainties. A polynomial fit (black curve) is applied to all data and the degree of the polynomial is chosen via the minimum χ^2 / NDF value (see table in Figure 8.9). The polynomial fit is applied from $]30^\circ; 180^\circ]$ due to the described shadowing effect of the sensor housing. The polynomial fit can be parameterized via Equation 8.1.

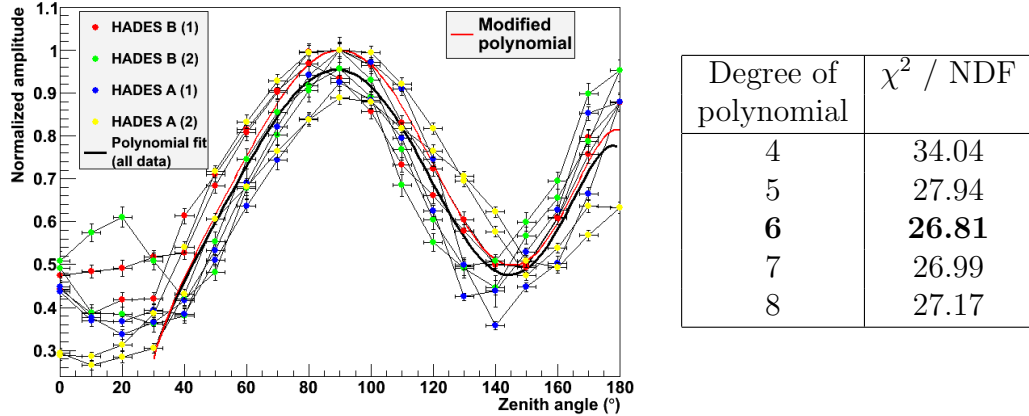


Figure 8.9: Normalized zenith sensitivity (peak to peak amplitude) with polynomial fit (6th degree; fit range: $]30^\circ; 180^\circ]$; black curve) to all data (left side) and χ^2 / NDF values for different degrees of this polynomial (right side). The manually modified polynomial is shown in red.

$$\begin{aligned}
 p(x) = & -1.86347 + 0.168368 (x/^\circ) - 5.37485 \cdot 10^{-3} (x/^\circ)^2 & (8.1) \\
 & + 9.46097 \cdot 10^{-5} (x/^\circ)^3 - 8.74958 \cdot 10^{-7} (x/^\circ)^4 \\
 & + 3.93477 \cdot 10^{-9} (x/^\circ)^5 - 6.77091 \cdot 10^{-12} (x/^\circ)^6 &]30^\circ; 180^\circ]
 \end{aligned}$$

For an zenith sensitivity measurement with a piezo ceramic element (used for HADES) positioned absolute horizontally towards the transmitter, it is expected to receive the maximum sensitivity at 90° and 270° . The maximum value (angle / amplitude) of Equation 8.1 is used to shift and scale this equation to fulfill the mentioned assumption and the result is shown in Equation 8.2. This Equation 8.2 is used as the final zenith sensitivity estimation of HADES sensors (see red curve in Figure 8.9):

$$\begin{aligned}
 p(x) = & -2.10445 + 0.186088 (x/^\circ) - 5.8857 \cdot 10^{-3} (x/^\circ)^2 \\
 & + 1.02251 \cdot 10^{-4} (x/^\circ)^3 - 9.34311 \cdot 10^{-7} (x/^\circ)^4 \\
 & + 4.15942 \cdot 10^{-9} (x/^\circ)^5 - 7.09622 \cdot 10^{-12} (x/^\circ)^6 \quad]30^\circ; 180^\circ]
 \end{aligned}
 \tag{8.2}$$

For a measurement at South Pole the deployed transmitters at each stage were used to emit acoustic pulses one by one for a predefined time with the same driving voltage, and all sensors of the SPATS array record the emitted pulses. In [Des 09] this data was clock drift corrected, averaged and used for an attenuation length analysis based on the ratio method. For the analysis in this thesis only the transmitter pulses visible within the HADES A and B data are of interest and the used sensor / transmitter combinations are shown in Table 8.1:

Depth	String D	String A	String B
140 m			BT3
190 m	HADES A		BT4
250 m		AT5	
320 m		AT6	BT6
400 m		AT7*	BT7
430 m	HADES B		

Table 8.1: Combination of HADES sensors and transmitter pairs with visible ($\text{SNR} > 2$) transmitter signals (after clock drift correction and averaging). Distance string D to A: 246 m and from string D to B: 325 m.

*only visible with HADES B

The angle between a line connecting transmitter with sensor and the horizon is defined as *opening angle* of the transmitter; positive above and negative below the horizon. With all combinations given above a maximum opening angle of -41.7° (from BT3 to HADES B) is possible. It is assumed that the ring shaped transmitters are isotropic in azimuth, isotropic in zenith angle range from $\pm 41.7^\circ$ and that all emit the same acoustic pulse. With the known positions of the SPATS array and the assumption that the HADES sensors are frozen in absolutely vertically the zenith sensitivity can be measured in-situ.

Using the high quality data set from [Des 09] the noise corrected peak to peak amplitude, the zenith angle and the distance d were calculated for each HADES sensor / transmitter combination. With help of the attenuation length λ (see Section 4.3.2) the amplitude values at 1 m distance to the HADES sensors were calculated with:

$$A_0 = A(d) \frac{d}{1 \text{ m}} e^{\frac{d-1 \text{ m}}{\lambda}}$$

The dominant error contribution is the attenuation length uncertainty.

A scale factor was applied to the result (different for HADES A and B) in a way that the distances between the measured data points and the parameterized expectation based on laboratory measurements (see Equation 8.2) were minimal. The result for HADES A DS2(2) (blue) and B DS6(2) (green) in comparison with the parameterized laboratory zenith measurement (red) is presented in Figure 8.10.

It is visible that even without the assumption of a non-vertical orientation (could be different for HADES A and B) it is not possible to reach an agreement between all data points and the parameterized zenith sensitivity. BT4 and AT5 are seen by HADES B under nearly the same zenith angle and the received sensitivity should agree within the uncertainties with the assumption of an isotropic transmitter pulse in azimuthal direction. Possible explanations for the disagreement could be non comparable transmitter to transmitter pulses (strong zenith/azimuth dependence or pulse to pulse variations) or transmitter shadowing effects caused by the IceCube cable.

As examples the averaged and clock drift corrected AT5 transmitter signals in time and frequency domain received by HADES A, B and SPATS CS5(1) are pictured in Figures 8.11, 8.12 and 8.13, respectively.

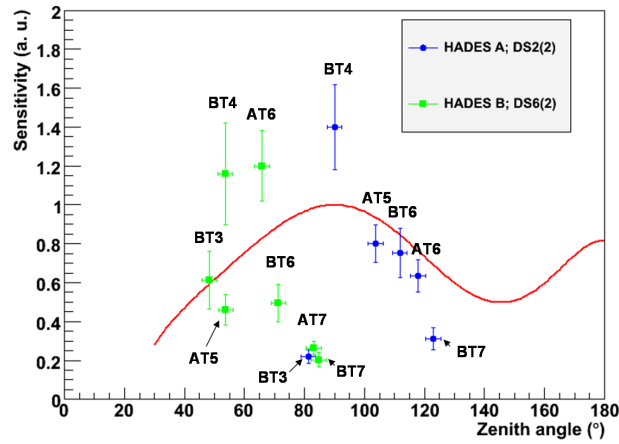


Figure 8.10: In-situ measurement of relative zenith sensitivity of HADES sensors with several frozen in transmitters. The scaled and attenuation length corrected received peak to peak amplitude is shown in comparison with the zenith sensitivity measured in laboratory and parameterized via Equation 8.2 (red).

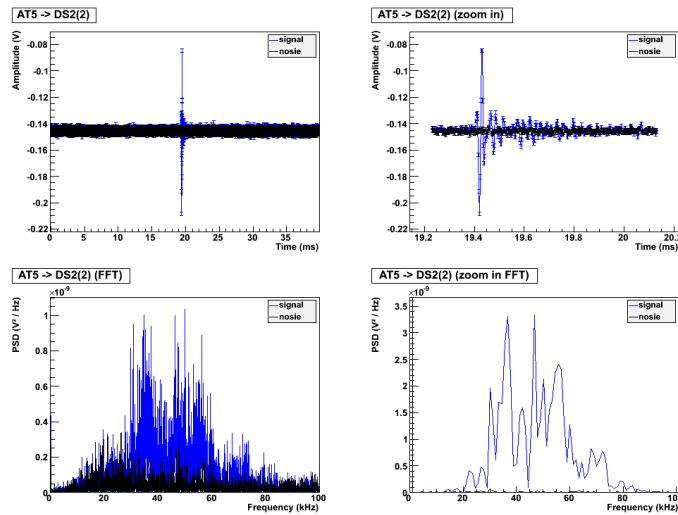


Figure 8.11: Averaged and clock drift corrected transmitter pulse; emitted by transmitter at string A level 5 (250 m deep), and received with HADES A (190 m deep). The signal (blue) and a corresponding noise measurement (black) are shown in time and frequency domain.

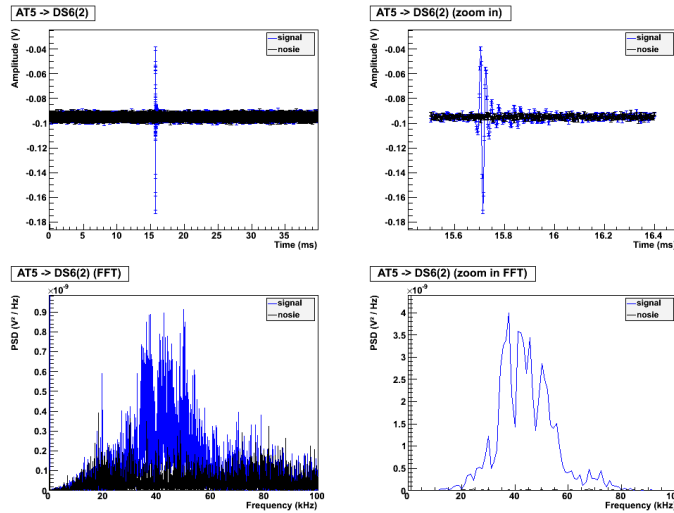


Figure 8.12: Averaged and clock drift corrected transmitter pulse; emitted by transmitter at string A level 5 (250 m deep), and received with HADES B (430 m deep). The signal (blue) and a corresponding noise measurement (black) are shown in time and frequency domain.

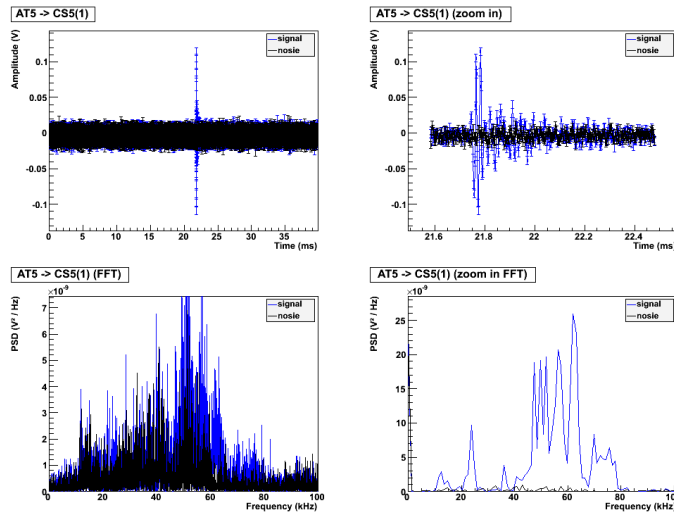


Figure 8.13: Averaged and clock drift corrected transmitter pulse; emitted by transmitter at string A level 5 (250 m deep), and received with SPATS sensor level 5 channel 1 at string C (250 m deep). The signal (blue) and a corresponding noise measurement (black) are shown in time and frequency domain.

8.2 Self-noise

The air temperature dependence self-noise of the HADES sensors down to -60°C were investigated with a freezer¹. How the self-noise level at a certain temperature was received will be described by a typical measurement with HADES A (1) at -40°C and the results are shown in Figure 8.14.

At each temperature setting one noise waveform with a length of 10 ms were recorded every second for a duration of 20 s (= 20 noise waveforms per temperature setting). One waveform is shown in time and frequency domain in 8.14 a) and 8.14 c), respectively and a Gauss fit shows the expected Gaussian distribution of the noise 8.14 b). The desired standard deviation (RMS) value in the time domain within the frequency range of interest from 10-50 kHz can be calculated with the help of the integral over the power spectral density (in the frequency range of interest). See Appendix A.5 for details. This has been done for all 20 waveforms at that temperature and the RMS values versus run number are shown in 8.14 d). To extract the final noise value with RMS for this temperature the mean (mean RMS) and RMS (RMS of mean RMS) of the distribution shown in 8.14 d) is calculated via a Gauss fit (Figure 8.14 d)). Compare Figure 8.15 b) at -40°C .

The temperature dependence self-noise of all four HADES sensors available yield similar results and all show a decreasing self-noise RMS with decreasing temperature. For example the self-noise versus temperature for HADES A (1) for the full frequency range and from 10-50 kHz is shown in Figure 8.15 a) and 8.15 b), respectively.

All acoustic sensors deployed in South Pole ice are switched on permanently. This could cause an increased self-noise caused by self heating (thermal noise) of the amplifier. To take this into account for self-noise measurements in laboratory the frequency of the self-noise measurement has been changed. Instead of every second one noise waveform every minute (= 20 minutes per measurement) was recorded. As visible in Figure 8.15 the RMS values (black data points) agree with the measurements done at shorter time intervals within their uncertainties.

To investigate the contribution of acoustic background noise picked up in laboratory, one noise measurement was done with a capacitor connected to the amplifier (and not coated with resin) instead of a piezo element.

¹model: MDF 492; <http://www.sanyo-biomedical.de>

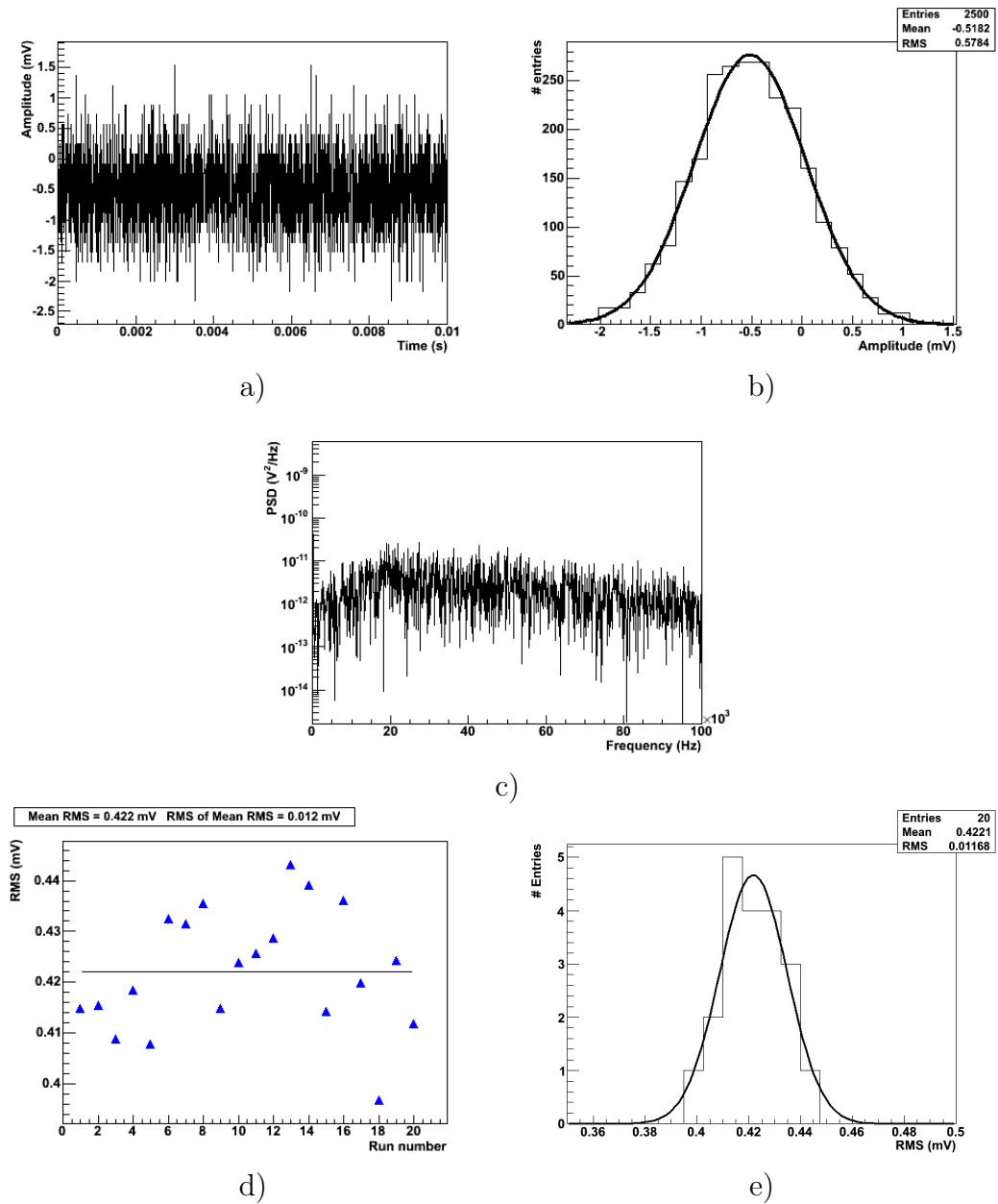


Figure 8.14: Noise waveform recorded with HADES A (1) at -40°C air temperature in time a) and frequency c) domain. The noise waveform histogram with Gauss fit in b) shows the Gaussian distribution of the noise (full frequency range). 20 measurements were taken and the RMS in the frequency range from 10 - 50 kHz versus run number is shown in d). The mean and the RMS of this distribution is calculated e).

The capacitance of a piezo electric element used for HADES B type sensors was measured in the frequency range from 1 -100 kHz with 8.5 nF to 3 nF between 20°C to -80°C (the capacitance measurement procedure is described in section 6.2). For the noise measurement a capacitor with 6.8 nF ($\pm 10\%$) was chosen. Comparing Figure 8.15 a) with 8.15 c) showing the full spectrum noise measured with HADES A (1) and with the capacitance, leads to the conclusion that both measurements agree within their uncertainties and therefore no external noise were picked up.

All 5 self-noise measurements (HADES A (1) and (2), HADES B (1) and (2) and amplifier with capacitor) agree within their uncertainty. Error on the fitted slopes are minimum 18%. Therefore the self-noise is dominated by the amplifier and independent of the device connected to the amplifier. In the South Pole ice a temperature of -50°C is expected. For the final HADES sensor self-noise value all measurement results at this temperature, limited to a frequency range of 10 - 50 kHz, have been averaged and the result is (mean and RMS): 0.416 ± 0.006 mV.

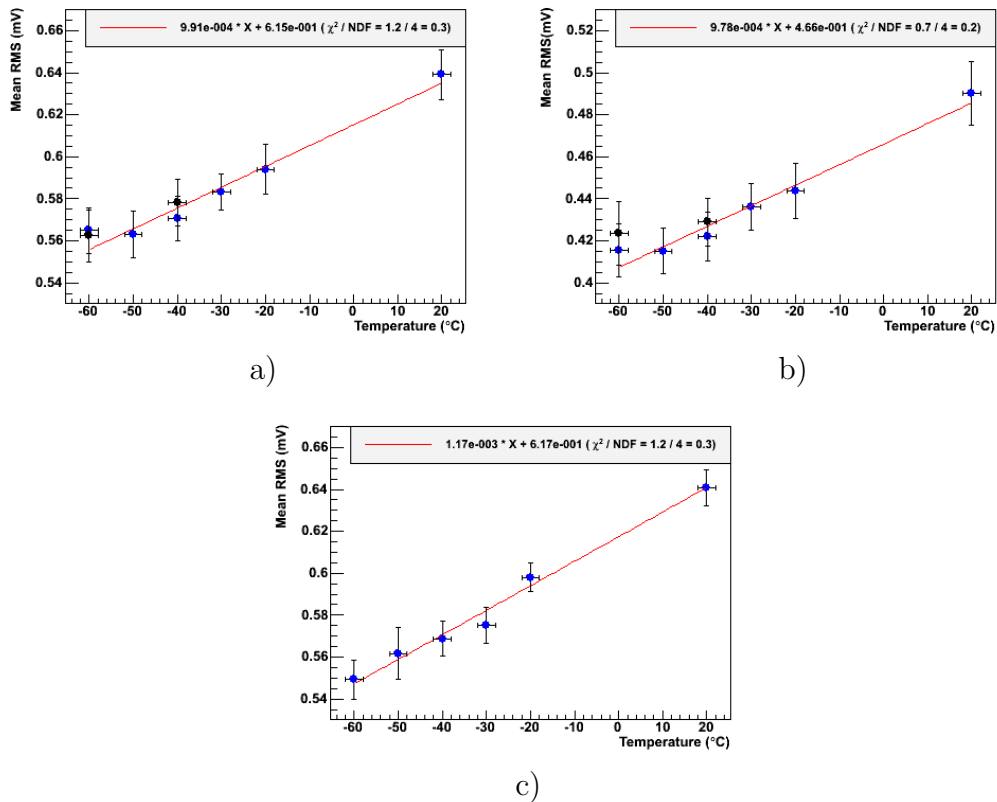


Figure 8.15: Mean RMS versus temperature measured with HADES A (1); full frequency range a) and frequency range from 10-50 kHz only b). Blue data points base on 20 measurements each with 1 measurement per second and the black data points base on 20 measurements each with 1 measurement per minute. c) represents a full frequency range Mean RMS distribution received via a 6.8 nF capacitor connected to the amplifier instead of a piezo ceramic element. The line fits for all three plots do not take the black data points into account.

8.3 Sensitivity change with temperature

To investigate a possible sensitivity change due to decreasing temperatures, data taken with the following setup have been analyzed.

For a meaningful measurement it is important to change only the temperature of the receiver and to provide stable transmitter pulses while the transmitter is always located in a location with constant temperature. For all measurements the receiver was located inside an air filled freezer at a fixed position and the pinger equipment of season 08/09 located outside the freezer at a fixed position at room temperature were used to generate stable acoustic pulses. Due to the strong pinger pulses the freezer could stay closed for all measurements.

At each temperature step 40 single pinger pulses (reflection free) and corresponding noise were recorded. After averaging in time and frequency domain the noise subtracted energy was calculated. This measurements had been accomplished for all four HADES sensors available at temperatures from 20°C down to -60°C. All measurements yield the same result within their uncertainties, and an exemplary plot for the noise subtracted energy versus air temperature is shown in Figure 8.16. No change in sensitivity with decreasing (air) temperature is visible within the uncertainty.

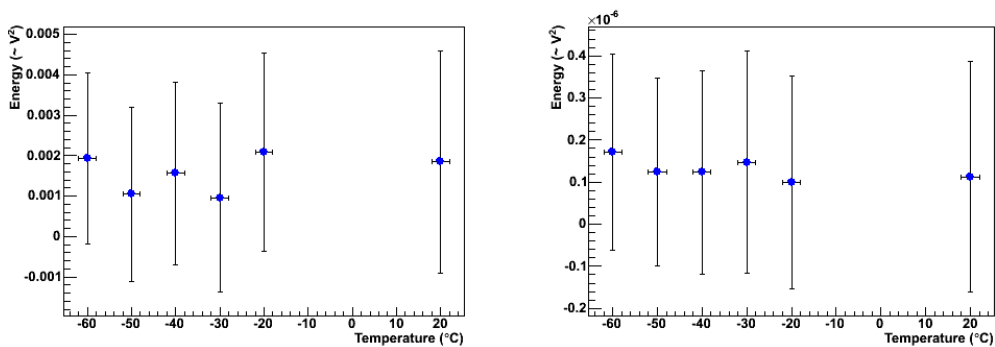


Figure 8.16: Calculated pinger signal energy (self-noise subtracted) versus air temperature for time (left side) and frequency (right side) domain in the frequency range from 10- 50 kHz. No sensitivity change with temperature is visible.

8.4 Calibration in water

The two HADES B (1) and (2) sensors have been calibrated in ice (see next Section 8.5). In ice the azimuth angle variation cannot be corrected, because the devices are frozen and therefore the calibration setup, shown in Figure 6.10 was used. In AAL narrow Gauss shaped pulses were used instead of sine waves at discrete frequencies due to dimensions of the IceTop tank. The transducer driving current has been measured via impedance measurement and the current was corrected afterwards off-line, because the driving current measurement technique via coil was not available at that date. To study the uncertainty contributions due to the setup, the described in-ice setup was used inside the water tank.

Due to the fact that the azimuthal orientation of the sensors inside the ice is unknown the azimuthal average sensitivity of both sensors have been measured using the ice calibration setup in water (water temperature $+18^{\circ}\text{C}$ and a triangle side length of 60 cm). A top view of the calibration setup inside the water tank is shown in Figure 8.17 and the sensitivity result is presented in Figure 8.18. On the left the sensitivity per azimuth angle setting is pictured and on the right the calculated average sensitivity is visible.

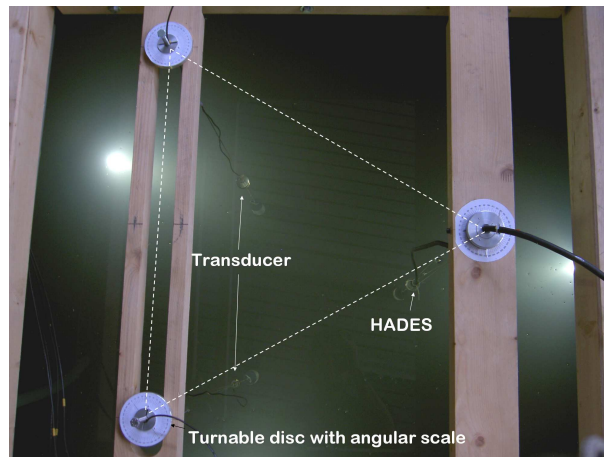


Figure 8.17: Top view of the calibration setup inside the water tank. The equilateral triangle (dashed lines) built by the transducers and the sensor, mounted on a turnable disc with angular scale, is visible.

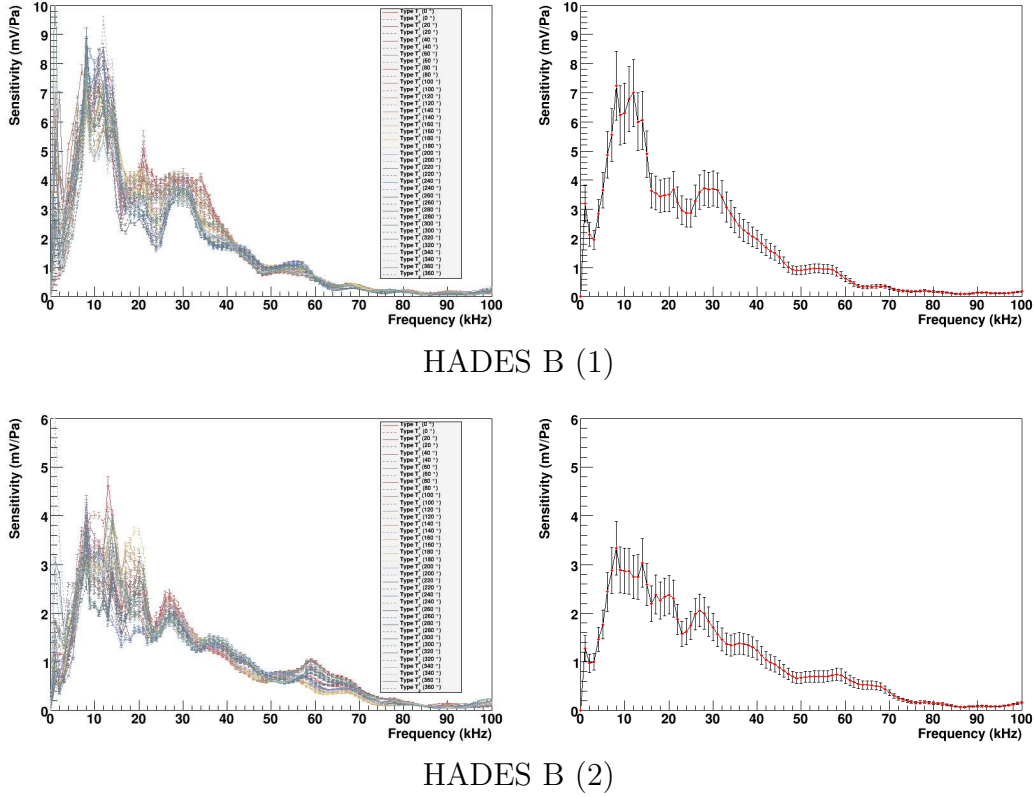


Figure 8.18: Calibration results for HADES B (1) and (2) in water. The ice calibration setup was used and the sensitivity of the sensors for different azimuth angles have been measured (left side). The average sensitivity is shown on the right side (error bars are spread of data points) and the average sensitivity between 10 - 50 kHz for HADES B (1) and (2) is 3.11 ± 0.11 mV/Pa and 1.69 ± 0.08 mV/Pa, respectively.

The average sensitivity between 10-50 kHz for HADES B (1) and (2) is 3.11 ± 0.11 mV/Pa and 1.69 ± 0.08 mV/Pa, respectively. Measurements with HADES A (1) and (2) show a sensitivity of 4.76 ± 0.05 mV/Pa and 4.84 ± 0.07 mV/Pa, respectively. The higher sensitivity of HADES A type sensors in comparison with HADES B type sensors is in agreement with the different piezo electric element specifications. The piezo electric charge coefficient for HADES A type piezo elements is higher than for HADES B type piezo elements (see Section 5.2). The maximum sensor to sensor variation is present in HADES B type sensors and therefore an uncertainty due to sensor to sensor variation of 50 % need to be taken into account.

To quantify the uncertainty caused by the described ice setup in comparison with the Rome calibration setup the SQ03 was again calibrated in water using the ice setup (Gauss pulse, no azimuthal correction) and the azimuthal orientation of all three devices were modified systematically. The azimuthal modifications for SQ03 are shown in Figure 8.19.

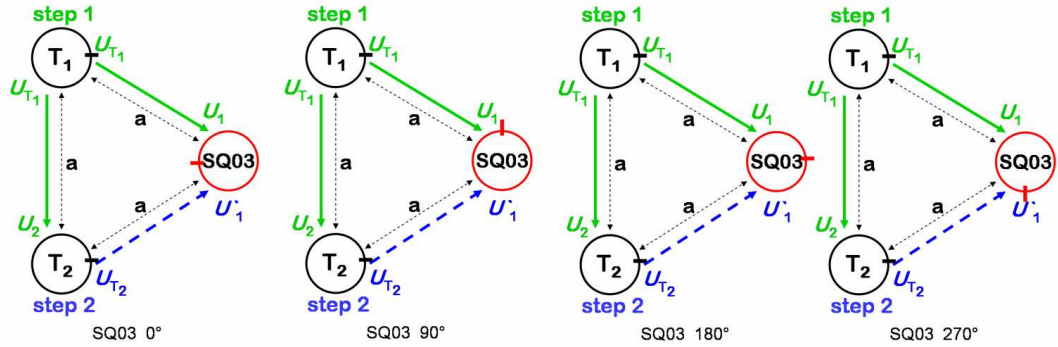


Figure 8.19: Schematic drawing of in ice calibration setup with systematic modification of the azimuthal orientation of SQ03.

The results of these measurements are shown in Figure 8.20. Comparing the averaged sensitivities in the frequency range from 10-50 kHz with the Rome calibration result an uncertainty of 19% due to the setup need to be taken into account.

For calibration via the reciprocity method in water the azimuthal variation of the devices should be taken into account and as calibration pulses sine waves at discrete frequencies should be used (requires a sufficient water volume). When adapting the reciprocity method to ice a correction for azimuth angle variation is not possible and due to the ice volume broad band Gauss pulses (in frequency) has been used. As shown above these differences cause an systematic uncertainty in comparison with the reciprocity method in water of 19%.

Due to the fact that the azimuthal angle of the frozen in HADES sensors is unknown, an averaged sensitivity has been calculated. The uncertainty of the averaged sensitivity is much smaller than the found sensor to sensor variation up to 50%. Reasons for that could be quality differences between two piezo ceramic elements of the same type.

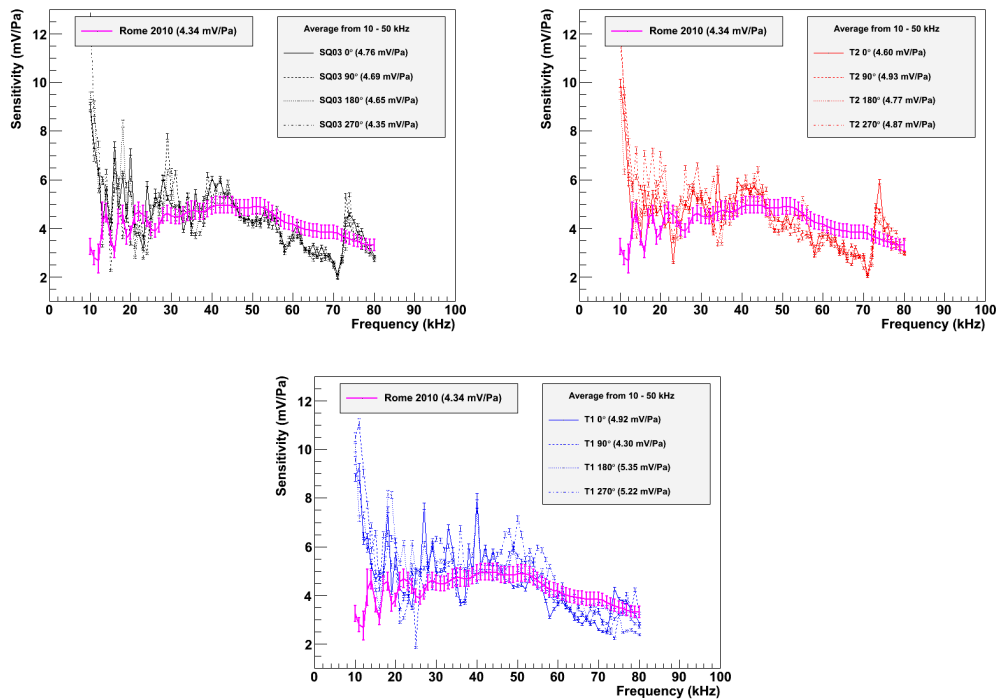


Figure 8.20: Sensitivity of SQ03 measured via the ice calibration setup in water in comparison with the sensitivity result from Rome 2010. The azimuthal orientation of the used devices have been modified systematically and the averaged sensitivity between 10 - 50 kHz of SQ03 is given in brackets. The described current overestimation is corrected.

8.5 Calibration in ice

For the in ice calibration the Aachen Acoustic Laboratory (AAL), described in Section 7.2, has been used. Beside the HADES sensor calibration setup a positioning system with three levels of *Murata* [Mur 08] sensor / transmitter pairs was installed in this freezing cycle in the IceTop tank.

On the left in Figure 8.22 the positioning system is shown and on the right a side view of the IceTop tank with the installed positioning system is visible. In Figure 8.24 a top view of the IceTop tank is presented with the location of the Murata sensor / transmitter pairs. It is referred to each pair via two digits; the first digit represents the level (counting from top to bottom) and the second stands for the pair inside the level. Details about positioning system, sensor characteristics and sensitivity can be found in [Pau 10], [Meu 10] and [Sch 09].



Figure 8.21: The positioning system; three levels equipped with six Murata sensor / transmitter pairs per level [Sch 09].

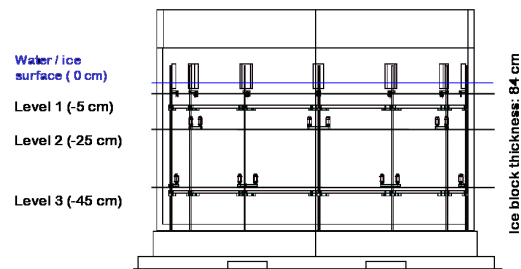


Figure 8.22: Schematic drawing (side view) of the IceTop tank including the positioning system with the three levels of sensors / transmitters (nominal depth) [Meu 10].

For the in ice calibration an equilateral double triangle with a nominal side length of 60 cm containing the two HADES B type sensors and transducer T_1 and T_2 was installed. The installation depth in the IceTop tank was 27.5 cm below the water / ice surface. In ice the distance between the devices has been measured via signal transit time and the corresponding speed of sound at this temperature. The results are presented in Table 8.2. An average value of 59.6 ± 1.2 cm has been used for the sensitivity calculations. The dominant error contribution is the uncertainty on the speed of sound.

Due to the small ice volume in AAL in comparison with the water volume in Wuppertal and the doubled speed of sound from water to ice, a narrow signal time window has to be used to exclude signal reflections in ice calibration data. In [Zie 10] the absolute position of the HADES calibration setup inside the IceTop tank was measured (see Figure 8.24). With the maximum speed of sound (determined via the lowest reachable temperature of -21.6°C) a signal time window for in ice calibration without the influence of reflections of $145\ \mu\text{s}$ has been calculated. The distances between the devices of the HADES calibration setup received via signal transit time and via location reconstruction in [Zie 10] agree within their uncertainties.

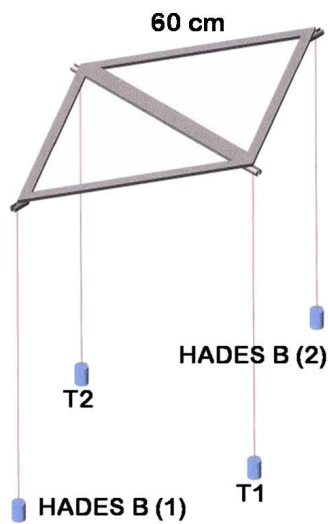


Figure 8.23: Artist view of the installed equilateral double triangle [Lai pr] with a nominal side length of 60 cm.

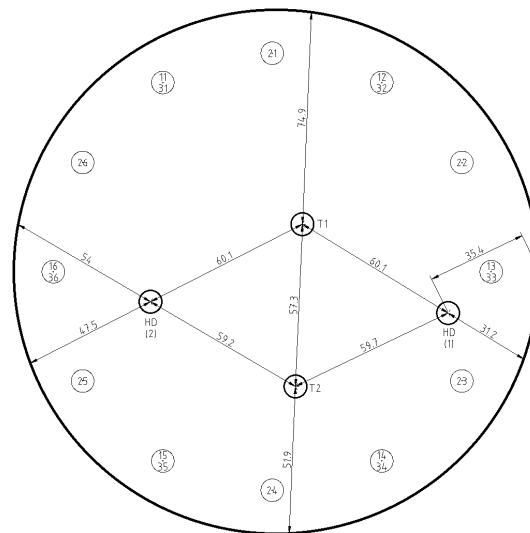


Figure 8.24: Top view of the IceTop tank with installed HADES calibration setup and Murata sensors. Distances are given in cm with an accuracy of 0.5 cm and they base on measurements published in [Zie 10].

Before the freeze cycle, calibration measurements in water at $+13.0^{\circ}\text{C}$ and $+4.0^{\circ}\text{C}$ have been done (without correcting for azimuthal angle like in the ice phase). After the production of the clear block of ice, the calibration measurements started at the lowest temperature of -21.6°C and were repeated at -20.5°C , -19.1°C , -18.0°C , -15.6°C , -13.0°C , -9.6°C and -5.75°C .

	T ₁	T ₂
HADES B (1)	60.4 ± 0.4 cm	59.6 ± 0.4 cm
HADES B (2)	60.4 ± 0.4 cm	59.6 ± 0.4 cm
T ₁	***	58.8 ± 0.4 cm
T ₂	58.8 ± 0.4 cm	***

Table 8.2: Distance matrix for the in ice calibration setup in AAL received via signal transit time measurements and the corresponding speed of sound. An average value of 59.6 ± 1.2 cm has been used for the sensitivity calculations.

At each temperature several measurements have been done. Three different narrow Gauss pulses (distinguished via their half width σ) and the two calibration types were used. The driving current was not measured inductively, because this was not available at that date, but the results have been corrected for this effect off-line.

All sensitivities at -21.6°C are shown in Figure 8.25. Similar to the water measurements in Wuppertal an excess around the 10 kHz region is sometimes visible. The excess is independent of the used calibration pulses and arbitrary visible in both sensors. Reasons for that are unknown.

All 12 measurements per temperature were averaged to derive a mean sensitivity at this temperature. The mean sensitivities are shown in Figure 8.26 and the average sensitivity between 10-50 kHz is calculated. All averaged ice sensitivities with an uncertainty of 10% each, agree within their errorbars. Therefore no increase in sensitivity with decreasing temperature can be seen. In addition in Figure 8.26 the measured sensitivities in the water phase at 4°C and 14°C are shown. Comparison between the averaged water and ice sensitivities show an increased sensitivity in the ice phase. The piezo ceramic resonance frequency around 48 kHz is only visible in ice. An increase in sensitivity from water to ice is in agreement within the data of the commissioning (see Figure 5.10). Possible reasons for the sensitivity increase have been mentioned in Section 5.2.

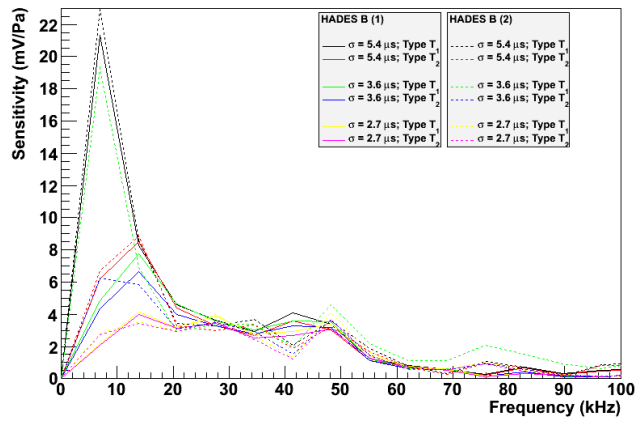


Figure 8.25: Calibration results (current corrected) at -21.6°C ice temperature and $145\ \mu\text{s}$ signal time window. The used three different Gauss pulses are distinguished via their half width σ . Type T_1 and T_2 represent the two setup configurations.

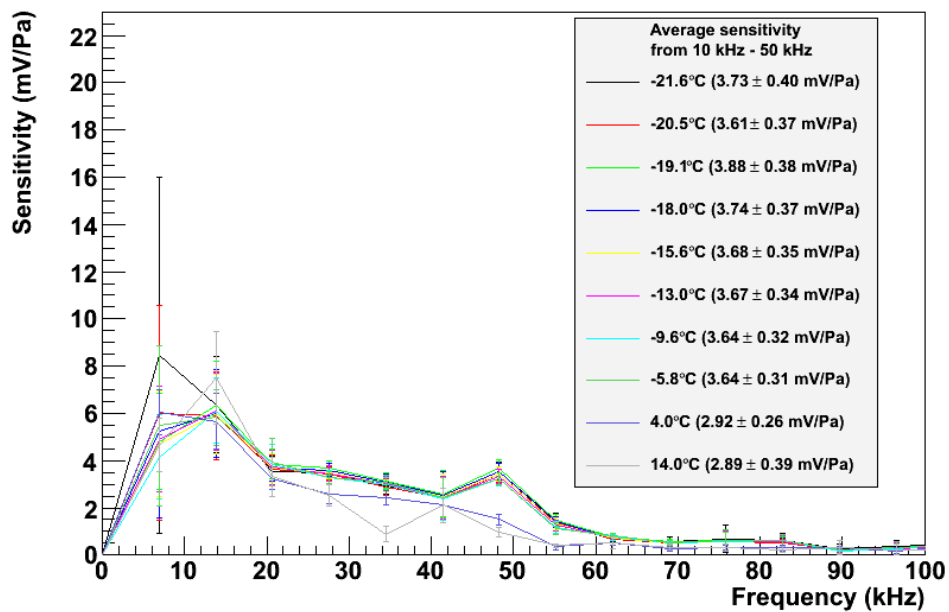


Figure 8.26: Averaged sensitivities, current corrected, at different temperatures (12 single measurements per temperature). The average sensitivity between 10-50 kHz is given in brackets.

At each temperature step 12 measurements have been done. For each single sensitivity (current corrected) at a temperature below 0°C the average between 10-50 kHz was calculated and the results are presented via a histogram in Figure 8.27. In the previous section a sensor to sensor variation from HADES B (1) to (2) of 50%, based on averaged azimuth sensitivity measured in water, was derived. Here in ice both sensors are frozen at a fixed but arbitrary angle and the sensitivities are similar.

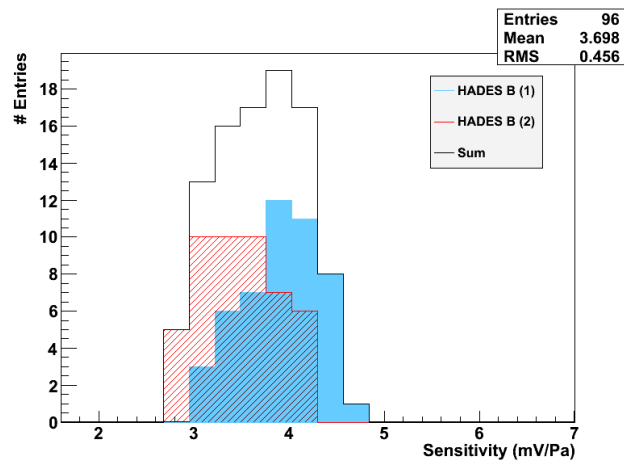


Figure 8.27: Averaged sensitivity (between 10-50 kHz) for every single calibration measurement result in ice (current corrected) for HADES B (1) and (2). Averaged sensitivity is 3.70 mV/Pa ; 12 sensitivities per temperature times 8 different temperature steps.

For a final ice sensitivity of HADES B type sensors the results are averaged to a mean sensitivity of 3.70 mV/Pa with a systematic uncertainty from 50% due to sensor to sensor variation from the water measurements. As mentioned before the averaged sensitivities for ice agree within their uncertainties of 10% and no increase in sensitivity with decreasing temperature is visible within this uncertainty. Therefore the derived sensitivity can be adapted for HADES B (at -50°C) deployed at the South Pole.

8.6 In-situ calibration

The retrievable transmitter - the pinger - is used as a calibrated sound source to derive the sensor sensitivity via in-situ measurements.

For an in-situ calibration the absolute emitted acoustic pulse of the transmitter needs to be known and all effects disturbing the sound propagation need to be taken into account. The pinger was used for the first time in the austral summer season 2007/2008 and string D was installed, too. The pinger is a good candidate for this in-situ calibration, because the emitted acoustic pulse has been investigated (theoretically and experimentally) after the deployment at South Pole. The analysis of pinger pulses received with HADES is described now followed by the theoretical and experimental examination of the absolute pinger output, and based on a combination of both a absolute HADES sensitivity is calculated. For comparison sensitivity estimations for selected SPATS sensors will be given at the end.

String D was deployed in IceCube hole #76. Before that, the pinger was used in hole #55, #71, #70 and #76 and hence no pinger data of these holes could be recorded with string D and the HADES sensors. In Figure 8.28 only the holes pinged after string D deployment are marked. IceCube hole #77 was pinged at December 28th, but string D was not frozen in completely, so no pinger data could be recorded. With the last pinger hole #69 pinged at January 2nd, 2008, pinger pulses could be recorded with string D and the HADES sensors.

In the season 2007/2008 the pinger depth inside the hole was determined by five pressure sensors and via counting turns of the winch spool. The winch diameter (as a function of number of cable layers on the spool) and the cable diameter was used to convert from the number of spool turns to depth of the pinger [Van pr]. The pressure sensors were not very well calibrated and the pressure values varied, converted to depth, up to ≈ 80 m. A visualization of the depth in hole #69, measured by one pressure sensor, is shown in Figure 8.29. All depth values correspond to the floor inside the *Tower Operations Structure* (TOS); therefore “depth below TOS”. Also during IceCube deployment itself, this is used as the definition of the top of the hole and all depths are measured from that level.

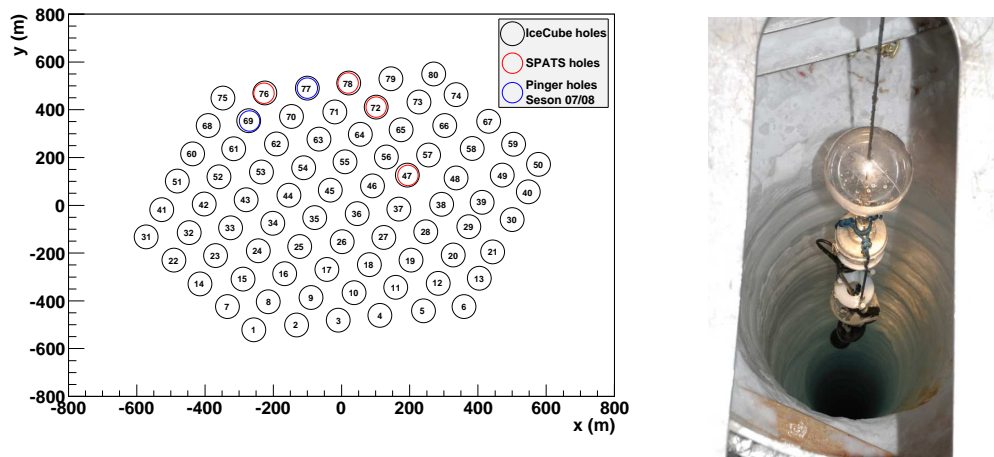


Figure 8.28: Location of IceCube holes used for pinger runs after the installation of string D in season 2007/2008 (on the left) and pinger lowered into an IceCube hole (on the right) [Tos 10].

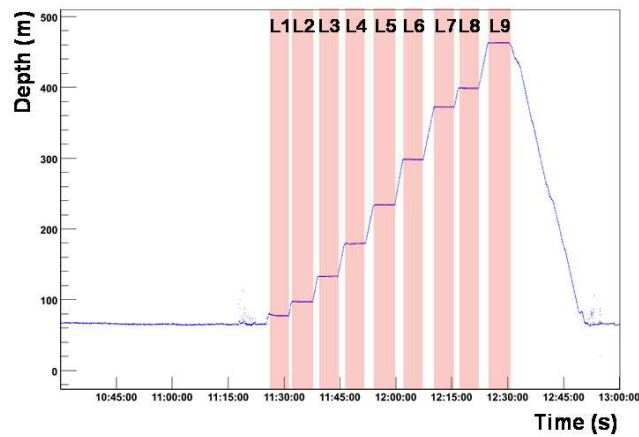


Figure 8.29: Pressure data converted to depth for one pressure sensor of pinger hole #69 [Van pr], the pinger depth versus time with the marked stop levels is shown.

Combining the five pressure sensors with the turn counting data yields the final pinger depth values for hole #69:

Stop level	Depth below TOS (± 5 m)	Nominal
L1	80.0 m	80 m
L2	100.1 m	100 m
L3	138.1 m	140 m
L4	186.4 m	190 m
L5	243.1 m	250 m
L6	309.8 m	320 m
L7	384.7 m	400 m
L8	412.1 m	430 m
L9	476.8 m	500 m

Table 8.3: Final pinger stop depth for hole #69 calculated via the mean of the depth received via turn counting and pressure sensor data [Van pr]. The stop depth below TOS (Tower Operations Structure) for each stop level (LX), corresponding to the nominal instrumented sensor levels, is given in the table.

Assuming the pinger ball with a diameter of 10 cm and the pressure wave is emitted from the surface of the ball located in the middle of an IceCube hole with a diameter of 70 cm, the pressure wave needs to travel through 0.3 m of $\approx 0^\circ\text{C}$ cold water. With a speed of sound $v_{\text{water}}(0^\circ\text{C}) = 1402 \frac{\text{m}}{\text{s}}$ it takes about 0.2 ms. The measured sound speed in ice at that depth is $v_{\text{ice}} \approx 3880 \frac{\text{m}}{\text{s}}$ (see Section 4.3.1) and therefore the horizontal signal transit time for 125 m to a nearby hole is $0.2 \text{ ms} + 32.22 \text{ ms} = 32.42 \text{ ms}$. The horizontal location uncertainty for the pinger ball and the frozen sensor is ± 5 m and ± 2 m, respectively, which would add a distance uncertainty of 0.2 m or 0.05 ms. Summation with the charge time of the pinger ball of 1.90 ± 0.05 ms [Tos 10] yields 34.32 ± 0.07 ms. The trigger signal is synchronized to a GPS clock and starts with the beginning of each second. Also the SPATS data acquisition receives GPS time and therefore the sent pinger pulse should arrive 34.32 ± 0.07 ms after each starting second. Later, one pinger waveform emitted at stop level L8 will be analyzed, which needs additional 0.33 ms to the transit time due to a vertical offset between TOS and nominal depth of 18 m.

Each recorded waveform is 9 s long and should contain nine pinger pulses (see Figure 8.31). Above, a transit time of 34.3 ms was calculated but this is true for the horizontal path only. To include inclination range the expected arrival time is extended to 40 ms. To find waveforms with 9 pulses stable in amplitude and clear above noise, each waveform is divided into nine sequences and each sequence starts with the beginning of a second. For each sequence the maximum peak to peak amplitude within the first 40 ms “signal time window” with one ADC count as uncertainty is plotted versus start time of each waveform in Figure 8.30.

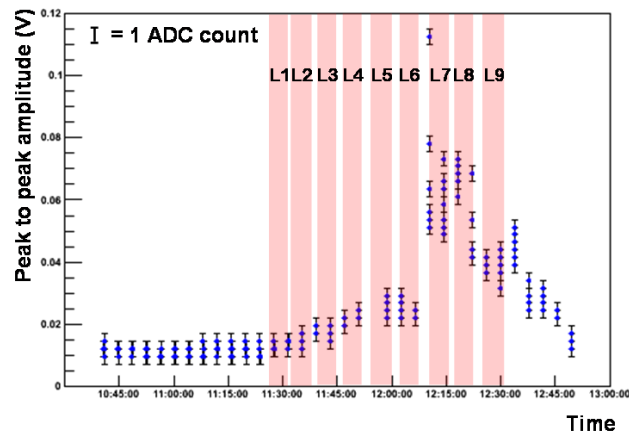


Figure 8.30: Peak to peak amplitude (signal) vs. time inside a 40 ms time window following each starting second measured with HADES B for pinger lowered inside hole #69 (L7 nominal 400 m and L8 nominal 430 m deep; sensor located at a depth of 430 m).

As expected the strongest amplitudes are visible at pinger stop level L7 and L8 (nominal 400 m and 430 m deep; sensor located at a depth of 430 m). But as one can see due to marked stopping times waveforms are recorded right at the beginning or really close to the end of the stopping times. Therefore it is unknown if the pinger is still moving or already moving and this is nicely underlined with a huge spread of peak to peak amplitudes within one waveform. The one “stable” waveform (first measurement at L8) shows the same peak to peak amplitude in every sequence within six ADC counts. This waveform is shown in Figure 8.31 on the left side. The waveform in the frequency domain (right side) shows a modulation with ≈ 5 kHz and can be caused by e. g. generators used during the deployment season. This is not visible in transient or noise data taken during the none deployment season.

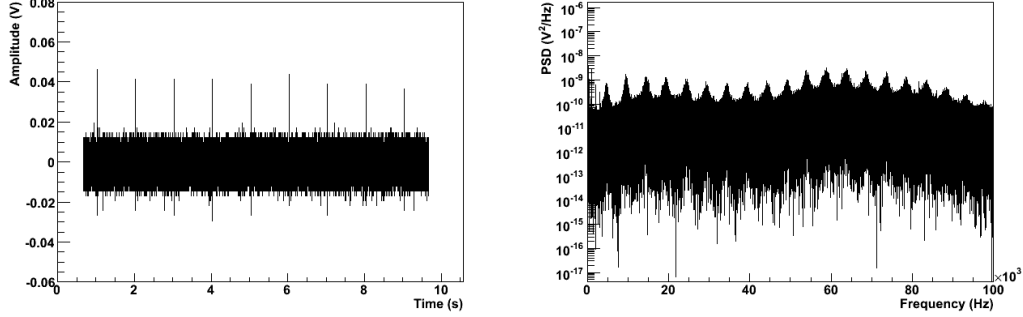


Figure 8.31: Stable pinger waveform in time (left) and frequency (right) domain recorded with HADES B at a depth of 430 m.

For a pinger signal analysis the nine single sequences are averaged and the clock drift need to be corrected before. Figure 8.32 shows a zoom into an overlay of all nine sequences synchronized to the beginning of the second. It is clearly visible that the signals are not aligned. In the plot sequence nine (light blue) is on the left side and sequence one (black) on the right that indicates a negative clock drift. Based on the received signal, a tripolar fit with Amplitude A , μ and σ as free parameters is applied for a better time resolution concerning the position of the signal maximum. As fit function the second derivative of a Gauss pulse

$$f(t) = \frac{A}{\sigma\sqrt{2\pi}} \frac{d^2}{dt^2} e^{-\frac{1}{2}\left(\frac{t-\mu}{\sigma}\right)^2} \quad (8.3)$$

was chosen. A piezo element always emits the second derivative of the (voltage) driving pulse [Lan 91]. Therefore, based on the applied fit function, a Gaussian shaped pulse could be the driving voltage. As shown in Figure 4.4 this is not completely true.

To receive the clock drift rate the position in time μ of each signal maximum, defined by the fit, is plotted versus sequence number normalized to sequence nine, shown in Figure 8.33. The slope of a line fit (red) yields the desired drift rate of $-10.64 \mu\text{s/s}$ or -10.64 parts per million (ppm). The overlay of the nine sequences with clock drift correction is pictured in Figure 8.34 and the averaged signal with RMS is shown in Figure 8.35.

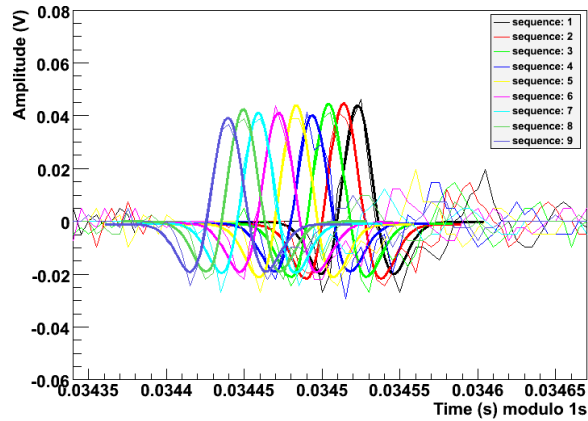


Figure 8.32: All nine sequences, not clock drift corrected, with tripolar pulse fit (bold lines) for a better time resolution of each maximum.

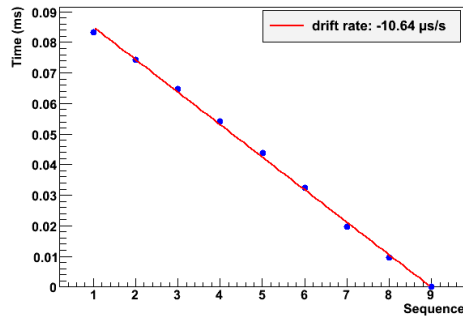


Figure 8.33: Position of each signal maximum per sequence versus sequence number normalized to sequence nine. The slope of a line fit yields the drift rate.

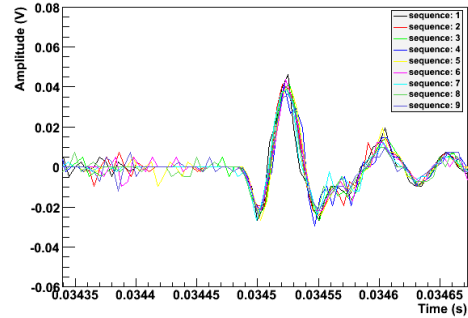


Figure 8.34: All nine sequences clock drift corrected.

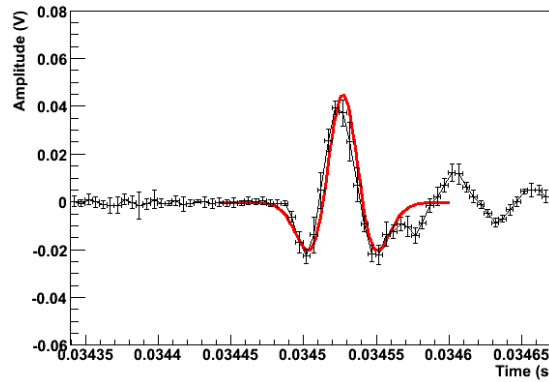


Figure 8.35: Averaged sequences with tripolar fit (red).

For sensitivity calculation the received signal in the frequency domain is of interest. Therefore the averaged sequences were divided in a signal time window and a noise time window of the same length before the signal time window. The Fourier transform of each time window has been calculated.

For comparison and sensitivity calculation the theoretical expected acoustic pinger pulse is needed. With the high voltage read back pulse (HVRB; measured in laboratory) and the transmit voltage response (TVR; based on pinger company information) shown in 4.4 and 4.5 respectively the theoretical expected acoustic pinger output can be calculated and the result is shown in 8.36.

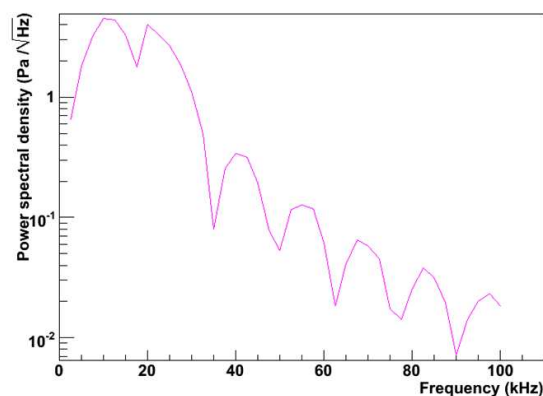


Figure 8.36: Expected acoustic pinger pulse [Abb 1+].

The described signal and noise time window of the in-situ measured pinger pulse is pictured in Figure 8.37 in frequency domain. The (scaled) theoretical pinger output (see Figure 8.36) is shown for comparison. The pinger pulse is visible up to a frequency of 30 kHz but the peaks of the measured pinger signal are shifted to higher frequencies in comparison with the theoretical expectation.

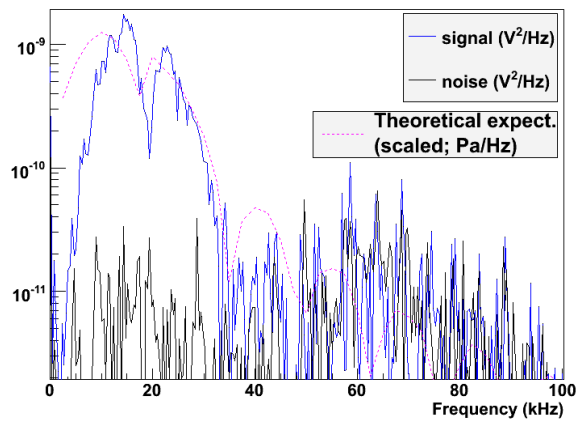


Figure 8.37: Received pinger signal with HADES B and a corresponding noise measurement in comparison with the (scaled) theoretical pinger output.

The big disadvantage of the described clock drift correction is the fact that for the tripolar fit signals clearly above noise are essential. Beside the four waveforms from L7 and L8 no other waveform recorded with HADES shows clearly visible peaks above noise and only the waveform discussed above was stable in amplitude. For an analysis of waveforms with signals hidden in the noise the IRIG-B (100 pps) decoding described in [Des 09] was used to correct clock drift prior waveform averaging.

Pinger swimming pool measurements

To check if the theoretically calculated pinger power spectral density is equal to the real pinger output, measurements in a public swimming pool with the calibrated hydrophone SQ03 as receiver have been done. The big water volume was essential to avoid saturation due to the strong pinger pulse.

The pinger prepared for the pool test is shown in Figure 8.38 and a schematic drawing of the pool setup is presented in Figure 8.39.

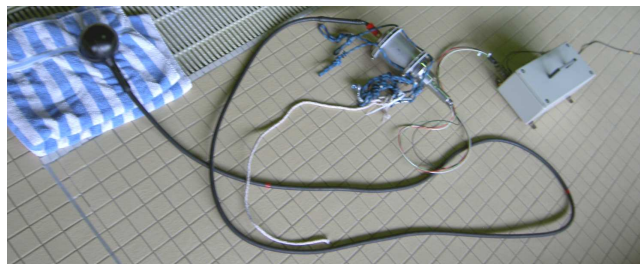


Figure 8.38: Pinger prepared for pool test with pinger ball (black sphere on the left), steel housing with high voltage pulser (metal cylinder in the middle) and the Acoustic Pinger Box (APB; on the right).

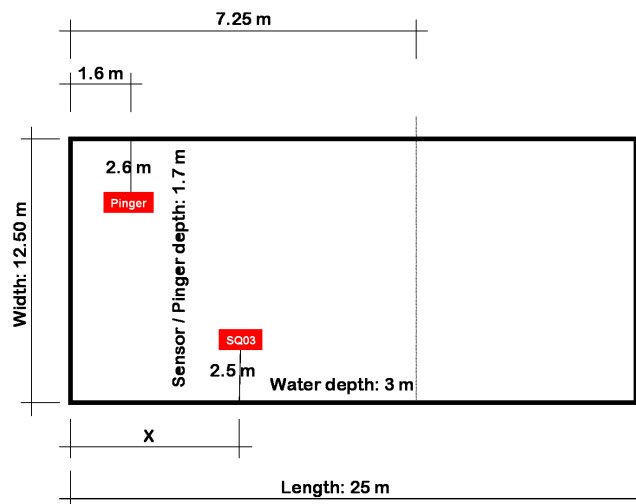


Figure 8.39: Schematic drawing of pool setup for pinger frequency content measurement (setup 1: $X = 4$ m; setup 2: $X = 7$ m).

Measurements with two different distances (differentiated via setup 1 and 2) between pinger and SQ03 of 7.78 m and 9.16 m have been done. 40 single pinger pulses per setting were recorded with SQ03, corrected for $1/r$ dependence and averaged in time domain. With this result the calculated Fourier spectrum was used to determine the absolute frequency spectrum of the pinger with the given sensitivity of SQ03 measured in Rome 2004. In the first pinger season in 2007/2008 one pinger pulse per second (repetition rate 1 Hz) was send. In the following seasons this rate was increased up to 10 Hz and accidentally set to 8 Hz once. Results of the measurements are pictured in 8.40.

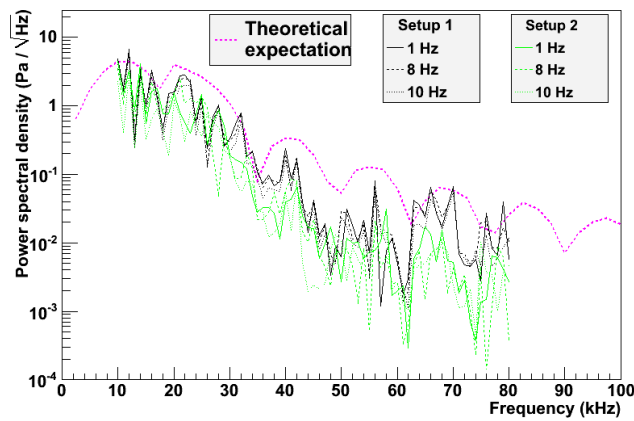


Figure 8.40: Comparison of theoretical pinger frequency power spectrum with pinger measurements done with SQ03 at different repetition rates and distances in a swimming pool.

It is visible that an increase in repetition rate did not decrease the signal strength. The discrepancy between the measured and the theoretical pinger power spectral density in the frequency range from 10-30 kHz is a factor 4.3. Derived via the ratio of the theoretical pinger power spectral density with measurements done with SQ03 in a swimming pool (see Figure 8.41).

A possible factor 2 can be explained via air bubbles (see Section 7.1) and a not present thermal equilibrium between the acoustic devices and the pool water. The measurements have taken place in a public swimming pool during closing hours and it was not possible to wait the required hours to avoid the described effects.

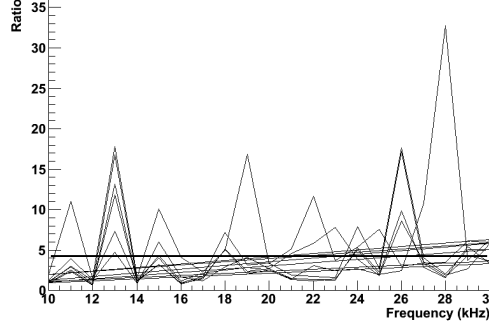


Figure 8.41: Ratio of the theoretical pinger power spectral density with measurements done with SQ03 (see Figure 8.40). A constant line fit leads to a mean ratio of 4.3.

The presented theoretical pinger power spectral density and the in-situ measured pinger signal with HADES B (see Figure 8.37) is used in the following to calculate an absolute sensitivity estimation for HADES B.

HADES B sensitivity estimation

For the final HADES B sensitivity estimation calculation the received signal at one meter distance to the transmitter needs to be calculated. Therefore the distance d between pinger and HADES B is calculated (see Figure 8.42) and the measured attenuation length is used.

To take into account the transition from water to ice, for amplitudes the transmission coefficient t is calculated via $t = \sqrt{1 - r^2}$ (r = reflection coefficient) and considered in the sensitivity estimation. The reflection coefficient can be calculated via:

$$r = \frac{Z_2 \cdot \cos(\alpha_1) - Z_1 \cdot \cos(\alpha_2)}{Z_2 \cdot \cos(\alpha_1) + Z_1 \cdot \cos(\alpha_2)} \quad (8.4)$$

For the impedances Z_1 and Z_2 the following values have been used:

$$Z_1(0^\circ\text{C}) = \rho_{water} \cdot \nu_{water} = 1000 \text{ kg/m}^3 \cdot 1402 \text{ m/s} \quad (8.5)$$

$$Z_2(-50^\circ\text{C}) = \rho_{ice} \cdot \nu_{ice} = 924 \text{ kg/m}^3 \cdot 3878 \text{ m/s}$$

Applying Snellius law and the relation between t and r , mentioned above, the transmission coefficient as function of the emergent angle α_2 can be calculated and is shown in Figure 8.43. To cover variations in the emergent angle (shown in Figure 8.42) an averaged transmission coefficient of 0.9, between $7^\circ - 9^\circ$, is used.

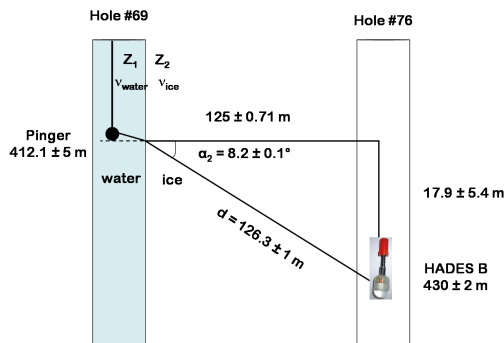


Figure 8.42: Sketch for the visualization of distance d and emergent angle α_2 between pinger and HADES B (pinger season 2007/2008). Uncertainty estimations are adapted from [Abb 10].

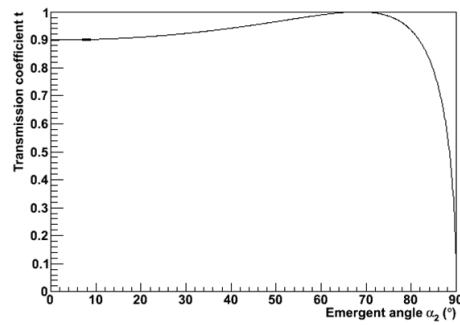


Figure 8.43: Transmission coefficient t versus emergent angle α_2 . Average from $7^\circ - 9^\circ$: 0.9

As described above with the calculated distance d and the measured attenuation length the signal strength at 1 m to HADES B was calculated. In addition the transmission coefficient was taken into account. Combining this result with the theoretical pinger output leads to a HADES B sensitivity, shown in 8.44.

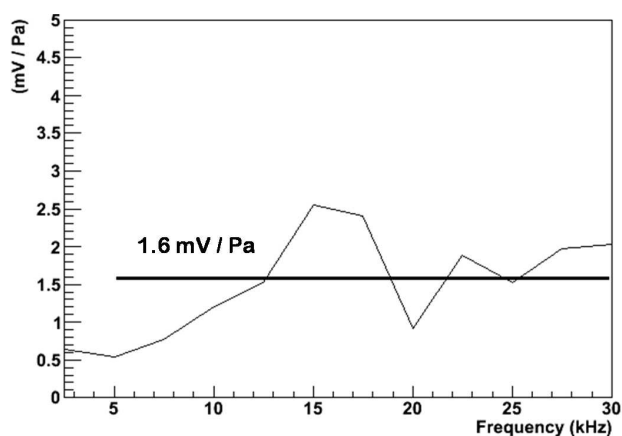


Figure 8.44: HADES B in-situ absolute sensitivity estimation.

The average between 5-30 kHz (pinger emission range) was calculated and the result is a HADES B sensitivity of 1.6 mV/Pa. Averaging the sensitivities from HADES B (1) and (2), measured in AAL in ice, from 10-30 kHz leads to a sensitivity of 4.4 ± 0.6 mV/Pa. The in-situ calibration measurement result differs from the laboratory in ice sensitivity by a factor of 2.75.

Pinger pulses are only visible in HADES sensor data of the first pinger season in 2007/2008. Due to several problems with the data quality of this season described in the pinger section 4.2, one recorded pinger waveform with HADES B was found which was suitable for an in-situ sensitivity estimation described above. No pinger signal at all was visible in the HADES sensors after clock drift correction and averaging applied to pinger data of the next seasons. In the following seasons the pinger position inside the water filled hole was stabilized with *centralizers* (metal springs), pinger pulses with a repetition rate of 10 Hz and waveforms with a length of up to 18 sec were recorded. The pinger was stopped on the way down the hole and back up again at every depth equipped with sensors, and only these horizontal pinger/sensor combinations were used for analysis (schematic drawing shown in Figure 8.45). For comparison with the sensitivity estimation of HADES B, data of selected SPATS sensors of this season were analyzed in the same way and the results are presented in Table 8.4. Each SPATS sensor has been calibrated in water prior deployment (see [Fis 06] for details) and this averaged sensitivity is shown for comparison with in-situ results.

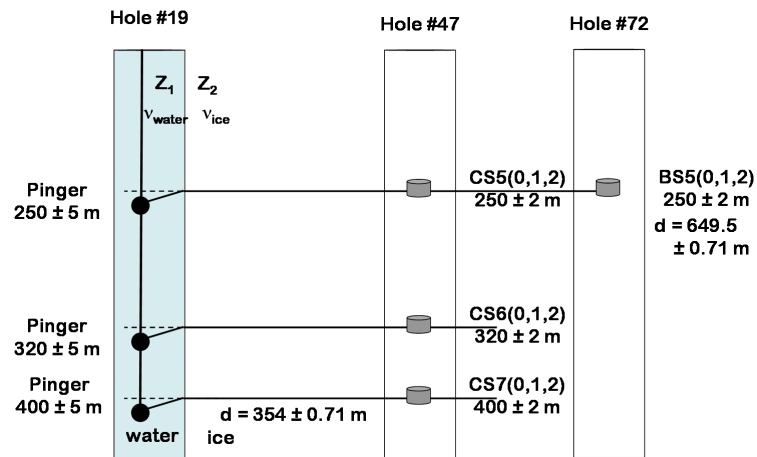


Figure 8.45: Sketch for the visualization of distance d between pinger and selected SPATS sensors (pinger season 2008/2009). Uncertainty estimations are adapted from [Abb 10].

Sensor	depth	Channel 0	Channel 1	Channel 2
CS5	250 m (down)	36.3 mV/Pa	59.4 mV/Pa	56.4 mV/Pa
CS5	250 m (up)	38.5 mV/Pa	54.2 mV/Pa	48.7 mV/Pa
Water	calibration	3.76 ± 0.16 V/Pa	3.82 ± 0.28 V/Pa	4.71 ± 0.20 V/Pa
CS6	320 m (down)	saturation	56.1 mV/Pa	51.8 mV/Pa
CS6	320 m (up)	saturation	58.1 mV/Pa	48.5 mV/Pa
Water	calibration	4.59 ± 0.61 V/Pa	5.72 ± 1.34 V/Pa	5.57 ± 0.96 V/Pa
CS7	400 m	18.8 mV/Pa	23.3 mV/Pa	23.8 mV/Pa
Water	calibration	1.57 ± 0.04 V/Pa	1.85 ± 0.06 V/Pa	1.98 ± 0.05 V/Pa
BS5	250 m (down)*	41.3 mV/Pa	36.0 mV/Pa	47.0 mV/Pa
BS5	250 m (up)	55.4 mV/Pa	72.3 mV/Pa	67.1 mV/Pa
Water	calibration	2.45 ± 0.05 V/Pa	2.65 ± 0.05 V/Pa	2.54 ± 0.05 V/Pa

Table 8.4: Averaged sensitivity (5 - 30 kHz) of selected SPATS sensors based on horizontal pinger measurements in austral summer season 2008/2009 in comparison with averaged sensitivities (10 - 30 kHz) received via water calibration with SQ03 prior deployment (see [Fis 06] for details). The pinger moving direction is given in brackets.

*weak signal to noise ($S/N \approx 2$) after averaging.

The sensitivities of SPATS sensors calibrated in water prior deployment are more than one order of magnitude larger than estimated sensitivities. During the water calibration the corresponding sensor channel pointed to the transmitter, while in ice the sensor orientation is unknown. In [Pau 10] a spare advanced SPATS sensor has been calibrated in water and ice inside the IceTop tank. The sensitivity averaged over all three channels and the frequency range from 10 - 50 kHz received in water is 1.7 V/Pa (22.5 % syst. uncertainty) and in ice 150 mV/Pa (55.7 % syst. uncertainty). This results show also an ice sensitivity which is more than one order of magnitude lower than the corresponding water calibration.

The transmission coefficient was calculated for a plain interface between water and ice. Due to the hot water drilling multiple structures are present on the inner wall. This could cause additional reflections or scattering of the pinger signal.

All or a few of the used sensors could be shadowed by the IceCube cable or/and surrounded by ice of bad quality (e. g. frozen air bubbles) within the hole of the sensor.

If the pinger output were lower than the theoretical calculations (see swimming pool measurements) or if a few or all of the described uncertainties reduce the pinger signal strength, the received sensitivities would increase.

All systematic uncertainties for HADES sensor corresponding to the in-situ calibration with the pinger as calibrated transmitter is listed below:

<i>HADES</i>	
Azimuthal variation	40%
Zenith variation*	100%
Sensor to sensor variation	50%
Calibration setup	19%
<i>Pinger</i>	
Power output variation	77%
Total error	143%

Table 8.5: Systematic uncertainties for HADES sensor corresponding to the in-situ calibration with the pinger as calibrated transmitter.

*can be reduced when the source location is known

Chapter 9

South Pole ice properties

In this Chapter the noise data, measured with HADES A and B in the year 2009, will be analyzed. With the sensor self-noise and the in-ice sensitivity of HADES B the South Pole noise level will be calculated and an explanation for the measured noise variation with time will be discussed. This is followed by a transient sound source location reconstruction.

9.1 South Pole noise

To monitor the background noise conditions in South Pole ice each deployed SPATS array sensor is taking *noise data* once every hour. Each untriggered waveform (0.1 s/hour) is recorded with a sampling frequency of 200 kHz. For the year 2009 all available noise data, taken with the two HADES sensors, were analyzed. The ADC count distribution ($24 \text{ h} \times 0.1 \text{ s/h} \times 200 \text{ ksamples/s} = 480 \text{ ksamples}$) for one day of noise data taking with HADES A and B is shown in Figure 9.1.

A Gaussian distribution (red) of ADC values is visible and the standard deviation (RMS) is a measure for the noise level in the sensor, which is a superposition of sensor electronic self-noise, electromagnetic interference picked up on the signal cable from the sensor to the surface¹, and possible acoustic noise contributions from the surrounding ice.

¹The signal is transmitted differentially from the sensor to the ADC, therefore electromagnetic interference should be small.

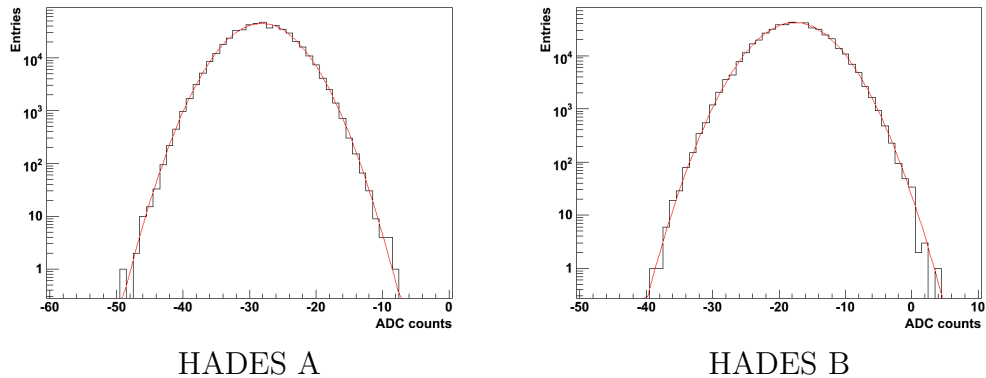


Figure 9.1: Distribution of ADC values from one day of noise data with Gauss fit (red).

We are interested in the noise contribution within a frequency range from 10-50 kHz. The RMS in this range for each recorded noise waveform versus time is shown on the left side of Figure 9.2. If entry i was not recorded (due to power outages for example) the RMS value is received via the average of the neighboring bins $((V(i-1) + V(i+1))/2)$.

Both noise distributions are flat and the visible noise RMS increase in HADES A & B at the end of the year is related to the beginning of the drilling / deployment season 2009/2010 at South Pole. The outliers distributed over the hole year could be caused by transient acoustic events or by a temporarily increased noise level.

To receive the South Pole noise RMS, measured by the HADES sensors (including the self-noise), the described data are shown in a histogram and a Gauss fit yields the desired RMS value (see right side of Figure 9.2). A comparison between the Gauss fit and the data shows an asymmetry towards higher RMS values, which could indicate an additional noise contribution to the sensor self-noise.

The South Pole noise measured with HADES A and B is 0.487 ± 0.006 mV and 0.454 ± 0.005 mV, respectively in a frequency range from 10-50 kHz. As shown in Section 8.2 the sensor self-noise is independent of the used piezo element type and both values are higher than the measured self-noise at -50°C , which could also indicate that additional noise is present.

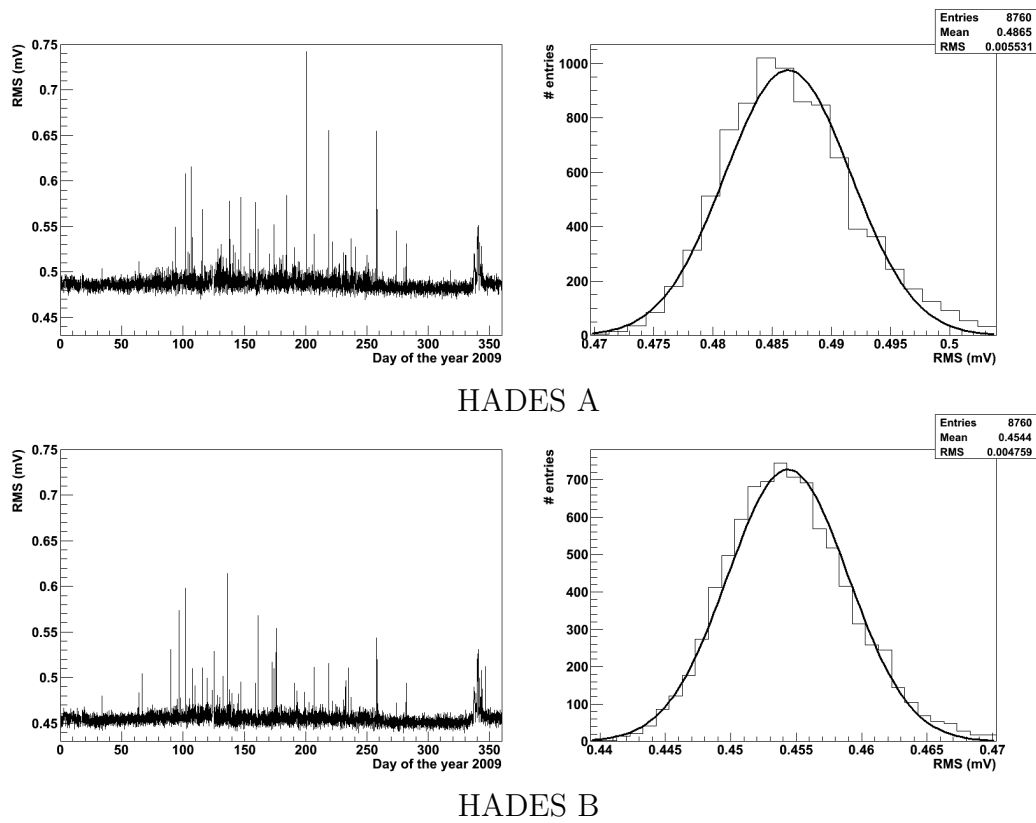


Figure 9.2: Noise RMS values (in frequency range from 10 kHz to 50 kHz) versus time for HADES A & B (left side) and histogram of these data with Gauss fit (zoom) to receive the mean of the RMS with sigma (RMS of the mean RMS) value (right side).

As mentioned above the sensor self-noise (caused by the amplifier) is independent of the used piezo element type, but temperature dependent. An ice temperature of -50°C is assumed and the averaged HADES self-noise at -50°C measured in laboratory (between 10 - 50 kHz) is: 0.416 ± 0.006 mV (see Section 8.2).

HADES A and B contain different type of piezo electric elements and only two HADES B type sensors have been calibrated in ice, because AAL was not available for an in-ice calibration of HADES A type sensors. Therefore only the noise measured with HADES B is used for a South Pole noise level calculation.

The sensor self-noise must be subtracted from the measured noise level quadratically to receive the South Pole noise level equivalent; the result is 0.182 mV.

In Section 8.5 the sensitivity of HADES B type sensors was measured and the averaged sensitivity from 10 - 50 kHz is 3.70 mV/Pa. It has been shown that this sensitivity is independent of the ice temperature (within 10% uncertainty) and therefore it can be used to convert the South Pole noise level into the equivalent pressure South Pole noise level between 10 - 50 kHz which is 49 mPa.

In Section 8.4 a systematic uncertainty of 50% due to HADES B type sensor to sensor variation and an uncertainty due to the calibration setup of 19% has been derived. Therefore a total systematic uncertainty of 53% need to be applied.

In this thesis an equivalent pressure South Pole noise level between 10 - 50 kHz (at a depth of 430 m) of 49 ± 26 mPa is calculated.

In [Abb ip] a mean noise level between 10 - 50 kHz in South Pole ice of 14 ± 3 mPa was estimated. Only SPATS sensors at string A-C located below 200 m have been used. SPATS sensors at string A-C reach a depth of 400 m and therefore the 14 ± 3 mPa correspond to a depth between 200 m and 400 m.

In [Abb 10] the gradient in the speed of sound indicates that the noise from the surface will be refracted back upwards. If the surface noise is the dominant noise source the deeper ice regions would be shielded and a decreasing noise level with depth would be expected. The derived noise levels between 10 - 50 kHz of 14 ± 3 mPa for a depth between 200 m to 400 m and

49 ± 26 mPa at 430 m are not in agreement or indicate a noise level decrease with depth. One possible explanation could be that some systematic uncertainties were not taken into account.

The Fourier transform of the presented noise RMS values have been studied and the results will be discussed now.

With the noise RMS values versus time shown on the left side of Figure 9.2 the Fourier coefficients have been calculated and the results are pictured in Figure 9.3. As one can see a modulation within these South Pole noise data recorded with both HADES sensors of 24 h and its harmonics are visible. The phases of both HADES sensors at a periodicity of 24 h are in agreement (95°). The analysis of the corresponding noise data recorded with the SPATS sensors (first and second generation) do not show this modulation with time! As random example the Fourier coefficient of SPATS sensor channel DS5(2) is shown.

It has been assumed that this modulation could be explained via power consumption variation of the South Pole station and the various experiments. For the year 2009 the power consumption of the IceCube Laboratory (ICL), where the SPATS array is connected to, and the total power produced by the generators at South Pole, known as Primary Main Distribution Equipment (PMDE), has been provided by [Mil 10]. The power consumption versus time and the corresponding Fourier coefficients for both are shown in Figure 9.4. The visible minima in time domain are related to power outages.

The ICL and its power consumption monitoring shows a periodicity slightly below 24 h and the total power produced at the South Pole shows a periodicity of exact 24 h and its harmonics. The SPATS array is connected to the ICL and the ICL receives the power from PMDE. Therefore it is likely that total power consumption variations due to the PMDE are visible at the ICL. The question: “Why is the noise variation visible in the HADES sensors and not within SPATS sensors?”; could be answered with the used amplifier board. The SPATS array sensors are receiving the same power (from the ICL) and inside each sensor housing the same type of voltage converter board is used. In comparison with the SPATS sensors in HADES only one sensor channel present. Therefore one out of three power channels from the voltage converter board is connected to the amplifier board which is different in comparison with the SPATS sensors.

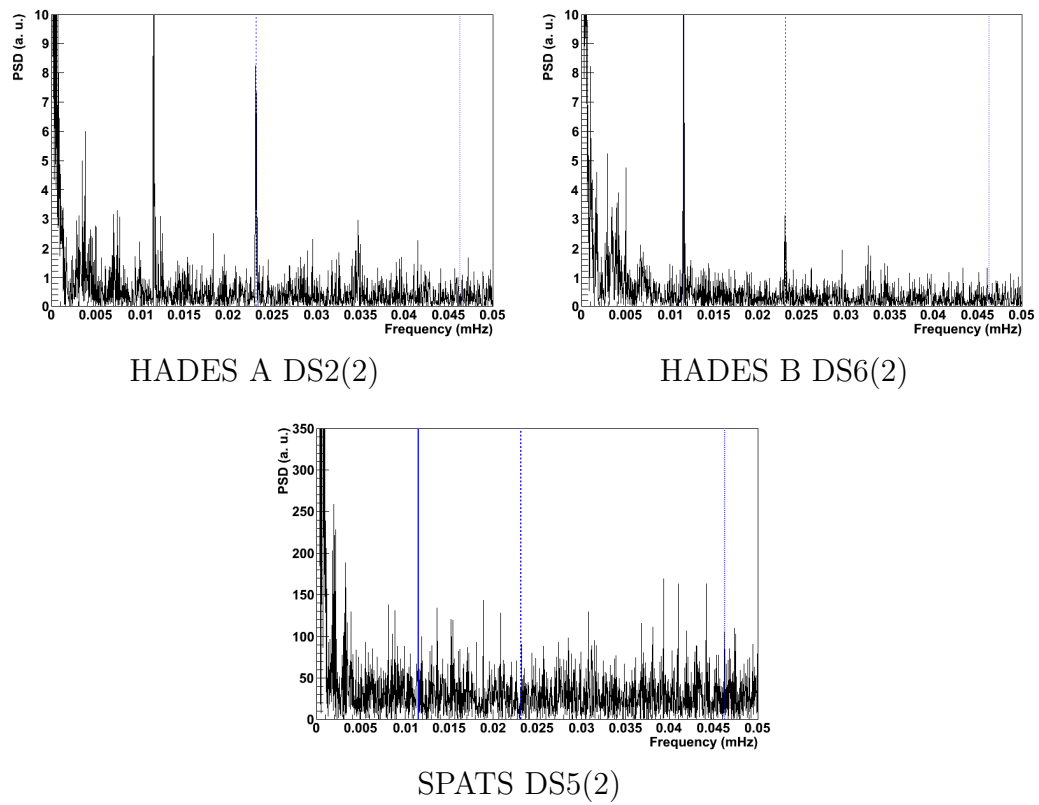
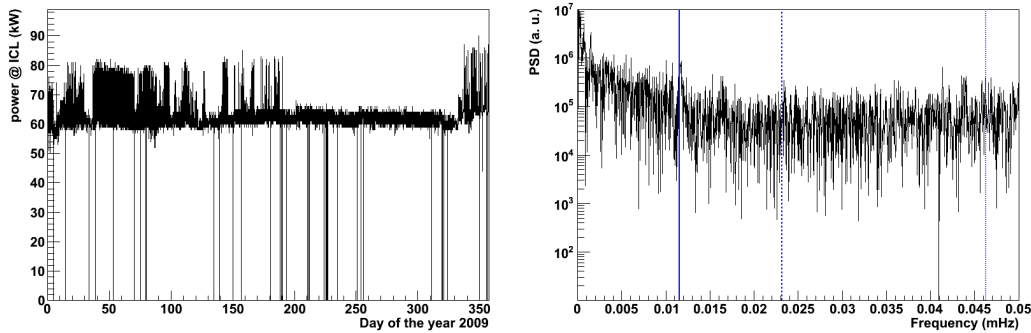
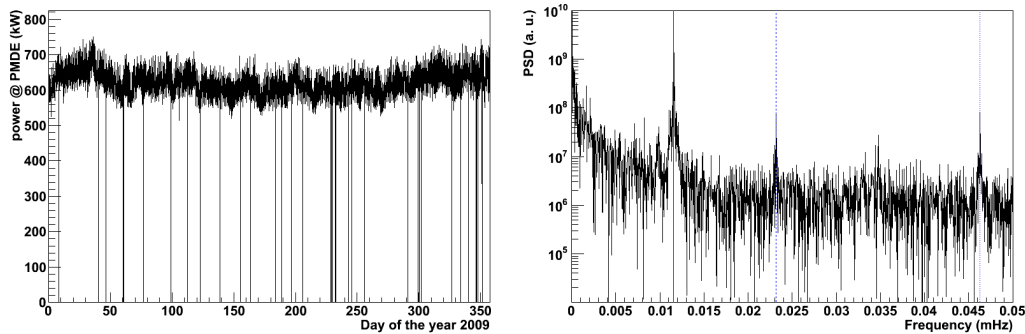


Figure 9.3: FFT of RMS noise data versus time (shown in Figure 9.2 for HADES A and B) (solid blue line: 24 h period; dashed blue line: 12 h period and dotted blue line: 6 h period).



IceCube Laboratory (ICL)



Primary Main Distribution Equipment (PMDE)

Figure 9.4: Power consumption of the IceCube Laboratory (ICL) and the total power at South Pole produced by generators both in time and frequency domain for 2009 (solid blue line: 24 h period; dashed blue line: 12 h period and dotted blue line: 6 h period).

As mentioned before the phases of HADES A and B at a periodicity of 24 h are in agreement. In addition a visible 24 h variation in the PMDE and ICL power monitoring was presented. With the possibility that the amplifier board electronics used with HADES sensors is more sensitive to power variations in comparison with the SPATS amplifier, the visible noise variation with time (only visible with HADES) can be explained with power consumption variations at South Pole.

9.2 Transient event location reconstruction

The rate and amplitude distribution of acoustical transient background events is an important quantity for future acoustical and/or hybrid neutrino detectors deep in the South Pole ice, because these background events will influence the discrimination from neutrinos. As a first step a simple transient event location reconstruction will be presented now.

Inside each String PC three ADCs are located and each of the three channels per sensor housing is connected to a different ADC board. With the first version of the installed DAQ on the String PCs we were able to record one channel per ADC at once. During this transient data taking configuration used for the present analysis, HADES A at a depth of 190 m was used beside 11 other SPATS sensor channels. All used sensor channels are shown in Table 9.1. From sensor BS6 two channels were recorded, but only channel BS6(0) was used for this transient event location reconstruction because the event arrival time in these two channels would agree inside the assumed signal arrival time uncertainty (see below for details).

Instrumented depth (nominal)	String A	String B	String C	String D
80 m				***
100 m				***
140 m				
190 m	AS4(2)		CS4(2)	DS2(2)
250 m	AS5(1)	BS5(1)	CS5(1)	DS3(1)
320 m	AS6(0)	BS6(0) BS6(2)	CS6(0)	DS4(0)
400 m				
430 m	***	***	***	
500 m	***	***	***	

Table 9.1: Used sensor channels for transient data taking during quiet period from July 1st to October 22nd 2008. BS6(2) was not used for transient event location reconstruction. String depth marked with “***” are not equipped with acoustic stages.

During the austral summer seasons e. g. hole drilling and IceCube string deployment is ongoing at the South Pole. For transient events analysis this time is treated as *drill period* and it covers the time range from November 1st

to February 28th². In contrast to that the time without man-made activities is called *quiet period* and covers the time range from March 1st to October 31st. To avoid the possibility of man-made transient events in this analysis, data taken during the quiet period were analyzed. From July 1st to October 22nd 2008 HADES A was used within the configuration described above and for analyzing data with a stable configuration this time range is used for the analysis described below.

For the first 45 min of each hour the 12 sensors took data in *threshold mode* (remember: only 11 sensors are used for analysis). If the amplitude crosses the threshold of 5.2 times the noise sigma in the SPATS sensors or 7 times the noise sigma in the HADES A sensor, the waveform with 1001 samples and a sampling frequency of 200 kHz is recorded. The trigger threshold of HADES A is increased in comparison with the SPATS sensors, because the dynamical range of HADES sensors is smaller and they are much more sensitive to small amplitude variations. The search for coincident events was done off-line.

Due to the high trigger threshold in HADES A, it is assumed that every recorded waveform by this sensor is a potential acoustic event. Two arbitrary chosen triggered waveforms are shown in Figure 9.5.

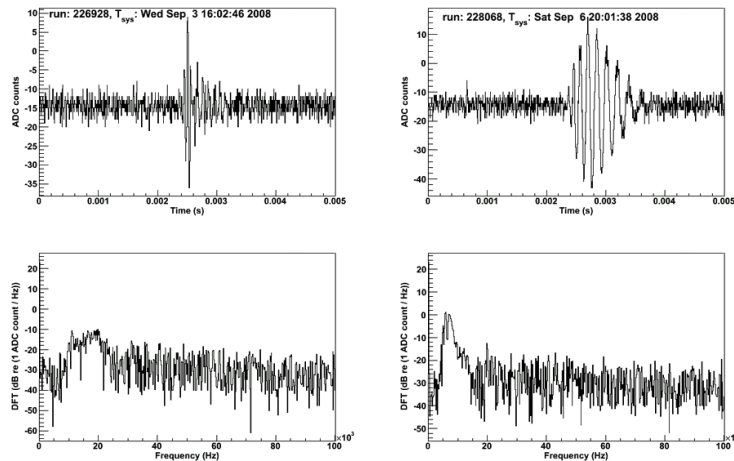


Figure 9.5: Arbitrarily chosen transient events recorded with HADES A in time and frequency domain.

²or February 29th at a leap year

The given time stamp (via GPS time) of each event specifies the beginning of the waveform. The bin, which causes the trigger, is always located in the middle of the signal time window. Therefore the *hit time*, used for reconstruction, is defined via the GPS time + $0.5 \times$ signal time window length. Due to the fact that we have different thresholds in HADES A and SPATS sensors (= different hit times), an uncertainty of $1/3 \times$ signal time window length (5/3 ms) to each hit time is applied to take the different hit times into account.

The hit time of each triggered HADES A event determines the center of a coincidence time window for the search of events recorded by SPATS sensors, also characterized via their hit time. The total time window length used in this analysis is 250 ms to cover the whole detector.

If a hit, detected by SPATS sensors, is present inside the chosen coincident time window, it is checked for being a real *acoustical waveform* and not a hit triggered by noise called *noise waveform*. A triggered hit by noise would contain one sharp peak only (often one bin) above threshold. In contrast to that an acoustical hit contains a sequence of bins with smooth ADC (amplitude) values which represent the acoustic signal. This is used to distinguish between a noise hit and an acoustical hit in a way that bin i with the maximum amplitude value U_{\max} is compared to the neighboring bins $i+1$ and $i-1$. If $U_{i+1} > 0.5 \times U_{\max}$ and $U_{i-1} > 0.5 \times U_{\max}$ is fulfilled, this hit is treated as an acoustical event and the hit time is used for transient event location reconstruction. If this is not the case only the corresponding sensor will not be taken into account for the location reconstruction.

From time to time transient bursts occur which exceed the transient event recording time and cause a second trigger right after the recording of the first event. If more than one event of a certain SPATS sensor is present inside the coincident time window, only the first hit time of the sensor is used for transient event location reconstruction.

For transient event location reconstruction it is assumed that the transient sound was emitted at time t_0 at the location defined by x_0, y_0 and z_0 and the position of the HADES A and SPATS sensors is known and can be described via x_n, y_n and z_n . Together with the speed of sound of $v_{\text{sound}} = 3878 \text{ m/s}$ ³ a set of equations yield the desired transient event location:

³As shown below no transient event below a depth of 300 m was found and therefore this speed of sound was chosen (compare to Figure 4.7)

$$(x_n - x_0)^2 + (y_n - y_0)^2 + (z_n - z_0)^2 - [v_{sound}(t_n - t_0)]^2 = 0 \quad n \geq 4 \quad (9.1)$$

The number n of sensors inside the coincidence window (including HADES A) is called *multiplicity*. As shown in the Equation above in addition to HADES A minimum three other SPATS sensors are needed to record an event inside the coincidence time window (multiplicity $n \geq 4$). With the known location and the hit time of all sensors inside the coincidence time window the most likely location of the transient event is calculated with Equation 9.1 via χ^2 minimization using the TMinuit package from ROOT [TMi 09] (uncertainties: $\sigma_{x_n, y_n} = 1$ m, $\sigma_{z_n} = 2$ m, $\sigma_{t_n} = 5/3$ ms and $\sigma_v = 12$ m/s). For this analysis multiplicity $n \geq 5$ is required. Reconstructed event locations with $n \geq 4$ would normally contain a huge uncertainty and therefore a high χ^2 / NDF value. Most of these events would not pass a χ^2 / NDF quality cut. The reconstructed transient event locations are shown in Figures 9.6 and 9.7 with quality cut conditions $\chi^2 / \text{NDF} < 25$ and $\chi^2 / \text{NDF} < 8$, respectively. The open circles at $z=0$ represent the IceCube holes and are no miss reconstructed events!

In Figures 9.6 and 9.7 the IceCube footprint (without DeepCore) is marked with open black circles and the location of the SPATS array is indicated with black stars. All other symbols beside the colored dots represent the location (in x and y) of the so-called *Rod well*. This is a short form of *Rodriguez well*, which represents one of the two persons who invented the cavern in the ice to store the hot water during IceCube hole drilling [Sch 62]. A schematic drawing is shown in 9.8. The figures behind the word Rod well present the season when the Rod well was used.

As shown in Figures 9.6 and 9.7 the refreezing IceCube hole # 70 (hole drill completed at December 21st 2007) and the Rod well from season 07-08 can be clearly identified as sound source of transient events. Rod well transient events are clustered at a depth of ≈ 100 m, but some occur down to a depth of ≈ 200 m and these transients are not aligned to the upper events. As seen in Figure 9.8 the maximum refreezing water volume, producing the transient events, is located 150 m deep. From reconstruction it seems that the “real” Rod well position is shifted to hole 62 (see Figure 3.4), and the transient event locations are not centered at one certain point. With simulations in [Ber 10] it is shown that the so-called *smearing effect* of the reconstructed event locations could be explained via the depth depended sound speed (see Figure 4.7) which was assumed to be constant in this analysis.

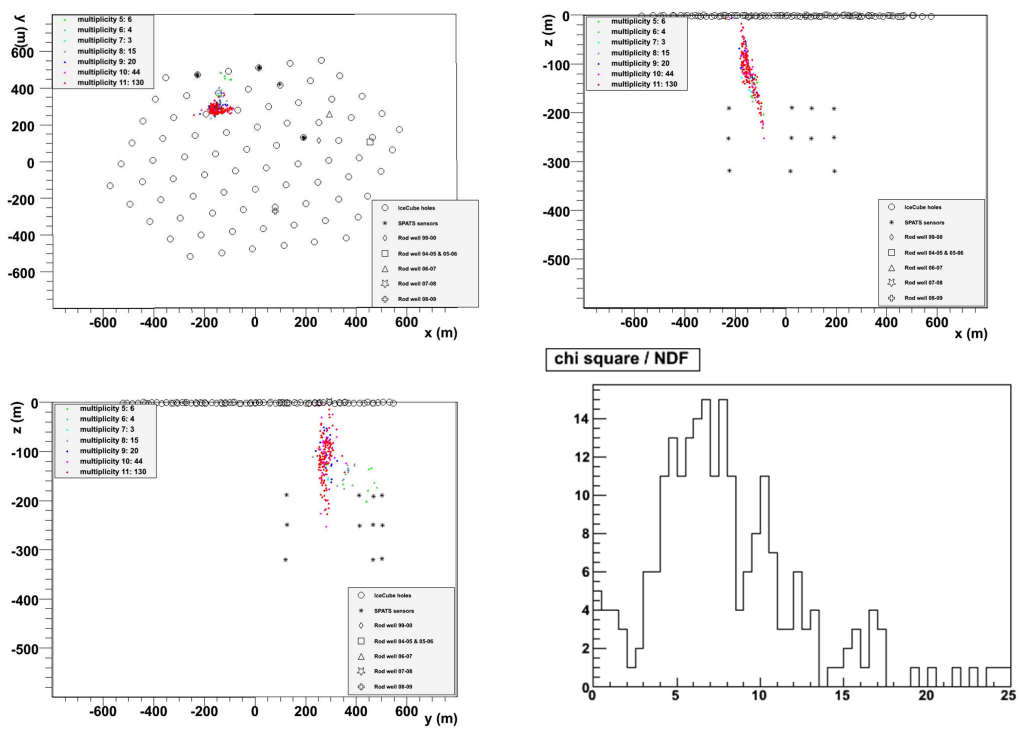


Figure 9.6: Reconstructed transient events from July 1st to October 22nd 2008 (quiet period) with $\chi^2 / \text{NDF} < 25$. The open circles at $z=0$ represent the IceCube holes and are no miss reconstructed events.

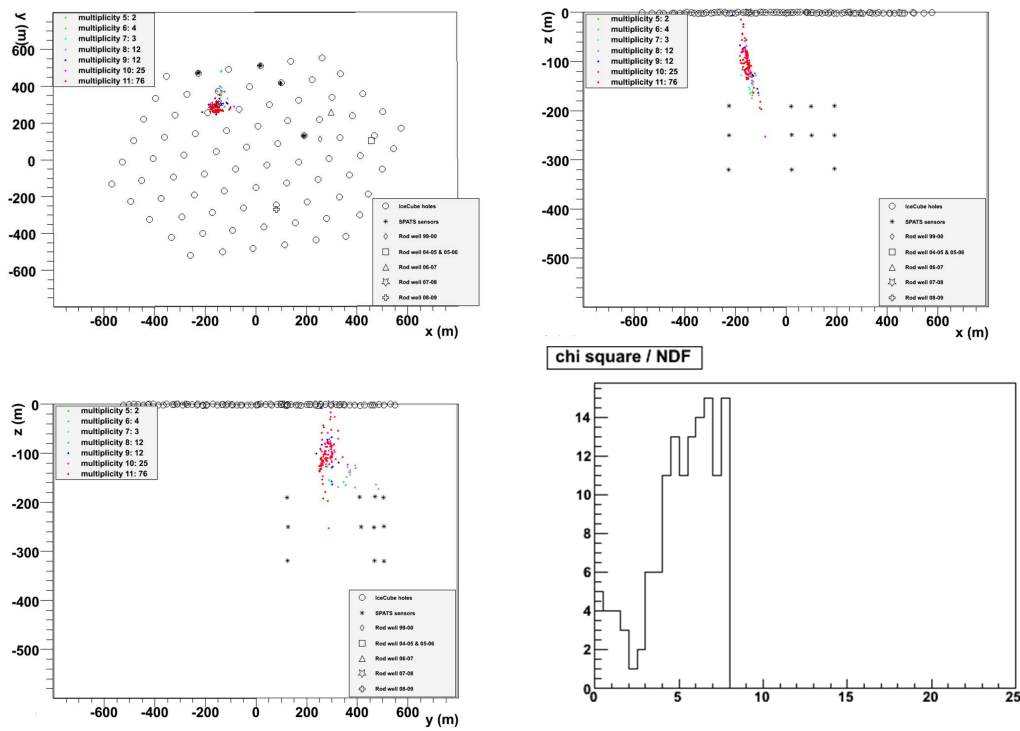


Figure 9.7: Reconstructed transient events from July 1st to October 22nd 2008 (quiet period) with $\chi^2 / \text{NDF} < 8$. The open circles at $z=0$ represent the IceCube holes and are no miss reconstructed events.

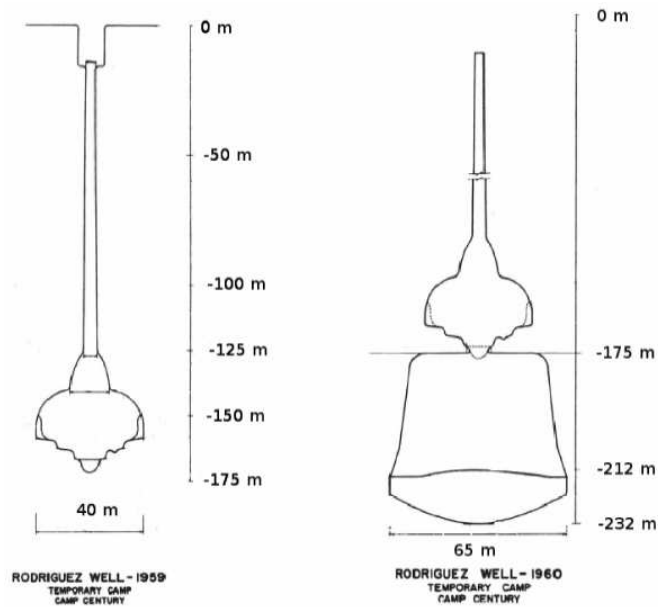


Figure 9.8: Schematic drawing of Rodriguez well (Rod well) [Sch 62].

Figure 9.9 shows the PSD of all triggered transient events (right side) and reconstructed events with $\chi^2/\text{NDF} < 8$ only (left side), recorded with HADES A during the quiet period. There is no visible difference between all triggered events and the subset of events which caused triggers in SPATS sensors and could be used for reconstruction.

The transient events frequency spectrum recorded by HADES A is more less flat with a casual excess around 48 kHz, which is a resonance frequency of the used piezo ceramic element, and around 5 to 25 kHz, which is the predicted region of interest for neutrino detection. In this roughly 4 month of transient data analysis only man-made sources (Rod well and refreezing IceCube holes) were observed. This is confirmed by other analyses and simulations [Ber 10]. Therefore the number of expected transient background events after the refreezing of all Rod wells and all IceCube holes should be low.

Excluding all events inside and around the IceCube holes, the Rod wells and the triangle built by hole #62, #63 and #70, which enclose the Rod well 07-08, two events from July 1st to October 22nd 2008 (114 days) would be left with the requirement of $\chi^2/\text{NDF} < 8$.

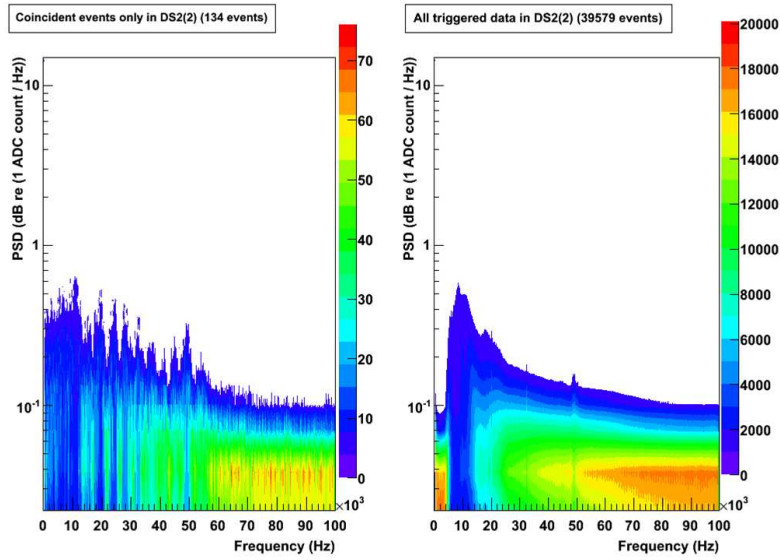


Figure 9.9: PSD of all triggered events (right) and reconstructed events with $\chi^2/\text{NDF} < 8$ only (left), recorded with HADES A during the quiet period from July 1st to October 22nd 2008.

Chapter 10

Summary and Outlook

The South Pole Acoustic Test Setup has been introduced with its components. In this thesis one type of acoustic sensor - HADES - was developed, characterized and installed as part of the SPATS array inside the South Pole ice sheet.

For directional measurements in water a tank with infrastructure (e. g. data acquisition) has been installed in Wuppertal. The relative angular sensitivity of the HADES sensor was measured and it is dominated from the shape of the surrounded resin and the location of the used piezo ceramic element inside the resin. A comparison with the relative angular sensitivity received via in-situ transmitter signal measurements have been presented.

The theory behind the two calibration techniques, comparison method and reciprocity method, has been introduced and HADES sensors were calibrated in water and ice. With the sensitivity in ice and the analyzed South Pole noise data an equivalent pressure South Pole noise level could be derived. In addition a noise variation with time (only visible with deployed HADES sensors) was investigated and possible reasons were discussed.

A transient event analysis with respect to one HADES sensor identified one Rod well as the dominant noise source in the used data set.

Some ideas and thoughts concerning the design for possible acoustic sensors in the future are given now.

The size of piezo ceramic element is well suited for the acoustical detection in the frequency range from 10-50 kHz. The type of the piezo electric element should be modified in a way that the charge coefficient d_{33} is maximized. For example a piezo electric element with an outer diameter similar to used piezo but a much smaller inner diameter.

The amplifier board offers more development potential concerning self-noise and size. The proposal is to reduce the size of the amplifier in a way that the dimensions of 1.5 cm in height and 2 cm in diameter are not exceeded. Maybe the two amplification stages can be divided into two separate circuit boards with connector pair. This new board would completely fit inside the ring shaped piezo.

The resin coating influences the angular sensitivity in an extreme way and damps the vibration of the piezo. Therefore the thickness of the surrounded media should be as reduced as possible. To increase the sensitivity via less damping through the resin one should explore the possibility of not filling the inner part of the ring shaped piezo element (which includes the amplifier) with resin but with dry air as described in [Agu 10]. Also the pressure stability of this new version should be tested.

The piezo/amplifier should be coated by resin (as thin as possible) to provide electrical insulation to the amplifier and to stabilize the connection between amplifier, piezo and cable to produce a robust device which would handle the deployment process. The sealing process needs to be modified in a way that the piezo element is indeed located in a centered position inside the casting mold to guarantee a coating with equally distributed thickness.

Based on [Tos pr] the two presented acoustic sensor types (piezo ceramic elements inside a steel housing and piezo ceramic element coated with resin and located outside of the housing) can be combined for further studies of coincident arrival time, sensitivity and reproducibility of received pulse shapes. As described above HADES uses a modified SPATS sensor housing with the same voltage converter board but only one out of three available channels. It should be possible to install two additional piezo electric elements with amplifiers at the inner wall (similar to the original SPATS sensors) to use the remaining channels and combine both types of acoustic sensors.

Bibliography

- [Abb 10] R. Abbasi *et al.*, *Measurement of sound speed vs. depth in South Pole ice for neutrino astronomy*, *Astropart. Phys.* **33**: (2010) 277; astro-ph/09092629
- [Abb10+] R. Abbasi *et al.*, *Calibration and Characterization of the IceCube Photomultiplier Tube*, *Nucl. Instrum. Meth. A* 618, 139, 2010; arXiv:1002.2442 [astro-ph.IM]
- [Abb 09] R. Abbasi *et al.*, *The IceCube Data Acquisition System: Signal Capture, Digitization, and Timestamping*, *Nucl. Instr. Meth. A* 601, 294, 2009; arXiv:0810.4930 [physics.ins-det]
- [Abb 08] R. Abbasi *et al.*, *Observation of the GZK cutoff by the HiRes experiment*, *Phys. Rev. Lett.* 100, 101101, 2008; astro-ph/0703099
- [Abb 1+] R. Abbasi *et al.*, *Measurement of Acoustic Attenuation in South Pole ice*, *Astropart. Phys.* **34**: (2011) 382; astro-ph/09092629
- [Abb ip] R. Abbasi *et al.*, *Background studies for acoustic neutrino detection at the South Pole*, in preparation
- [Abd ip] Y. Abdou *et al.*, *Design and performance of the South Pole Acoustic Test Setup*, in preparation
- [AbdPhD] Y. Abdou, PhD thesis, University Ghent, in preparation
- [Abr 08] J. Abraham *et al.*, *Observation of the Suppression of the Flux of Cosmic Rays above $4 \cdot 10^{19}$ eV*, *Phys. Rev. Lett.* 101, 061101, 2008; astro-ph/0806.4302
- [Abr 07] J. Abraham *et al.*, *Correlation of the highest energy cosmic rays with nearby extragalactic objects*, *Science* 318, 939, 2007; astro-ph/00711.2256

- [Ack 06] M. Ackermann *et al.*, *Optical properties of deep glacial ice at the South Pole*, J. Geophys. Res., 111, D13203, 2006
- [Agu 10] J. A. Aguilar *et al.*, *AMADEUS - The Acoustic Neutrino Detection Test System of the ANTARES Deep-Sea Neutrino Telescope*, 2010; astro-ph/1009.4179
- [Agu 06] J. A. Aguilar *et al.*, *First results of the instrumentation line for the deep-sea ANTARES neutrino telescope*, Astropart. Phys. **26**: (2006) 314
- [All 97] C. Allen *et al.*, *Status of Radio Ice Cherenkov Experiment (RICE)*, 1997; arXiv:astro-ph/9709223
- [Ant 06] G. Anton *et al.*, *Study of piezo based sensors for acoustic particle detection*, Astropart. Phys. **26**: (2006) 301
- [Ask 62] G. A. Askarian, *Excess negative charge of an electron-photon shower and its coherent emission*, Sov. JETP, 14, 1962
- [Ask 79] G. A. Askarian *et al.*, *Acoustic detection of high energy particle showers in water*, Nucl. Instrum. Meth., 162, 1979
- [Auf 10] J. Auffenberg, *On a prototype detector for the radio emission from air showers at the South Pole*, PhD thesis, Wuppertal, 2010
- [Aug 10] <http://www.auger.org>, 2010
- [Bah 01] J. N. Bahcall, E. Waxmann, *High energy astrophysical neutrinos: The upper bound is robust*, Phys. Rev. D 64, No 2, 023002, 2001; astro-ph/9902383
- [Ben 03] C. L. Bennett *et al.*, *First Year Wilkinson Microwave Anisotropy Probe (WMAP) Observations: Preliminary Maps and Basic Results*, Astrophys. J. Suppl. 148, 1, 2003; astro-ph/0302207
- [Ber 10] J. Berdermann and R. Nahnauer, *Acoustic transient event reconstruction and sensitivity studies with the South Pole Acoustic Test Setup*, Proceedings of the ARENA workshop 2010, Nucl. Instr. and Meth. A
- [Ber 06] V. Berezhinsky *et al.*, *On astrophysical solution to ultra high energy cosmic rays*, Phys. Rev. D 74, No 4, 043005, 2006; astro-ph/0204357

- [Bev 08] S. Bevan, *An investigation into the Feasibility of Sea Water or Ice Based Acoustic UHE Neutrino Telescopes*, PhD thesis, University College London, 2008
- [Bob 61] R. J. Bobber and G. A. Sabin, *Cylindrical Wave Reciprocity Parameter*, J. Acoust. Soc. Am., **33**, 446, 1961
- [Bös 03] S. Böser, *Status of acoustic detection studies for IceCube*, AMANDA Collaboration Meeting, Mons, 2003
- [Bös 06] S. Böser, *Acoustic detection of ultra-high energy cascades in ice*, PhD thesis, Humboldt-University, Berlin, 2006
- [Bös pr] S. Böser, *private communications*, Humboldt-University, Berlin, 2006 - 2010
- [Buo pr] S. Buogo, *private communications*, Istituto di Acustica e Sensoristica “Orso Mario Corbin”, Rome, Italy, 2010
- [Cav 81] G. Cavallo and H.M. Horstman, *Spectrum of cosmic fireballs*, Astrophysics and Space Science 75, No 1, 117, 1981
- [Ded 97] L. G. Dedenko *et al.*, *Prospects of deep sea acoustic detection of neutrinos*, Bull. Russ. Acad. Sci. Phys., 61, 1997
- [Des 09] F. Descamps, *Feasibility of acoustic neutrino detection in ice with the South Pole Acoustic Test Setup*, PhD thesis, University Ghent, 2009
- [Eng 01] R. Engel *et al.*, *Neutrinos from propagation of ultrahigh energy protons*, Phys. Rev. D. 64, No 9, 093010; astro-ph/0101216
- [Fer 34] E. Fermi, *Versuch einer Theorie der β -Strahlung I*, Z. Phys. **88**, 161, 1934
- [Fer 49] E. Fermi, *On the Origin of the Cosmic Radiation*, Phys. Rev. 75, No 8, 1169, 1949
- [Feu 10] T. Feusels, *Study of cosmic ray composition through muon bundle properties using coincident IceTop/IceCube measurements*, Proceedings of the 22nd European Cosmic Ray Symposium, 2010
- [Fis 06] J. Fischer, *Acoustic transducers for the South Pole Acoustic Test Setup*, Diploma thesis, Humboldt-University, Berlin, 2006

- [Gai 90] T. K. Gaisser, *Cosmic Rays and Particle Physics*, Cambridge University Press, 1990
- [Gra pr] K. Graf, *private communications*, University of Erlangen, Erlangen, 2006 - 2010
- [Gre 66] K. Greisen, *End to the Cosmic Ray spectrum*, Phys. Rev. Lett., **16**, 748, Cambridge University Press, 1966
- [Har pr] S. Hartmann, *private communications*, University Wuppertal, 2008 & 2009
- [Hel pr] R. Heller, *private communications*, DESY, Zeuthen, 2010
- [ITC 10] ITC product specifications:
http://www.itc-transducers.com/itc_page.asp?productID=6&type=3&subtypename=Calibration%20Standards&headline=Calibration%20Standards, July 2010
- [Jan 99] H. T. Janka *et al.*, *Black Hole - Neutron Star Mergers as Central Engines of Gamma-Ray Bursts*, Astrophys. J. Lett. 527, L39, 1999; [astro-ph/9908290](http://arxiv.org/abs/astro-ph/9908290)
- [Kar pr] T. Karg, *private communications*, University Wuppertal, 2006 - 2010
- [Kis 10] F. Kislat, *Measurements of the all-particle cosmic ray energy spectrum with IceTop*, Proceedings of the 22nd European Cosmic Ray Symposium, 2010
- [Kuc 03] S. Kuch, *Aufbau eines Hydrophone-Teststands und vorbereitene Studien zur akustischen Detektion ultrahochenergetischer Neutrinos*, diploma thesis, University of Erlangen, 2003
- [Kur 08] N. Kurahashi, *Updates from the Study of Acoustic Ultra-high energy Neutrino Detection phase II*, Proc. 3rd ARENA, 2008
- [Lai pr] K. Laihem, *private communications*, RWTH Aachen, 2010
- [Lan 91] L. D. Landau *et al.*, *Lehrbuch der theoretischen Physik - Hydrodynamik*, 5. Auflage, Akademie Verlag, 1991
- [Lea 00] J. G. Learned and K. Mannheim, *Lehrbuch der theoretischen Physik - Hydrodynamik*, Annu. Rec. Nucl. Part. 50, No 1, 679, 2000

- [McF 99] A. MacFadyen and S. E. Woosley, *Collapsars - Gamma-Ray Bursts and Explosions in "Failed Supernovae"*, *Astrophys. J.* 524, 262, 1999; astro-ph/9810274
- [Més 93] P. Mészáros and M. J. Rees, *Relativistic fireballs and their impact on external matter - Models for cosmological gamma-ray bursts*, *Astrophys. J.* 405, 278, 1993
- [Més 01] P. Mészáros, *Gamma-Ray Bursts: Accumulating Afterglow Implications, Progenitor Clues and Prospects*, *Since* 291, 79, 2001 astro-ph/0102255
- [Meu 10] T. Meures, *Reciprocity Calibration of Hydrophones in the Aachen Acoustic Laboratory*, Diploma thesis, RWTH Aachen, 2010
- [Mil 10] N. Miller, *private communications*, 2010
- [Mor 84] P. M. Morse, *Vibration and Sound*, 2nd ed., McGraw-Hill Book Company, New York, 1984
- [Mur 08] Murata Manufacturing Co. Ltd., *Piezoelectric Ceramics - PIEZOTITE R Sensors*, Cat.No.P19E-9, Japan, 2008
- [Nak 10] K. Nakamura et al. (Particle Data Group), *J. Phys. G* 37, 075021 (2010), <http://pdg.lbl.gov>
- [Neu 04] T. Neuenhöfer, *Die Entwicklung eines Verfahrens zur Suche nach kosmischen Neutrino-Punktquellen mit dem AMANDA-Neutrino-teleskop*, Aachen, 2004
- [Pau 10] L. Paul, *Characterization and calibration of acoustic devices for the South Pole Acoustic Test Setup*, Diploma thesis, RWTH Aachen, 2010
- [Pir 99] T. Piran, *Gamma-Ray Bursts and Fireball Model*, *Phys. Rept.* 314, 575, 1999; astro-ph/9810256
- [Pri 06] P. B. Price, *Attenuation of acoustic waves in glacial ice and salt domes*, *J. Geophys. Res.* 111 (2006) B02201; astro-ph/0506648
- [Raz 77] K. Ražnjević, *Thermodynamische Tabellen*, VDI Verlag (1977)
- [Ree 92] M. Rees and P. Mészáros, *Relativistic fireball - Energy conversion and timescales*, *Mon. Not. R. astr. Soc.* 258, 41, 1992

- [Rei 56] F. Reines *et al.*, *The Neutrino*, Nature **178**, 446, 1956
- [Ric 08] G. Riccobene *et al.*, *Longterm measurements of acoustic background noise in very deep sea*, Proc. 3rd ARENA, 2008
- [Sch 62] R. P. Schmitt and R. Rodriguez, *Glacier water supply and sewage disposal systems*, Proceedings of the Symposium on Antarctic Logistics, Colorado, National Academy of Sciences, National Research Council, 329-338, 1962
- [Sch 09] K. Schönauer, *Charakterisierung von Piezosensoren für Kalibrationsmessungen zum akustischen Neutrinonachweis in Eis*, Bachelor thesis, RWTH Aachen, 2009
- [Sem 07] B. Semburg, *Untersuchung von akustischen Sensoren zum Neutrino-Nachweis*, Diploma thesis WU D 07-06, University Wuppertal, 2007
- [Sem 08] B. Semburg *et al.*, *HADES - Hydrophone for Acoustic Detection at South Pole*, Nucl. Instr. and Meth. A (2009) 215; astro-ph/08111114
- [Sim 49] B. D. Simmons and R. J. Urick, *The Plane Wave Reciprocity Parameter and Its Applications to the Calibration of Electroacoustic Transducers at Close Distances*, J. Acoust. Soc. Am., **21**:633, 1949
- [Sta 91] T. Stanev *et al.*, *Radio detection of cosmic neutrinos; a numerical real time analysis*, Phys. Lett. B 257, 1991
- [Sta 09] T. Stanev *et al.*, *Status, performance and first results of the IceTop array*, Nucl. Phys. B, **196**:159, 2009; astro-ph/0903.0576
- [Sul 79] L. Sulak *et al.*, *Experimental studies of the acoustic signature of proton beams traversing fluid media*, Nucl. Instrum. Meth., 161, 1979
- [Swo 97] S. Swordy, *Astroparticle Physics at Chicago*, Website: <http://astroparticle.uchicago.edu/>, 1997
- [Tep 09] A. Tepe, *Hardware Integration of the AMANDA into the IceCube Neutrino Telescope and Search for Supersymmetric Particles with the IceCube Neutrino Telescope*, PhD thesis, University Wuppertal, 2009

- [Tho 04] T. A. Thompson *et al.*, *Magnetar Spindown, Hyper-Energetic Supernovae and Gamma Ray Bursts*, *Astrophys. J.* 611, 380, 2004; astro-ph/0401555
- [TMi 09] <http://root.cern.ch/root/html/TMinuit.html>
- [Tos pr] D. Tosi, *private communications*, Humboldt-University, Berlin, 2007 - 2010
- [Tos 10] D. Tosi, *Measurement of Acoustic Attenuation in South Pole Ice with a Retrievable Transmitter*, PhD thesis, Humboldt-University, Berlin, 2010
- [Uri 83] R. J. Urik, *Principle of underwater sound*, 3rd ed., Peninsula Publishing (1983)
- [Van pr] J. Vandenbroucke, *private communications*, University of California, Berkeley, 2008 - 2010
- [VDI 06] Verein Deutscher Ingenieure [Ed.], *VDI Wärmeatlas*, 10. Auflage, Springer Verlag (2006)
- [Vog 07] C. Vogt, *Aufbau eines Messplatzes zum Test akustischer Sensoren für den Nachweis ultra-hochenergetischer Neutrinowechselwirkungen*, Diploma thesis, RWTH Aachen, Aachen, 2007
- [Vog 08] C. Vogt *et al.*, *Speed of sound in bubble-free ice*, *J. Acoust. Soc. Am.* 124 (6), 3613, 2008
- [Wag 04] W. Wagner, *Design and Realisation of a new AMANDA Data Acquisition System with Transient Waveform Recorders*, PhD thesis, University Dortmund, 2004
- [Wax 99] E. Waxmann, J. N. Bahcall, *High energy neutrinos from astrophysical sources: An upper bound*, *Phys. Rev. D* 59, No 2, 023002, 1999; astro-ph/9807282
- [Wei 82] T. J. Weiler, *Resonant Absorption of Cosmic Ray Neutrinos by the Relic Neutrino Background*, *Phys. Rev. Lett.* 49, 234, 1982
- [Wie 09] C. Wiebusch, *Physics capabilities of the IceCube DeepCore detector*, Proceedings of the 31st International Cosmic Ray Conference, 2009; arXiv:0907.2263 [astro-ph.IM]

- [Woo 93] S. E. Woosley, *Gamma-ray bursts from stellar mass accretion disks around black holes*, *Astrophys. J.* 405, 273, 1993
- [Zat 66] G. T. Zatsepin, V. A. Kuzmin, *Upper limit of the spectrum of cosmic rays*, *JETP Lett.* 4, 78, 1966
- [Zie 10] S. Zierke, *Arbeit zur Ortsrekonstruktion akustischer Signale mit Hilfe von Laufzeitmessungen*, Bachelor thesis, RWTH Aachen, 2010
- [Zub 04] K. Zuber, *Neutrino Physics*, Dirac House, Temple Back, Bristol BS1 6BE, Institute of Physics Publishing, ISBN 0-7503-0750-1, 2004

Appendix A

Discrete Fourier transform

A.1 Basic equations

Consider a set of N real numbers $X_j \in \mathbb{R}$ ($j = 0 \dots N - 1$). We define two new sets $\tilde{X}_j \in \mathbb{C}$ and $Y_j \in \mathbb{C}$ ($j = 0 \dots N - 1$) of N complex numbers each:

$$\tilde{X}_j := \sum_{k=0}^{N-1} X_k e^{-2\pi i \frac{jk}{N}} \quad (\text{A.1})$$

$$Y_j := \sum_{k=0}^{N-1} \tilde{X}_k e^{2\pi i \frac{jk}{N}} = \sum_{l=0}^{N-1} X_l \sum_{k=0}^{N-1} e^{2\pi i \frac{k(j-l)}{N}} = \sum_{l=0}^{N-1} X_l N \delta_{jl} = NX_j \quad (\text{A.2})$$

Since $X_j \in \mathbb{R}$ the following relation holds:

$$\tilde{X}_{N-k} = \tilde{X}_k^* \quad (\text{A.3})$$

so that there are only $\frac{N}{2} + 1$ independent values \tilde{X}_j (For simplicity we assume N to be even).

A.2 Continuous Fourier transform

The continuous Fourier transform $\tilde{f} : \mathbb{R} \rightarrow \mathbb{C}, \omega \mapsto \tilde{f}(\omega)$ of a real function $f : \mathbb{R} \rightarrow \mathbb{R}, t \mapsto f(t)$ is defined as:

$$\tilde{f}(\omega) = \frac{1}{\sqrt{2\pi}} \int_{-\infty}^{\infty} dt f(t) e^{-i\omega t} \quad (\text{A.4})$$

with the inverse transform

$$f(t) = \frac{1}{\sqrt{2\pi}} \int_{-\infty}^{\infty} d\omega \tilde{f}(\omega) e^{i\omega t} \quad (\text{A.5})$$

Since $f(t) \in \mathbb{R}$ the following relation holds

$$\tilde{f}(-\omega) = \tilde{f}(\omega)^* \quad (\text{A.6})$$

and only non-negative frequencies ω have to be considered.

Energy conservation It is worth noticing that the total energy in the signal in the time and frequency domain are equal (Parseval's theorem):

$$\int_{-\infty}^{\infty} dt |f(t)|^2 = \int_{-\infty}^{\infty} d\omega |\tilde{f}(\omega)|^2 \quad (\text{A.7})$$

A.3 Discrete Fourier transform

Now consider the case of a digitized signal with N samples U_j recorded at sampling intervals Δt . Then the total length of the waveform is $T = (N-1)\Delta t$, and the Nyquist frequency is $f_{\max} = \frac{1}{2\Delta t}$. The frequency resolution is $\Delta f = \frac{f_{\max}}{N/2} = \frac{1}{N\Delta t}$.

In comparison with (A.4) we define the discrete Fourier transform (DFT) of U_j to be:

$$\tilde{U}_j := \Delta t \sum_{k=0}^{N-1} U_k e^{-2\pi i \frac{jk}{N}} \quad (\text{A.8})$$

Then the inverse transform is given by (compare to (A.5))

$$U_j := \Delta f \sum_{k=0}^{N-1} \tilde{U}_k e^{2\pi i \frac{jk}{N}} = \Delta f \Delta t N U_j = U_j \quad (\text{A.9})$$

where for the intermediate steps equations (A.2) and $\Delta t \Delta f = \frac{1}{N}$ were used.

The unit of the Fourier coefficients \tilde{U}_j is then (if U_j is measured in Volts): $[\tilde{U}_j] = \text{Vs} = \frac{\text{V}}{\text{Hz}}$.

One should notice that the Fourier coefficients \tilde{U}_j obviously depend on Δt and N so they are not a good quantity to compare different measurements or systems.

Energy conservation Notice that also in the discrete case energy is conserved (compare to (A.7)):

$$\Delta t \sum_{j=0}^{N-1} |U_j|^2 = \Delta f \sum_{j=0}^{N-1} |\tilde{U}_j|^2 \quad (\text{A.10})$$

A.4 Power spectral density (PSD)

The energy E of the recorded signal is given by (A.10):

$$E = \Delta f \sum_{j=0}^{N-1} |\tilde{U}_j|^2 \quad (\text{A.11})$$

If $T = (N - 1)\Delta t$ is the length of the signal the average power P is given by

$$P = \frac{E}{T} = \frac{\Delta f}{(N - 1)\Delta t} \sum_{j=0}^{N-1} |\tilde{U}_j|^2 \approx \frac{2\Delta f}{(N - 1)\Delta t} \sum_{j=0}^{N/2} |\tilde{U}_j|^2 \quad (\text{A.12})$$

where in the last step (A.3) was used. For a continuous signal (e.g. noise) P is independent of the length T of the recording.

So the power P_j in the j -th frequency bin of width Δf is

$$P_j = \frac{2\Delta f |\tilde{U}_j|^2}{(N - 1)\Delta t}, \quad (j = 0 \dots N/2) \quad (\text{A.13})$$

The power spectral density PSD_j is defined as the power per unit frequency, so

$$PSD_j = \frac{P_j}{\Delta f} = \frac{2|\tilde{U}_j|^2}{(N - 1)\Delta t}, \quad (j = 0 \dots N/2) \quad (\text{A.14})$$

which is independent of both the sampling rate Δt and the number of samples N (or equivalently Δf and N).

The unit of the power spectral density is (if U_j is measured in Volts) $[PSD_j] = \text{V}^2\text{s} = \frac{\text{V}^2}{\text{Hz}}$.

Numerical calculation The FFTW algorithm which is e.g. used in ROOT calculates DFTs using (A.1). So when one gets values \tilde{X}_j from such a calculation the PSD must be calculated as

$$PSD_j = \frac{2|\Delta t \tilde{X}_j|^2}{(N-1)\Delta t} = \frac{2\Delta t |\tilde{X}_j|^2}{(N-1)} \left(= \frac{|\tilde{X}_j|^2}{f_{\max}(N-1)} \right) \quad (\text{A.15})$$

Be careful: There are several programs out there which do not calculate $\tilde{X}_j = \sum_{k=0}^{N-1} X_k e^{-2\pi i \frac{jk}{N}}$ but $\tilde{X}_j = \frac{1}{\sqrt{N}} \sum_{k=0}^{N-1} X_k e^{-2\pi i \frac{jk}{N}}$ or use even other normalization factors, so that (A.15) has to be adapted accordingly.

A.5 Relation between PSD and signal RMS

If the mean value μ of a signal is zero:

$$\mu = \frac{1}{N} \sum_{j=0}^{N-1} U_j = 0 \quad (\text{A.16})$$

then the standard deviation σ^2 of the signal is given by

$$\begin{aligned} \sigma^2 &= \frac{1}{N} \sum_{j=0}^{N-1} |U_j|^2 = \frac{1}{N} \frac{\Delta f}{\Delta t} \sum_{j=0}^{N-1} |\tilde{U}_j|^2 \approx \frac{2}{N} \frac{\Delta f}{\Delta t} \sum_{j=0}^{N/2} |\tilde{U}_j|^2 \\ &= \frac{2}{N} \frac{\Delta f}{\Delta t} \sum_{j=0}^{N/2} \frac{(N-1)\Delta t PSD_j}{2} = \frac{N-1}{N} \Delta f \sum_{j=0}^{N/2} PSD_j \\ &\approx \Delta f \sum_{j=0}^{N/2} PSD_j \end{aligned}$$

So the integral over the power spectral density is equal to the standard deviation (RMS) in the time domain.

Acknowledgment

I would like to grateful acknowledge Klaus Helbing for accepting me as a PhD student. He was always interested in my progress and supported every idea I had with constructive hints and suggestions. He disbanded me before staring my journey to the South Pole with the words: “Have fun at the most southern hostel worldwide” (he was talking about the Jamesway).

Many thanks to Timo Karg for answering more less any question I had and for very fruitful result discussions. He assisted me during the pinger measurements in the pool.

Without Steffen Hartmann the Water Tank Test Facility could never been realized. He solved the problem of how to lift the concrete rings from the heavy goods vehicle via the crane over the other experiments in the experimental hall to its final position. Steffen also designed and installed the walkable platform and the rotatable sensor positioning.

The amplifier was designed by Karl-Heinz Becker and he taught me how to solder these little resistors, capacitors and so forth on the board.

Jahangir Pouryamout provided me spontaneously all these tiny little things like special screws and hooks whenever I asked him and he new who else in the University could help to solve any other problems not regarding these tiny little things.

Uwe Naumann joined the acoustic activities in the middle of my PhD but contributed important aspects and ideas concerning the reciprocity calibration and the hole acoustic sensor development business. I had fruitful discussions with him about possibilities for a complete new acoustic sensor design for future hybrid detectors.

During the past years I shared office with Daniel Bindig, Maria Gurtner, Jan-Patrick Hülß, Sandro Kopper, Martin Matusik, Jonas Posselt, Nils Potthof, Andreas Schultes and Andreas Tepe. At that time I spent more hours with these peoply than with my family at home. All of them contributed to a productive and friendly atmosphere and they were available for any kind of questions I had. Andreas Tepe became more than a colleague during our trips around and to the end of the world. Thanks to Andreas experiences and

his many hints (concerning what to do before or what to take along to the South Pole) which made my stay at the Amundsen-Scott South Pole station as convenient as possible.

Of course the other IceCube people, the Auger group and the CBM group in Wuppertal contributed to the very nice working atmosphere and beside work we spent several funny nights with pizza and video, BBQs or Christmas parties.

My thanks also go to Larissa Paul, Thomas Meures and the Aachen Acoustic Laboratory scientists around their leader Christopher Wiebusch which offered me the possibility to use their IceTop tank for my in-ice calibration purpose.

Silvano Buogo from CNR - Istituto di Acustica e Sensoristica “O. M. Corbin” shared his knowledge and all the tiny little secrets about the reciprocity calibration process with me.

Many thanks to all members of the IceCube AND working group for the hints, comments and suggestions concerning my work. We had a lot of productive and nice meetings around the world.

Whenever paper works needed to be done, Ms. Schaarwächter was a great help.

Penny, Leonard, Sheldon, Howard and Rajesh showed me in a nice and encouraging way to be proud of being a physicist and to handle the reaction of (not nerdy) people at parties (or general in public) with the right humor when telling about my job.

Also many thanks to Domenico Eisert and the hole crew of the urban swimming pool in Haan. They make it possible for me to use the big water volume outside the opening hours to do the pinger measurement.

Anna-Livia Wörner supported the quality of this thesis with her linguistic knowledge of the English language.

Bärbel and Wolfgang Völkel from child care *Kribbel Krabbel* looked after our son while mommy and daddy were at work. How comforting to know that our offspring was so well taken care of.

The last (but absolutely not least) paragraph is dedicated to the people of capital importance in my life - my family. My parents, my sister and my wife were like a rock in the past, and sometimes very turbulent, weeks and months. Thank you for all the good words, the patience, the support and for simple being there (all true not only for the last weeks). My greatest event up to now in my life has been the birth of our son Tom Malte in May 2009. Life itself is much more exciting than hunting for (ultra) extremely high energetic neutrinos, coming out of the universe, with the biggest detector (built until now) installed at the craziest place on Earth.

Lebenslauf

Name	Benjamin Semburg
Anschrift	Wormser Straße 42119 Wuppertal
Geburtsdatum und Ort	9. Juli 1981 in Hilden
Familienstand	verheiratet; ein Sohn (geboren: 5 / 2009)
Derzeitige Tätigkeit seit 7 / 2007	Promotionsstudent und wissenschaftlicher Angestellter an der Bergischen Universität im Bereich der Astroteilchenphysik
Studentische Hilfskraft 8 / 2005 - 6 / 2007	Betreuung des Versuches “Experimente mit polarisiertem Licht” im Rahmen des physikalischen EE/IT-Praktikums
Hochschulstudium 10 / 2002 - 6 / 2007	Physikstudium mit Abschluss Diplom- Physiker an der Bergischen Universität Wuppertal; Thema: “Untersuchung von akustischen Sensoren zum Neutrino-Nachweis”
Wehrdienst 9 / 2001 - 6 / 2002	Grundausbildung in der Waldkaserne in Hilden, danach Dienst in der Bergischen Kaserne in Düsseldorf beim 1. Führungs- unterstützungsregiment 30
Schuldbildung 1998 - 2001 1992 - 1998	Berufskolleg am Haspel in Wuppertal Emil-Barth-Realschule in Haan

Selbständigkeitserklärung

Hiermit bestätige ich, diese Arbeit selbständig und nur unter Verwendung der angegebenen Quellen erstellt zu haben.

Benjamin Semburg

Wuppertal, im Februar 2011

